NUMERICAL STUDY OF DETONATION FLAME ARRESTOR PERFORMANCE AND

DETONATION INTERACTION WITH THE ARRESTOR ELEMENT

by

HODEN ALI FARAH

Presented to the Faculty of the Graduate School of

The University of Texas at Arlington in Partial Fulfillment

of the Requirements for the Degree of

DOCTOR OF PHILOSOPHY

THE UNIVERSITY OF TEXAS AT ARLINGTON

December 2019

This dissertation is dedicated to my mother, Kedija, and my husband, Ermias,

who always stood by me and gave me their love

ACKNOWLEDGMENTS

ABSTRACT

NUMERICAL STUDY OF DETONATION FLAME ARRESTOR PERFORMANCE AND

DETONATION INTERACTION WITH THE ARRESTOR ELEMENT

Publication No. _____

Hoden A. Farah, Ph.D.

The University of Texas at Arlington, 2019

Supervising Professor: Frank Lu

A numerical study of detonation propagation and interaction with a flame arrestor product in a combustible gas/vapor transport pipeline system is conducted. The flame arrestor element is modeled as a porous medium using the Forchheimer equation, which is incorporated in the governing conservation equations as a momentum sink. The Forchheimer porous medium model is then used to model the flow through a representative four-inch detonation flame arrestor and is validated with experimental data. The detonation propagation simulation is modeled with the Reynolds averaged Navier-Stokes (RANS) equations extended for reacting flows. A 21-step chemical kinetic mechanism with 10 species is used to resolve the hydrogen-oxygen combustion. A series of detonation propagation case studies is conducted to validate the numerical model. The detonation propagation numerical result is qualitatively compared to experimental data and is shown to have the same trend. Numerical simulation is used to predict the transmission or interruption of detonation wave propagation through the flame arrestor product and is confirmed with historical test data.

TABLE OF CONTENTS

LIST OF FIGURES

LIST OF TABLES

LIST OF ABBREVIATIONS

A_k Pre-exponential factor in reaction k for Arrhenius expression

C Courant number

c Speed of sound

C_p Specific heat capacity at constant pressure of the mixture

C_{pi} Specific heat at constant pressure of species i

ρ Total domain multi species density

ρ_i Density of the species i

D_a Damköhler number

D_i Diffusion coefficient for species i

D_{th} Heat diffusivity coefficient

E Total Energy

E_k Activation energy in reaction k for Arrhenius expression

e_i Internal energy of species i

e Internal energy per unit mass

ε Porosity of the zone

$\vec{F}$ Flux vector in x-direction

$\vec{G}$ Flux vector in r-direction

$\vec{H}$ The axisymmetric flux term

H_i^0 Molar enthalpy

h Enthalpy per unit mass

h_i Enthalpy of species i

h_i^f Heat of formation of species i

k Thermal conductivity

$k_{f,k}$ Forward rate constant in reaction k

$k_{b,k}$ Backward rate constant in reaction k

M Mach number

M_2 Mach number downstream of shock wave

m_i	Mass of species i
m	Total mass of the mixture
N_A	Avogadro's number
N_r	Number of elementary reactions
N_s	Number of species
$\vec{n}$	Normal vector
Pr	Prandtl number
p	Static pressure
p_{atm}	atmospheric pressure
p_r	reduced pressure
p_s	von Neumann pressure spike
$\vec{Q}$	Vector of conserved variables
R	Specific gas constant
$\bar{R}$	universal gas constant
$\mathcal{R}$	Residuals
Re	Reynolds number
$\vec{S}$	Vector of source terms
S_{ci}	Schmidt number
T	Static temperature
T_0	Reference Temperature
t	Time
U	Any primitive variable
u_x	Velocity component in axial direction
u_r	Velocity Component in radial direction
u_D	Detonation wave speed
u_G	Gas speed
W_i	Molecular weight of species i
W	Mean molecular weight of the mixture
X_i	Molar concentration of species i
x, r	Cylindrical coordinate

Y_i	Mass fraction of species i
n	Temperature exponent in reaction k for Arrhenius expression
γ	Ratio of specific heats
μ	Viscosity coefficient
μ_t	Turbulent viscosity coefficient
v'	Stoichiometric coefficients of reactant
v''	Stoichiometric coefficients of product
$\dot{\omega}_i$	Mass production rate of species i
$(\bar{\ })$	Mean
$(\ )'$	Fluctuating

CHAPTER 1

INTRODUCTION AND BACKGROUND

1.1 Detonation Arrestor Applications and Operating Principles

Gas explosions have a significant impact on the safety of chemical processing industries and petrochemical plants. The damage caused by these explosions can be very significant, especially in confined spaces such as pipelines transporting flammable gas mixtures, or semi-confined spaces such as storage tanks. Inline flame arrestors are devices used for safety in pipelines transporting flammable gas or vapors mixtures where there is a potential for accidental combustion due to an ignition source. The operating principles of flame arrestors was discovered in 1815th by the famous chemist and professor, Sir Humphry Davy, who invented the Davy's lamp for coal mining applications. Current flame arrestors operate within the same principles, except for some additional features to enhance the flame arrestor's performances. In the same time frame, working independently, George Stephenson discovered, that the effective diameter to disrupt the transmission of a flame is dependent on the flammable gas mixture type and concentration. This discovery provided bases for the concept of quenching distance which led to the concept of "Maximum Experimental Safe Gap" (MESG) [1]. Inline flame arrestors are the secondary fail-safe provision in the vapor control systems, in addition to the active flame safety devices such as liquid seals, oxygen analyzers, temperature sensors, pressure vents, etc. There are two major categories of flame arrestors; deflagration flame arrestors used for protection against slow moving subsonic flame propagation, and detonation flame arrestors used for protection against detonation propagation. The critical design characteristic of the flame arrestor is determined based on the type

of flame which is expected and the chemical composition of the flammable gas or vapor in the system. There are detailed reviews of successful and unsuccessful application of flame arrestors. From these reviews, especially the unsuccessful applications, the main reason for the failure of the arrestor is either faulty arrestor design or improper installation location or applications [1].
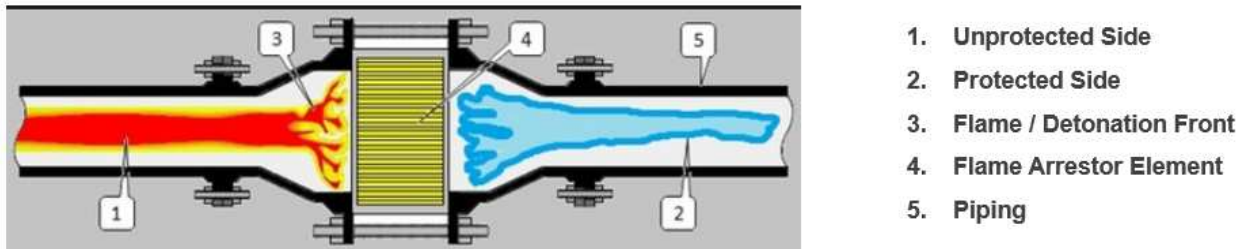
Figure 1-1 Flame arrestor operation schematic [38]

As shown in Figure 1-1, the pipeline connecting a flame arrestor with an identified ignition source is the "unprotected side" of the flame arrestor and the pipeline connecting the arrestor to the equipment that needs to be protected from flame penetration is the "protected side."

Typical applications for flame arrestors are shown in Figure 1-2. Chemical storage tank with a flame arrestor is shown in Figure 1-2 (A), where end-of line flame arrestor is shown on the top of the tank and in-line flame arrestor is used in the pipe leading to the tank. Figure 1-2 (B) shows inline flame arrestor mounted on installation rig.
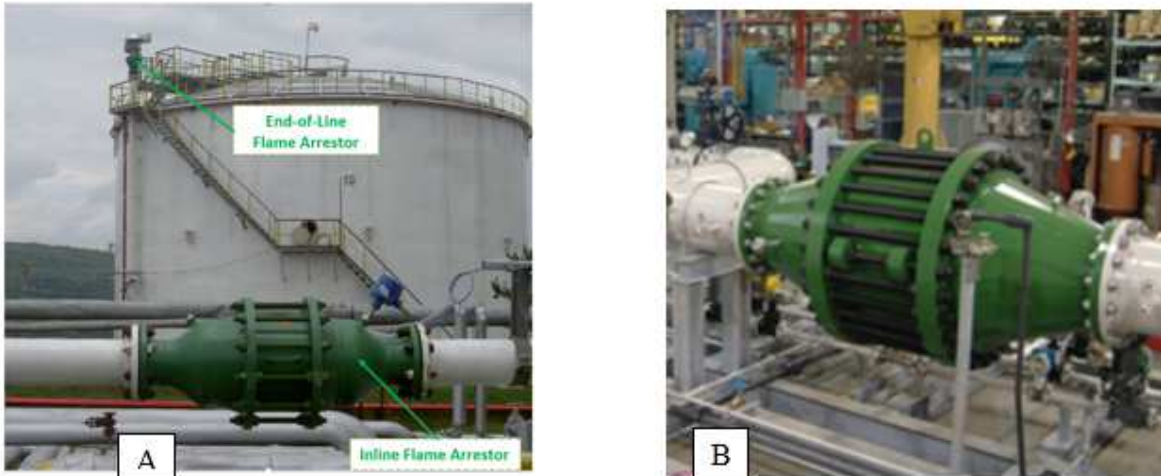
Figure 1-2. Inline flame arrestor applications
(A). Gas storage tank application, (B). Inline flame arrestor installation rig

One of the main characteristics in such pipeline systems design is the pressure drop across the arrestors which is predominantly associated with the crimp design of the flame arrestor element. An example of a crimped flame arrestor element is shown in Figure 1-3.
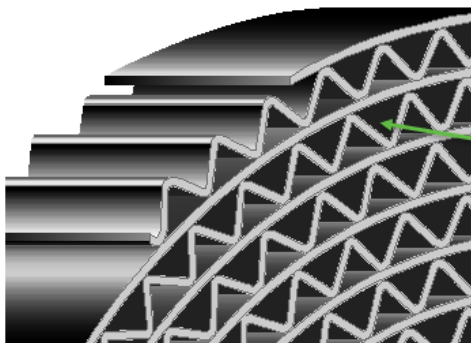
- Flame is forced to pass through these narrow channels
- The narrow channels limits the formation of detonation cells structure
- Large contact area removes significant amount of heat from the flame
- This leads to flame / detonation propagation interruption

Figure 1-3 Crimped flame arrestor element sketch [38]

The figure shows small isosceles triangular channels formed by crimping sheet metal. Flame and detonation propagation are interrupted by the arrestor element due to the removal of heat by the large contact surface area through these channels and restriction of detonation cell

formation. For the former, it is well known that flames are quenched when heat is extracted from the combustion process [2]. Further, it has been observed that a propagating detonation wave leaves behind a fish-scale pattern or cells in soot foils that have a characteristic length scale [8]. A passage with a diameter less than the detonation cell width will prevent the detonation from propagating. Thus, the crimped arrestor design can arrest both flame and detonation wave propagation. Thomas et al [27] have conducted experimental studies to understand the behavior of high temperature reactive gas flows in relation to the maximum experimental safety gap (MESG) characteristics. This study provides the propensity of gaseous mixture to undergo flame acceleration to detonation which is key to the selection of flame arrestor type and installation location.

1.2 Review of Detonation Physics and Reacting Flow Computational Study

Detonation is a type of combustion involving a supersonic reacting front accelerating through a medium that eventually drives a shock front. The shock front is defined as the detonation wave. Since the detonation wave is supersonic, the reactants ahead of the detonation wave are not disturbed prior to the arrival of the detonation wave and remain at the initial state.

A detonation wave has a multidimensional complex structure [8, 24]. This structure consists of leading shock waves, triple points and transverse waves, and has a cellular pattern. Figure 1-4 shows the cellular structures of a detonation wave recorded on soot foil by the triple point trajectory. The structure of a detonation wave is correlated with detonation limits.
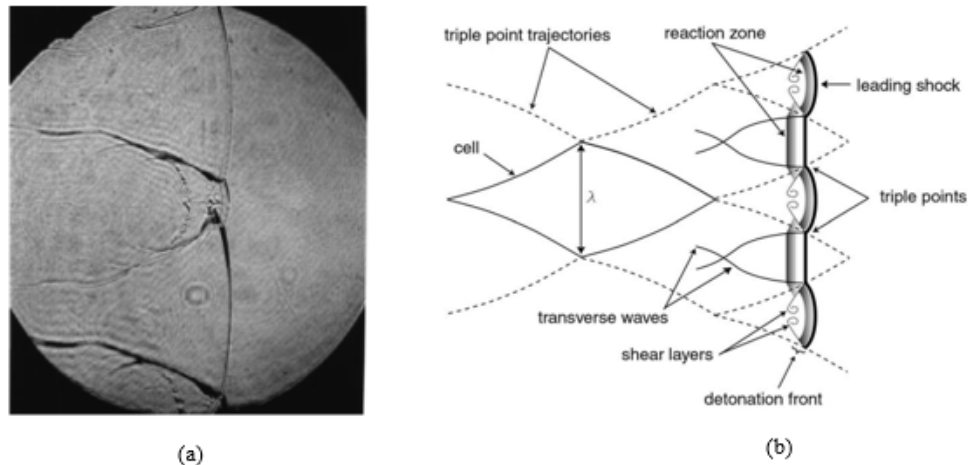
Figure 1-4. The three-dimensional detonation structure
(a) Pulsed laser schlieren image of detonation front in $2H_2$-O_2-17Ar (b) Formation of the cellular structure on a soot foil record by detonation wave [9]

There are simple theoretical models for describing the detonation wave. The detonation wave can be regarded as single surface of discontinuity, separating the burned and the unburned gases. As the detonation wave passes, it compresses the gases and increases the temperature significantly leading to ignition and driving the detonation wave. Detonation is a special case of combustion compared to deflagration which is the common class of combustion. Deflagration is a slow combustion where the velocity of the flame propagation is subsonic. In deflagration, heat conduction and diffusion of species drive the combustion process and keep the pressure nearly constant. An explosion is different from detonation or deflagration in that it does not require propagation of a combustion wave through the exploding medium.

Detonation was first studied systematically by two scientists, Berthelot and Vielle, in the late 19th century and mathematical prediction of detonation waves propagation was carried out by Chapman and Jouguet in a similar time frame, which is referred as the Chapman-Jouguet (CJ) theory. Advances in understanding detonation waves were made by Zeldovich, von Neumann, and

Döring working independently in the 1940s leading to the Zeldovich-von Neumann-Döring (ZND) theory.

In the Chapman-Jouguet theory of detonation propagation, it is assumed that the chemical reactions take place instantaneously inside the shock and the reaction zone thickness is zero. In the Chapman-Jouguet condition, the reaction products are assumed to follow the detonation wave at the local sonic speed and the detonation wave speed is constant. CJ theory enables the velocity of the detonation wave and post-detonation thermodynamic characteristics to be determined using the governing conservation equations and the initial conditions of the fuel–oxidizer mixture [9]. CJ theory provides insight on the macroscopic characteristics of detonation propagation in a confined space, which provides a foundation in studying detonation arrestor application systems.
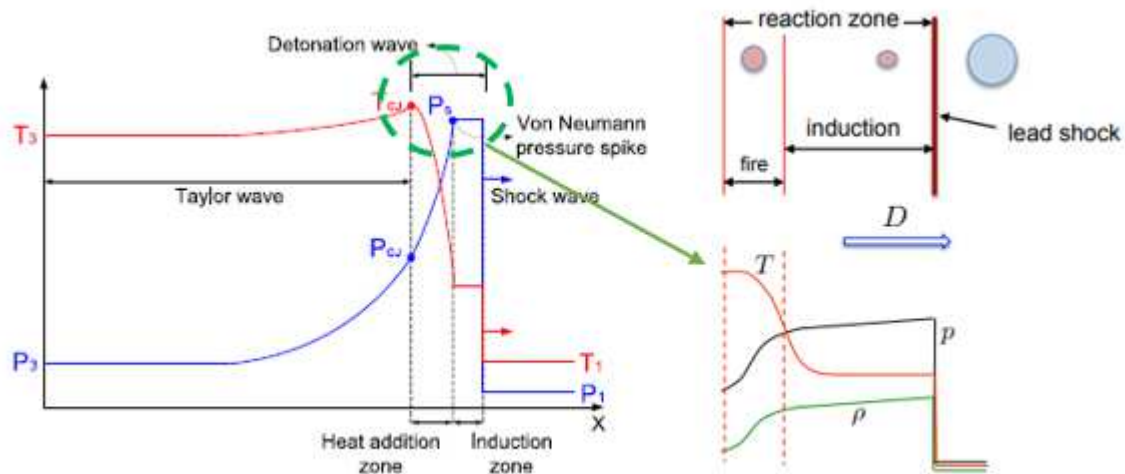
Figure 1-5 The ZND structure [26]

The ZND model shown in Figure 1-5 assumes, that the gas ahead of the shock wave is quiescent and there is insignificant reaction. Passing through the lead shock the fuel–oxidizer

mixture is compressed tremendously, and its temperature rises thousands of degrees. This induces chemical reactions which go to completion very rapidly in a thin reaction zone behind the shock to sustain the propagation of the shock. The leading shock can be approximated as a frozen shock moving at the same velocity as the detonation wave. Thus, the strength of the leading shock depends on the detonation velocity. As indicated in Figure 1-5 the highest pressure of the shock is called the von Neumann pressure spike. The reaction zone is divided into two regions, namely, the induction zone and the heat addition zone. In the induction zone, the reaction is delayed due to the finite time required to initiate chemical reactions. Once the reactions are initiated, the energy is released to the flow so that the temperature is further increased. The state at which the reaction is completed corresponds to the CJ conditions indicated as P_{CJ} and T_{CJ} in Figure 1-5. A Taylor rarefaction is generated behind this point. Thus, the pressure and temperature in this region are decreased to match the left wall boundary conditions.

1.3 Review of Numerical Studies in Detonation Propagations

The equations governing flows with chemical reaction are the continuity, the Navier-Stokes, the energy and the species conservation equations. The fluid dynamics and the chemical reactions are strongly coupled, and they have different time scales. Stiffness of equations arising from detailed chemistry is one of the most difficult issue in chemically reacting flows. In ANSYS® Fluent™, detonations are modeled with a finite-rate model using a density-based solver. Multiple simultaneous chemical reactions can be modeled with reactions occurring in the fluid phase (volumetric reaction) or in a porous region. The solver predicts the local mass fraction of each species through the solution of a convection-diffusion equation for the species conservation equation. The reaction rates in turbulent flows are computed by direct use of finite-rate kinetics.

The effect of turbulence on kinetics rates are neglected, and reaction rates are determined by general finite-rate chemistry directly. In-Situ Adaptive Tabulation (ISAT) is used by the software to accelerate the detailed, stiff chemistry calculation. The database for the elementary reaction mechanism, thermodynamic data and transport parameters for hydrogen–oxygen reaction used in this simulation were downloaded from the Lawrence Livermore National Laboratory [36]. The hydrogen-oxygen reaction mechanism was verified and developed for a large range of temperatures and pressures by O'Conaire et al. [23].

Much of the recent numerical studies of detonation propagation has focused to obtain detailed understanding in the 2D and 3D cellular structures of the detonation wave front [19,20,21], and there are numerical and experimental studies in understanding and predicting detonation gas dynamics and propulsion characteristics for application in jet propulsion engines [17,18,19]. Yi developed a CFD code for two-dimensional, multi-species reacting laminar flows for pulse detonation engine applications [26]. There are only few reported scientific research and numerical studies conducted in flame arrestor applications. Thomas et al [29] conducted experimental studies to understand deflagration to detonation transition phenomena, on selection and testing of explosion prevention devices. Sun et al. has developed a numerical model for simulation of detonation wave propagation and quenching in flame arrestor applications [22].

1.4 Review of Porous Media Model

The Reynolds number is a dimensionless number, which is defined as the ratio of inertial forces to viscous forces within a fluid caused by relative movement due to different fluid velocities. [5] The Re is used to predict flow patterns in different fluid flow situations and it has wide applications

in porous-media/fracture flow, internal pipe flow, external flow, etc. One of its main applications is to predict the transition from laminar to turbulent flow.

$$Re = \frac{\rho \bar{u} L}{\mu} = \frac{\bar{u} L}{\nu} \tag{1}$$

where ρ is the density of the fluid, μ is the dynamic viscosity and L is a characteristic length.

The flow regime classification established recently [13,16] for the porous media / fracture flow is slightly different from the traditional classification of laminar and turbulent regimes. In this classification, there are five flow regimes based on the Re number, from small to large Reynolds number as, 1 = Darcy, 2 = weak inertia, 3 = Forchheimer (strong inertia), 4 = transition from Forchheimer to turbulence, and 5 = turbulence.

The Darcy's law is valid for Re < 1, in this regime the flow rate and the pressure gradient have linear relationship. The viscous force is dominant, and the inertial force is neglected. For a one-dimensional steady-state Newtonian fluid flow, Darcy's law can be written as:

$$-\frac{\partial p}{\partial x} = \frac{\mu}{\alpha} u_x \tag{2}$$

where p is the pressure, u_x is the velocity, x is the distance in the flow direction, μ is the dynamic viscosity and α is the permeability of the solid phase.

As the Reynolds number increases, the inertial force becomes more significant and the relationship between inertial force and pressure gradient becomes nonlinear. The nonlinear relationship between the pressure drop and velocity in the weak inertia region is developed from both microscopic and macroscopic scale porous media and has been numerically confirmed

recently [15]. In this regime, Darcy's law is corrected by adding a cubic term in velocity and is given by:

$$-\frac{\partial p}{\partial x} = \frac{\mu}{\alpha} u_x + \frac{\gamma}{\alpha} \rho^2 u_x^3 \tag{3}$$

where γ is the weak inertial factor. It can be noted that this is the regime where the inertial force is of the same order as the viscous force

The Forchheimer (strong inertia) regime starts as the Reynolds number increases further, where the pressure drop is proportional to the square of the velocity:

$$-\frac{\partial p}{\partial x} = a u_x + b u_x^2 \tag{4}$$

where a and b are constants related to the fluid characteristic and the porosity of the medium.

Much research has been done to develop the coefficients in the Forchheimer equation using analytical and experimental methods for granular porous media made of spherical elements or other shapes [13]. Chan et al. [14] conducted macroscopic modelling of turbulent flow in porous media. Kim et al. [15] developed numerical modeling of laminar pulsating Flow in Porous Media. The flow regime in the porous medium is characterized by Skjetne et al. [16] using the Reynolds number. Sidiropoulou et al. [12] proposed empirical equations to determine the Forchheimer coefficients via a survey of experimental data.

A reformulated Forchheimer equation is given by:

$$-\frac{\partial p}{\partial x} = \frac{\mu}{\alpha} u_x + \frac{C_2}{2} \rho u_x^2 \tag{5}$$

where α is the permeability and C_2 is the inertia resistance coefficient (Forchheimer coefficient).

For fully-developed steady flow, where u_x is not a function of x, integrating Equation (5) yields

$$-\Delta p = \left(\frac{\mu}{\alpha} u_x + \frac{C_2}{2} \rho u_x^2\right) \cdot \Delta x \tag{6}$$

where $\Delta p = (p_2 - p_1)$, pressure drop across the porous media and $\Delta x = (x_2 - x_1)$ is length of porous media.

1.5 Preview of Present Research

The flow characteristics and performance of inline detonation flame arrestors are usually studied experimentally. The main challenges in implementing numerical computational methods are the complex geometry of the arrestor flame element and the complicated system of equations generated from theoretical models of multi-species reacting turbulent flows.

The main objective of this research is to develop a numerical method to evaluate and analyze the performance characteristics of detonation flame arrestors. The numerical method developed is then used to solve the flow characteristics of four-inch detonation flame arrestor and to evaluate the detonation propagation and attenuation mechanism in the flame arrestor applications. The simulation domain representing the flame arrestor element is modeled as a porous medium to overcome the difficulty of creating a complex flow domain in the flame arrestor element. The porous medium model is included in the governing equation as a momentum sink using the Forchheimer equation. The proportionality coefficients for the Forchheimer equations are determined experimentally.

11

In Chapter 2, the governing equations for the viscous axisymmetric turbulent Reynolds Averaged Navier-Stokes (RANS) equations extended for multi-species chemical reacting flow are discussed and summarized. The Shear Stress Transport, SST k–ω model equations used to evaluate the turbulent viscosity is discussed. The various physical models are discussed and summarized, such as the porous media model in Section 2.3, the thermodynamic model, in Section 2.4 and the chemical kinetics model in Section 2.5.

In Chapter 3, numerical models are developed and verified. In Section 3.1, the Forchheimer equation representing the porous medium model is developed and the proportionality coefficients are determined using experimental flow test data. Several different models (axisymmetric and three-dimensional models) are used to verify the numerical simulation result using the porous medium model. A four-inch detonation flame arrestor flow is simulated using the porous medium model and the results are validated experimentally. In section 3.2, a detonation tube simulation is used to validate the numerical simulation method by comparing it to analytical one-dimensional detonation propagation solution. Mesh sensitivity analysis is conducted to determine the optimum grid size and the appropriate timestep is selected to assure stability of the numerical solution that does not violate the Courant-Friedrichs-Lewy (CFL) condition. In section 3.3 to 3.5 the simulation domain used is a two-dimensional axisymmetric geometry based on the ISO 16852 standard detonation flame arrestor validation test setup configuration. Inviscid model, viscous adiabatic model and viscous with heat transfer model are used for the detonation propagation simulation.

The four-inch detonation flame arrestor simulation results are presented in Chapter 4. The first section provides flow simulation result using the porous medium model and comparison with the experimental data. In section 4.2, numerical simulation result of detonation propagation

simulation of four-inch flame arrestor and analysis are presented and discussed. Detonation characteristics in each section of the domain, inlet and outlet flanges and interaction with the flame element are presented. The flame element is modeled using porous medium and the effect of the porous medium parameters on the transmission of the detonation wave are presented. The phenomena of re-initiating of detonation and the transition from unstable detonation to stable detonation are discussed. Concluding remarks, summary of this study and recommendations for future research are given in Chapter 5.

CHAPTER 2

GOVERNING EQUATIONS

The equations governing flows with chemical reaction are the continuity, the Navier-Stokes, the energy and the species conservation. The solution to these equations provides all the information needed to study the detonation flame arrestor application systems [23]. However, reacting flows involves multi-species and multi-reactions. The species are characterized through their mass fraction Y_i for i = 1 to N_s. Y_i is defined as: $Y_i = m_i/m$, where m_i is the mass of species i and m is the total mass of the mixture and N_s is the total number of species. For reacting flows, the problem requires to solve additional N_s variables instead of just the flow variables. The reacting flow problem also involves different time scales, the chemical reaction time scale, which could be different for different species involved in the chemical reaction and the flow time scale.

2.1 The Governing Equations in Differential Form

Conservation of mass:

$$\frac{\partial \rho}{\partial t} + \frac{\partial (\rho u_k)}{\partial x_k} = 0 \tag{7}$$

Conservation of momentum, Navier-Stokes

$$\frac{\partial (\rho u_i)}{\partial t} + \frac{\partial (u_k u_i)}{\partial x_k} = -\frac{\partial p}{\partial x_i} + F_i + \frac{\partial \tau_{ik}}{\partial x_k} \tag{8}$$

with the shear stress related to the strain rate by

$$\tau_{i,j} = \mu \left(\frac{\partial u_i}{\partial x_j} + \frac{\partial u_j}{\partial x_i} \right) - \frac{2}{3} \mu \frac{\partial u_k}{\partial x_k} \delta_{i,j} \tag{9}$$

Conservation of mass of species α

$$\frac{\partial(\rho Y_\alpha)}{\partial t} + \frac{\partial(\rho u_k Y_\alpha)}{\partial x_k} = \frac{\partial}{\partial x_k} \left(\rho D \frac{\partial Y_\alpha}{\partial x_k} \right) + \omega_\alpha \tag{10}$$

where we have assumed Fick's law for diffusion.

Conservation of energy

In terms of enthalpy h

$$\frac{\partial(\rho h)}{\partial t} + \frac{\partial(\rho u_k h)}{\partial x_k} = \frac{\partial p}{\partial t} + \frac{\partial}{\partial x_k} \left(\lambda \frac{\partial T}{\partial x_k} \right) + \frac{\partial}{\partial x_k} \left(\rho D \sum_{\alpha=1}^{N} h_\alpha \frac{\partial Y_\alpha}{\partial x_k} \right) \tag{11}$$

In terms of temperature, assuming a perfect gas,

$$c_{p,m} \frac{\partial(\rho T)}{\partial t} + c_{p,m} \frac{\partial(\rho u_k T)}{\partial x_k}$$

$$= \frac{\partial p}{\partial t} + \frac{\partial}{\partial x_k} \left(\lambda \frac{\partial T}{\partial x_k} \right) - \sum_{\alpha=1}^{N} h_\alpha \omega_\alpha + \rho D \frac{\partial T}{\partial x_k} \sum_{\alpha=1}^{N} c_{p,\alpha} \frac{\partial Y_\alpha}{\partial x_k} \tag{12}$$

where u_i is the velocity, ρ is the density, p is the pressure, g_i is the body force, $\tau_{i,j}$ is the viscous stress, Y_α is the mass fraction of the species α, D is the diffusion coefficient (assumed same for all species), ω_α is the chemical source term, λ is the conductivity, T is the temperature and h_α is the absolute enthalpy. The mixture heat capacity $c_{p,m} = \sum_{\alpha=1}^{N} Y_\alpha c_{p,\alpha}$, where N is the total number of species and the mixture enthalpy $h = \sum_{\alpha=1}^{N} Y_\alpha h_\alpha$

The main non-dimensional numbers used in flow analysis are the Reynolds number (ratio of inertia force to viscous force, $R_e = \frac{\rho u L}{\mu} = \frac{u L}{\nu}$), the Prandtl number, (ratio of the momentum diffusivity to the thermal diffusivity, $Pr = \frac{\mu c_p}{\lambda} = \frac{\nu}{\alpha}$), Schmidt number, (ratio of momentum/kinematic diffusivity to mass diffusivity $Sc = \frac{\mu}{\rho D} = \frac{\nu}{D}$), and in reacting flows the Lewis number, (ratio of thermal diffusivity to mass diffusivity $Le = \frac{\lambda}{\rho c_p D}$ and the Damköhler number, the ratio of physical time, τ_{phys}, scale and the chemical time scale τ_{chem}, $Da = \frac{\tau_{phys}}{\tau_{chem}}$ are common.

2.2 Reynolds-Averaged Navier-Stokes (RANS) Equations

The flow in the pipelines in flame arrestor applications is expected to be turbulent. The solution therefore proceeds with applying the Reynolds-averaged Navier-Stokes (RANS) equations [3,7]

The averaging procedure for numerically solving turbulent flows decomposes the velocity into a mean and a fluctuating component, namely,

$$u_i = \bar{u}_i + u_i' \tag{13}$$

where $\bar{u}_i$ and u_i' are the mean and fluctuating Cartesian velocity components.

Substituting these variables to the conservation equations and taking the time average yield the continuity and momentum equations for a turbulent flow

$$\frac{\partial \rho}{\partial t} + \frac{\partial}{\partial x_i}(\rho u_i) = 0 \tag{14}$$

16

$$\frac{\partial}{\partial t}(\rho u_i) + \frac{\partial}{\partial x_i}(\rho u_i u_j)$$

$$= -\frac{\partial p}{\partial x_i} + \overline{u_i' F_j} + \frac{\partial}{\partial x_i}\left[\mu\left(\frac{\partial u_i}{\partial x_j} + \frac{\partial u_j}{\partial x_i} - \frac{2}{3}\delta_{ij}\frac{\partial u_i}{\partial x_i}\right)\right] \qquad (15)$$

$$+ \frac{\partial}{x_j}\left(-\rho\overline{u'_i u'_j}\right)$$

Reynolds averaging yields a term $-\rho\overline{u_i' u_j'}$ known as the Reynolds stress which must be modeled.

2.2.1 Closure Problems

The RANS method introduces a closure problem where the number of equations is less than the number of variables we need to solve. Turbulence modeling must be introduced which approximates the turbulence correlation of a certain order in terms of the mean flow variables. These turbulence models simulate the average characteristic of a real turbulence. These closure assumptions involve a combination of dimensional analysis and empirical constants. These empirical constants could be 'tuned' to give 'board agreement' with experiments in a wide range of flow configuration.

Turbulence modelling usually begins with the Boussinesq hypothesis which relates the Reynolds stress to the mean velocity gradients

$$-\rho\overline{u_i' u_j'} = \mu_t\left(\frac{\partial u_i}{\partial x_j} + \frac{\partial u_j}{\partial x_i}\right) - \frac{2}{3}\left(\rho k + \mu_t\frac{\partial u_k}{\partial x_k}\right)\delta_{ij} \qquad (16)$$

where the turbulent viscosity μ_t is computed from an empirical model based on the turbulent kinetic energy k and the specific dissipation rate ω, which is the ratio of ε, the dissipation rate, to k, the kinetic energy, using the Shear-Stress Transport (SST) $k–\omega$ model. The SST $k–\omega$

accounts for the transport of the turbulence shear stress in the definition of the turbulent viscosity, which makes it more accurate and reliable to wider class of flows, such as adverse pressure gradient flows.

$$\mu_t = \frac{\rho k}{\omega} \frac{1}{\max\left[\frac{1}{\alpha^*}, \frac{S \cdot F_2}{a_1 \omega}\right]} \tag{17}$$

The transport equations for the kinetic energy k and the specific dissipation rate ω are given by:

$$\frac{\partial}{\partial t}(\rho k) + \frac{\partial}{\partial x_i}(\rho k u_i) = \frac{\partial}{\partial x_j}\left(\Gamma_k \frac{\partial k}{\partial x_j}\right) + G_k - Y_k + S_k \tag{18}$$

$$\frac{\partial}{\partial t}(\rho \omega) + \frac{\partial}{\partial x_i}(\rho \omega u_i) = \frac{\partial}{\partial x_j}\left(\Gamma_\omega \frac{\partial \omega}{\partial x_j}\right) + G_\omega - Y_\omega + D_\omega + S_\omega \tag{19}$$

$$S = |S_{i,j}| \tag{20}$$

$$where: \ S_{i,j} = \frac{1}{2}\left(\frac{\partial u_j}{\partial x_i} + \frac{\partial x u_i}{\partial x_j}\right) \tag{21}$$

$$F_2 = \tanh(\phi_2^2) \tag{22}$$

$$\phi_2 = \max\left[2\frac{\sqrt{k}}{0.09\omega y}, \frac{500\mu}{\rho y^2 \omega}\right] \tag{23}$$

$$\alpha^* = \alpha_\infty^* \left(\frac{\alpha_o^* + Re_t/R_k}{1 + Re_t/R_k}\right) \tag{24}$$

where

$$\alpha_\infty^* = 1, \quad Re_t = \frac{\rho k}{\mu \omega}, \quad R_k = 6, \quad \alpha_o^* = \frac{\beta_i}{3}, \quad \beta_i = 0.072 \tag{25}$$

and where y is the distance to the next computational surface in the grid defined. Detailed definition of all parameters and constants is given in ANSYS® Fluent™ Theory Guide. [10] For this simulation default parameter values were used.

2.2.2 Porous Media Model.

The porous medium is modeled as a source term, in the momentum equation.

$$F_i = -\left(\sum_{j=1}^{3} D_{ij}\mu v_j + \sum_{j=1}^{3} C_{ij}\frac{1}{2}\rho|v|v_j \right) \tag{26}$$

where;

$\sum_{j=1}^{3} D_{ij}\mu v_j$ is the viscous loss term (Darcy's Law),

$\sum_{j=1}^{3} C_{ij}\frac{1}{2}\rho|v|v_j$ is the inertia loss term,

S_i is the source term of the momentum equation which contributes to pressure gradient in the porous medium proportional to the velocity or square of the velocity,

$|v|$ is the magnitude of the velocity

For a homogeneous porous medium

$$F_i = -\left(\frac{\mu}{\alpha} v_i + C_2 \frac{1}{2}\rho|v|v_j \right) \tag{27}$$

The transient term of the energy equation and the conduction flux term are treated in the porous medium model as

$$\frac{\partial}{\partial t}\left(\varepsilon\rho_f E_f + (1-\varepsilon)\rho_s E_s\right) + \nabla.\left(\vec{v}\left(\rho_f E_f + p\right)\right)$$

$$= \nabla.\left[k_{eff}\nabla T - \left(\sum_i h_i J_i\right) + (\bar{\bar{\tau}}.\vec{v})\right] + S_f^h \tag{28}$$

where E_f is the total fluid energy, E_s is the total solid medium energy, ε is the porosity of

the medium. $k_{eff} = \varepsilon k_f + (1-\varepsilon)k_s$ is the effective thermal conductivity of the medium where,

k_f is the fluid phase thermal conductivity (including the turbulent contribution, k_t) and k_s is the

solid medium thermal conductivity. The energy transfer due to conduction is given by $k_{eff}\nabla T$,

energy transfer due to diffusion is $\sum_i h_i J_i$, and energy transfer due to viscous dissipation is $\bar{\bar{\tau}}.\vec{v}$ with

S_f^h is the enthalpy source term.

2.3 Governing Equations for Axisymmetric Flow

For cylindrical coordinate the indices i and j represents: axial direction x, the angular

direction θ, and the radial direction r. The velocity vector $\vec{u} \equiv (u_x, u_\theta, u_r)$. For axisymmetric

flow it is assumed, that there is no flow in the angular direction $u_\theta = 0$, and the flow properties

are independent of the angular direction θ. Neglecting the effect of gravity, the governing

conservation equations for the axisymmetric flow are simplified to

$$\frac{\partial\rho}{\partial t} + \frac{\partial(\rho u_x)}{\partial x} + \frac{1}{r}\frac{\partial(\rho r u_r)}{\partial r} = 0 \tag{29}$$

$$\rho\left(\frac{\partial u_x}{\partial t} + u_x\frac{\partial u_x}{\partial x} + \frac{u_r}{r}\frac{\partial(ru_{x)}}{\partial r}\right) = -\frac{\partial p}{\partial x} + \frac{\partial(\tau_{xx})}{\partial x} + \frac{1}{r}\frac{\partial(r\tau_{rx})}{\partial r} + F_x \tag{30}$$

$$\rho\left(\frac{\partial u_r}{\partial t} + u_x\frac{\partial u_r}{\partial x} + \frac{u_r}{r}\frac{\partial(ru_{r)}}{\partial r}\right) = -\frac{1}{r}\frac{\partial rp}{\partial r} + \frac{\partial(\tau_{xr})}{\partial x} + \frac{1}{r}\frac{\partial(r\tau_{rr})}{\partial r} + F_r \tag{31}$$

where

$$\tau_{xx} = \mu \left(-\frac{2}{3} \nabla \cdot \vec{u} + 2\frac{\partial u_x}{\partial x} \right) \tag{32}$$

$$\tau_{rr} = \mu \left(-\frac{2}{3} \nabla \cdot \vec{u} + 2\frac{\partial u_r}{\partial r} \right) \tag{33}$$

$$\tau_{rx} = \tau_{xr} = \mu \left(\frac{\partial u_x}{\partial r} + \frac{\partial u_r}{\partial x} \right) \tag{34}$$

and the gradient $\nabla \cdot \vec{u}$ is given by

$$\nabla \cdot \vec{u} = \frac{\partial u_x}{\partial x} + \frac{1}{r}\frac{\partial (ru_r)}{\partial r} \tag{35}$$

The source term in the momentum equation to represent the porous medium is modeled as

$$F_x = \frac{\mu}{\alpha} u_x + \frac{C_2}{2} \rho u_x \sqrt{u_x^2 + u_r^2} \tag{36}$$

$$F_r = \frac{\mu}{\alpha} u_r + \frac{C_2}{2} \rho u_r \sqrt{u_x^2 + u_r^2} \tag{37}$$

Using the mathematical manipulation, the governing conservation equations are arranged in a way to make it possible for generalized vector notation and are given as:

$$\frac{\partial \rho}{\partial t} + \frac{\partial (\rho u_x)}{\partial x} + \frac{\partial (\rho u_r)}{\partial r} + \frac{1}{r}(\rho u_r) = 0 \tag{38}$$

$$\frac{\partial \rho u_x}{\partial t} + \frac{\partial (\rho u_x^2 + p)}{\partial x} + \frac{\partial \rho u_x u_r}{\partial r} + \frac{1}{r}(u_r u_x - \tau_{rx}) = \frac{\partial \tau_{xx}}{\partial x} + \frac{\partial \tau_{rx}}{\partial r} + F_x \tag{39}$$

$$\frac{\partial \rho u_r}{\partial t} + \frac{\partial (\rho u_x u_r)}{\partial x} + \frac{\partial (\rho u_r^2 + p)}{\partial r} + \frac{1}{r}(\rho u_r^2 + p - \tau_{rr})$$
$$= \frac{\partial (\tau_{xr})}{\partial x} + \frac{\partial \tau_{rr}}{\partial r} + F_r \tag{40}$$

Axisymmetric governing equations for chemically reacting, viscous, compressible flow, through a porous medium are given by

$$\frac{\partial U}{\partial t} + \frac{\partial F}{\partial x} + \frac{\partial G}{\partial r} = \frac{\partial Fv}{\partial x} + \frac{\partial Gv}{\partial r} + S \tag{41}$$

where U is the state vector, F is the flux vector in axial direction, G is flux vector in radial direction, H is the axisymmetric term, F_v is the viscous force in axial direction G_v is the viscous force in radial direction and S is the source term to account for the porous medium, external heat transfer, and the species source vector,

$$
U = \begin{bmatrix} \rho\varepsilon \\ \rho\varepsilon u_x \\ \rho\varepsilon u_r \\ \rho\varepsilon E \\ \rho\varepsilon Y_\alpha \end{bmatrix}
\qquad
F = \begin{bmatrix} \rho\varepsilon u_x \\ (\rho\varepsilon u_x{}^2 + p) \\ \rho\varepsilon u_x u_r \\ (\rho E + p)u_x \\ \rho\varepsilon u_x Y_\alpha \end{bmatrix}
\qquad
G = \begin{bmatrix} \rho\varepsilon u_r \\ \rho\varepsilon u_x u_r \\ (\rho\varepsilon u_r{}^2 + p) \\ (\rho E + p)u_r \\ \rho\varepsilon u_r Y_\alpha \end{bmatrix}
\tag{42}
$$

$$
H = \frac{1}{r}\begin{bmatrix} \rho\varepsilon u_r \\ \rho\varepsilon u_x u_r - \tau_{rx} \\ \rho\varepsilon u_r{}^2 + p - \tau_{rr} \\ (\rho E + p)u_r \\ \rho\varepsilon u_r Y_\alpha \end{bmatrix}
\qquad
F_v = \begin{bmatrix} 0 \\ \varepsilon\tau_{xx} \\ \varepsilon\tau_{xr} \\ \varepsilon(u_x\tau_{xx} + u_y\tau_{xr} + q_x) \\ \rho\varepsilon D Y_\alpha \end{bmatrix}
\tag{43}
$$

$$
G_v = \begin{bmatrix} 0 \\ \varepsilon\tau_{rx} \\ \varepsilon\tau_{rr} \\ \varepsilon(u_x\tau_{rx} + u_r\tau_{rr} + q_r) \\ \rho\varepsilon D Y_\alpha \end{bmatrix}
\qquad
S = \begin{bmatrix} 0 \\ F_x(1-\varepsilon) \\ F_r(1-\varepsilon) \\ h_v(T-T_o) \\ \varepsilon\dot{\omega}_\alpha \end{bmatrix}
\tag{44}
$$

$$\varepsilon = (open\ flow\ area)/(total\ area)$$

The source in the momentum equation are given by equation (36) and (37). For a Newtonian fluid the shear stress constitutive equations are given by equation (32), (33) and (34).

The heat transfer due to conduction is given by

$$q_x = (k + k_\tau) \frac{\partial T}{\partial x} \tag{45}$$

$$q_r = (k + k_\tau) \frac{1}{r} \frac{\partial rT}{\partial r} \tag{46}$$

where ρ is the density of the mixture; p is the pressure of the mixture; u_x and u_y are the velocities in x and y direction and ε is the coefficient of the porous medium, $\varepsilon = 1$ in full flow section and ε = porosity in the porous medium flow section, Y_α is the mass fraction of the species α, where α = 1, 2...N; and N is the total number of the species.

$$E = \sum_{\alpha=1}^{N} (Y_\alpha h_\alpha) - \frac{p}{\rho} + \frac{1}{2} (u_x^2 + u_r^2) \tag{47}$$

The dynamic viscosity is μ is given by the material properties and μ_τ, the turbulent viscosity is obtained by turbulence modelling. The laminar heat transfer coefficient is

$$k_L = \mu \frac{c_p}{Pr_L} \tag{48}$$

where Pr_L is the laminar Prandtl number and the turbulent heat transfer coefficient is

$$k_\tau = \mu_\tau \frac{c_p}{Pr_\tau} \tag{49}$$

where the Pr_τ is the turbulent Prandtl number. The diffusion coefficient is D

$$D = \frac{v}{Sc} \qquad (50)$$

Assumed to be the same for all species, where v is the kinematic viscosity, $v = \frac{\mu}{\rho}$, Sc denotes the Schmidt number. $\dot{\omega}$ in the chemical reaction source term. h_v is the coefficient of the volumetric heat transfer between the gas and solid region, T is the temperature of the gas-phase, and T_s is the temperature of the solid-phase. The permeability of the porous medium is α, and C_2 is the inertia resistance factor.

2.3.1 Porous Medium Model

The "momentum sink" term used to model the porous medium flow resistance is expressed using the Forchheimer equation

$$-\Delta P = a\bar{u} + b\bar{u}^2 \qquad (51)$$

where ΔP is the pressure drop across the porous medium, "a" is the Darcy coefficient, "b" is Forchheimer coefficient and $\bar{u}$ is the average velocity through the porous medium. In this research the coefficients "a" and "b" are determined from experimental flow test, conducted using a small-scale flame arrestor element sample.

Equating the axial "momentum sink" equation to the Forchheimer equation and substituting $\bar{u}$ with u_x will yield

$$S_x = -\left(\frac{\mu}{\alpha}u_x + C_2\frac{1}{2}\rho u_x^2\right) = -\frac{\partial p}{\partial x} \cong \frac{-\Delta P}{\Delta x} \qquad (52)$$

$$\left(\frac{\mu}{\alpha}u_x + C_2\frac{1}{2}\rho u_x^2\right)\Delta x = \Delta P = au_x + bu_x{}^2 \qquad (53)$$

The coefficients in the "momentum sink" equations are calculated from experimentally determined coefficients "a" and "b" using

$$\frac{1}{\alpha} = \frac{a}{\mu}, C_2 = \frac{2b}{\rho} \tag{54}$$

2.4 Thermodynamic Relations

2.4.1 Equation of State

The ideal gas equation for thermally perfect gas mixture in a volume, V, is given by Dalton's law as

$$p_i = \rho_i R_i T \tag{55}$$

$$p = \sum_{i=1}^{N_s} p_i \tag{56}$$

where p_i is partial pressure of species i, $\rho_i = \frac{m_i}{V}$ is density of the species i with the mass, m_i, and $R_i = \frac{R_u}{W_i}$ is the specific gas constant of species i, where R_u is the universal gas constant and W_i is the molecular weight of the species i. The total pressure, p, can be calculated from the partial pressure of the species, p_i, where N_s is the total number of the species.

2.4.2 Thermodynamic Properties of Species and a Mixture

For thermally perfect gas mixture, the specific heats, enthalpy and internal energy of a species i are a function of temperature only and are given by:

$$c_{pi} = f_1(T), \quad c_{vi} = f_2(T) \tag{57}$$

$$dh_i = c_{pi}dT, \quad de_i = c_{vi}dT \tag{58}$$

By integrating equation (58) we obtain the enthalpy of species i:

$$h_i(T) = h_i^f(T_{ref}) + \int_{T_{ref}}^{T} c_{pi}(T)dT \tag{59}$$

where $h_i^f(T_{ref})$ is called the heat of formation of the species i, at the reference temperature $T_{ref} = 298.15\ K$. The heat of formation is set to zero for species in their natural state, for example, heat of formation of oxygen $h_{O_2}^f = 0$. There are thermodynamic databases available for the heat of formation of most commonly found substances in combustion such as CEA [35]. The thermodynamic properties of species are determined using kinetic theory. However, most common or practical approach is to use the least-square fit of equation with seven coefficients [26].

The thermodynamic properties of the mixture, the specific heats and enthalpy are obtained from the species properties by

$$c_p(T) = \sum_{i=1}^{N_S} Y_i\, c_{pi}(T) \tag{60}$$

$$c_v(T) = \sum_{i=1}^{N_S} Y_i\, c_{vi}(T) \tag{61}$$

$$h(T) = \sum_{i=1}^{N_S} Y_i\, h_i(T) \tag{62}$$

$$e(T) = \sum_{i=1}^{N_S} Y_i\, e_i(T) \tag{63}$$

where $Y_i = \frac{m_i}{m_m}$ is the mass fraction of the species; and m_i is mass of the species i and m_m is total mass of the mixture.

The speed of sound "c" can be derived from thermodynamic relation for a perfect gas as

$$c^2 = \left(\frac{\partial p}{\partial \rho}\right)_v = \frac{\gamma p}{\rho} = \gamma RT \tag{64}$$

where the specific heat ratio $\gamma = c_p/c_v$, where c_p and c_v are the specific heat at constant pressure and volume respectively.

2.5 Rankine-Hugoniot Relations

Rankine-Hugoniot relations are equation derived from the governing conservation equations. These equations relate the initial and final conditions of a steady one-dimensional flow of combustible gas that burns to completion. In detonation, heat and radical diffusion do not control the velocity; rather, the shock wave structure of the developed supersonic wave raises the temperature and pressure substantially to cause very high reaction rates and energy release. The detonation wave propagation is sustained by this energy release. The detonation wave is highly three-dimensional; however, the one-dimensional analysis of detonation wave could give us insight and is presented in this section. A one-dimensional, steady, ideal perfect gas with no heat transfer and negligible body force is considered for this analysis. The detonation wave is fixed in the laboratory frame of reference.
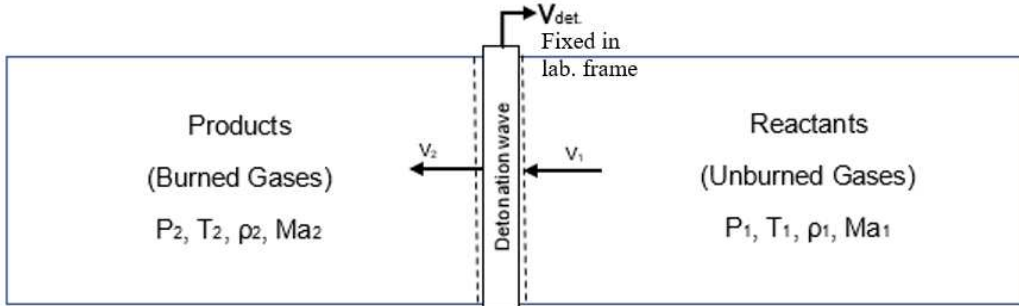
Figure 2-1 One-dimensional detonation propagation schematics

Mass Conservation:

$$\dot{m} = \rho_1 v_1 = \rho_2 v_2 \tag{65}$$

Momentum conservation: only pressure force acting on the control volume.

$$P_1 + \rho_1 v_1^2 = P_2 + \rho_2 v_2^2 \tag{66}$$

Energy conservation:

$$h_1 + \frac{v_1^2}{2} = h_2 + \frac{v_2^2}{2} \tag{67}$$

By splitting the total enthalpy to sensible and heat of formation contributions:

$$h(T) = \sum Y_i h_{fi}^o + \sum Y_i \int_{T_o}^{T} C_{pi} dT \tag{68}$$

with the constant specific heat assumption

$$h(T) = \sum Y_i h_{fi}^o + C_p(T - T_o) \tag{69}$$

substituting into the energy equation

$$C_p T_1 + \frac{v_1^2}{2} + \sum_{state\ 1} Y_i h_{fi}^o - \sum_{state\ 2} Y_i h_{fi}^o = C_p T_2 + \frac{v_2^2}{2} \tag{70}$$

where

$$\sum_{state\ 1} Y_i h_{fi}^o - \sum_{state\ 2} Y_i h_{fi}^o = q \ (heat\ addition) \tag{71}$$

the energy equation becomes

$$C_p T_1 + \frac{v_1^2}{2} + q = C_p T_2 + \frac{v_2^2}{2} \tag{72}$$

Ideal gas assumption:

$$P_1 = \rho_1 R_1 T_1$$
$$\tag{73}$$
$$P_2 = \rho_2 R_2 T_2$$

The Rayleigh line equation is formulated by combining the mass conservation equation and the momentum conservation equations

$$\frac{P_2 - P_1}{1/\rho_2 - 1/\rho_1} = -\dot{m}^{"2} \tag{74}$$

For a fixed mass flow rate $\dot{m}$ and initial conditions P_1 and ρ_1

$$P = a\left(1/\rho_2\right) + b \tag{75}$$

where $a = -\dot{m}^{"2}$ and $b = P_1 + \dot{m}^{"2}\left(1/\rho_1\right)$
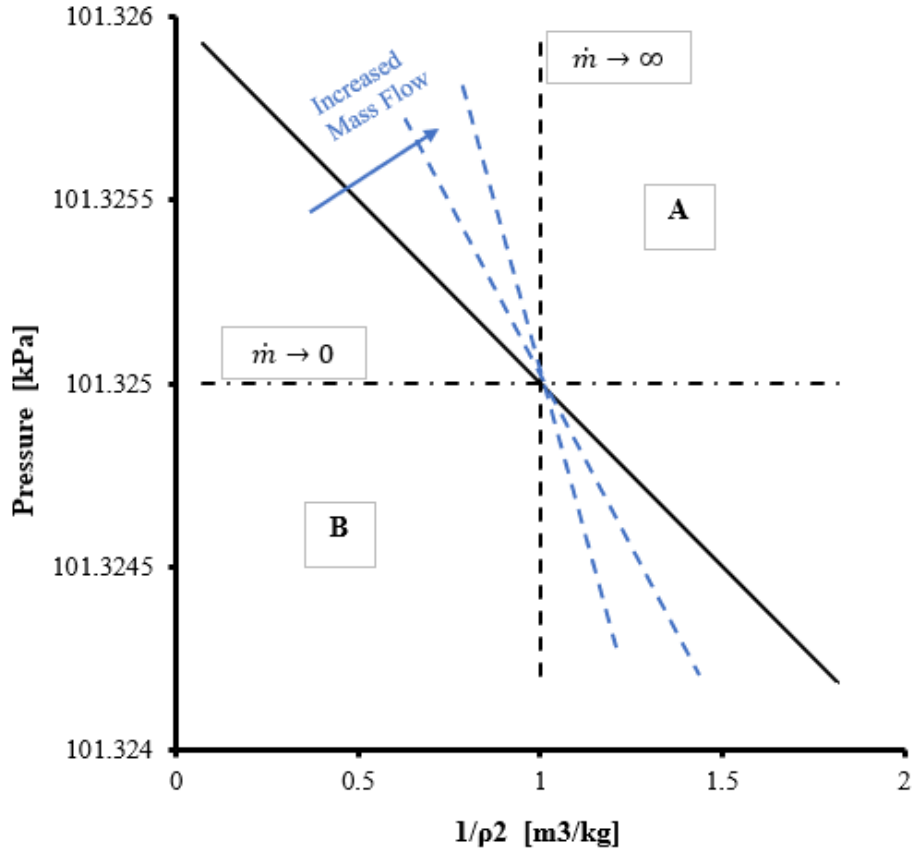
Figure 2-2 Rayleigh line

The two quadrant, A and B, are physically inaccessible regions. The Rankine-Hugoniot relation is obtained when we require that the energy equation be satisfied in addition to the continuity and momentum equations. Combining the continuity, momentum and energy conservation equations and using the ideal gas relationship, $\gamma \equiv C_p/C_v$, we obtain,

$$\frac{\gamma}{\gamma - 1}\left(\frac{P_2}{\rho_2} - \frac{P_1}{\rho_1}\right) - \frac{1}{2}(P_2 - P_1)\left(\frac{1}{\rho_1} + \frac{1}{\rho_2}\right) - q = 0 \tag{76}$$

For a given initial conditions, $P1$ and $\rho1$ and if we assume q is given parameter calculated from the reaction mechanism, we could develop relation $P2$ as a function of $1/\rho_2$, or in general P as function of $1/\rho$

30

$$\frac{P_2}{P_1} = \frac{\left(\frac{\gamma+1}{\gamma-1}\right)\frac{\rho_2}{\rho_1} - 1 + 2q\frac{\rho_2}{P_1}}{\frac{\gamma+1}{\gamma-1} - \frac{\rho_2}{\rho_1}} \tag{77}$$
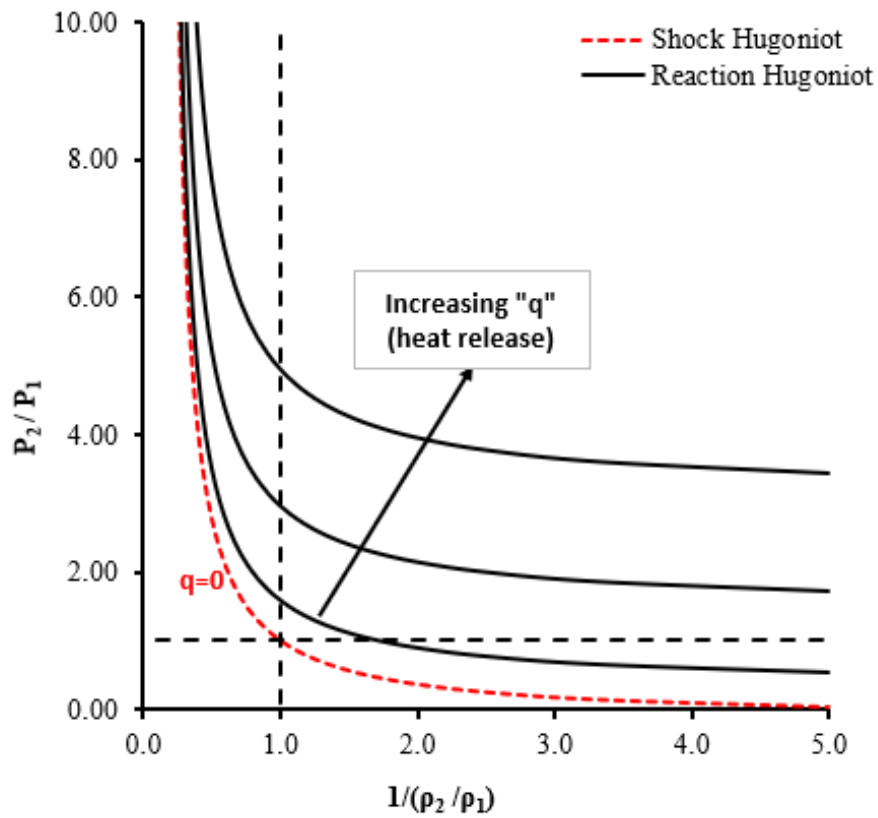
Figure 2-3 Rankine-Hugoniot relations

Combining the Rayleigh line and the the Rankine-Hugonoit relation gives the CJ point (where the Rayleigh line equation is tangent to the Rankine-Hugonoit equation)
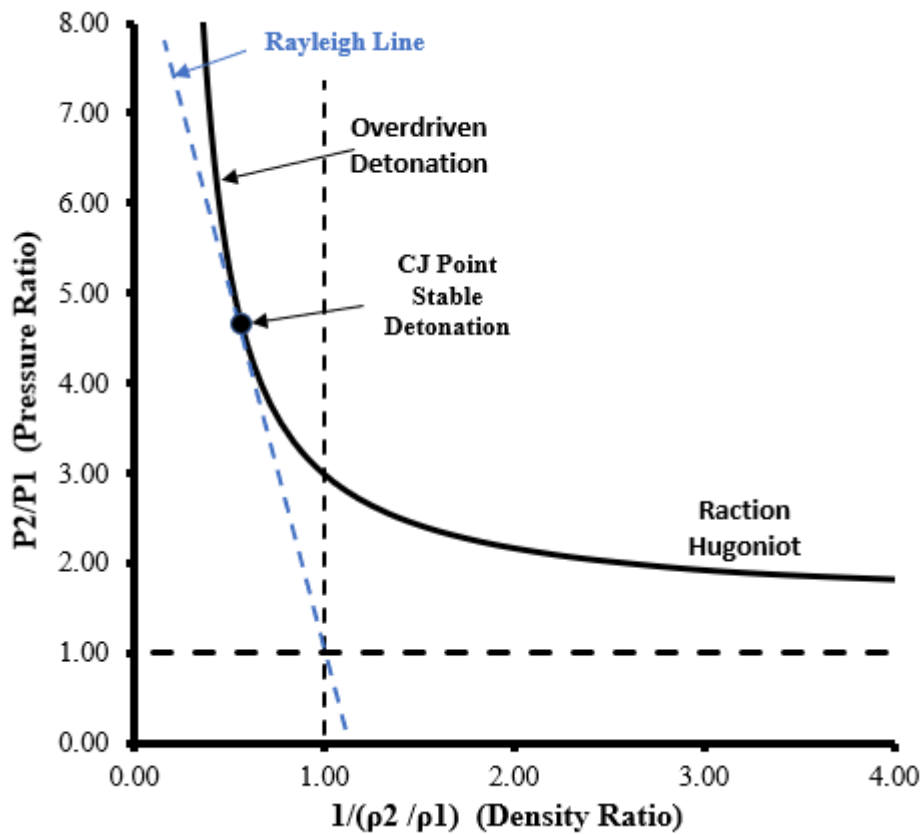
Figure 2-4 Rankine-Hugoniot relations & the Rayleigh line

2.6 Chemical Kinetics

Turbulence-chemistry-interaction (TCI) is neglected in the numerical model used to calculate the detonation propagation. The chemical source term and the reaction is computed using the general reaction-rate expressions, without involving the effects of turbulence. For analysis involving detonation, where complex reaction is taking place, this approach is appropriate. The mass production rate in the source term is due to the chemical reaction, which is the rate of formation or destruction of a chemical species.

The hydrogen-oxygen reaction kinetic mechanism used in the detonation propagation study is obtained from the Lawrence Livermore National Laboratory LLNL-WEB-670918 database [26]. The hydrogen-oxygen elementary reaction mechanism with 21-step reactions and 10 species, the thermodynamic database and the transport parameters are directly imported into ANSYS®™ Fluent™. The 21-step reaction mechanism has 19-step elementary reaction mechanisms with two of them repeated and eight reacting chemical species (H, HO$_2$, H$_2$, H$_2$O, H$_2$0$_2$, O, OH, O$_2$) and two inert species (Ar, N$_2$). The reaction mechanism and the thermodynamic data are developed in CHEMKIN format and verified by M. O'Conaire et-al [24] using experimental and numerical investigation in a wide range of temperatures, pressures and equivalence ratios. These data are presented in Appendix A Table A.1 (reaction mechanism), Table A.2 (thermodynamic data) and Table A.3 (transport parameters)

The transport properties, viscosity, thermal conductivity and mass diffusion in the governing equations for each species must be solved using classical kinetic theory. The mixture property is obtained from the species properties using a mixture-averaged approach. The transport property database of Hydrogen-2004 [37] is used to evaluate the viscosity coefficient, thermal conductivity and diffusion coefficient for each species and is shown in Table A-3 in Appendix A. Column 2 in the Table A-3 indicates a molecular geometrical configuration: 0 for a monatomic molecule, 1 for linear molecule and 2 for non-linear molecule. Column 3 is the Lennard-Jones potential well depth ε/kg in Kelvin, column 4 is the Lennard collision diameter σ in Angstrom, column 5 is the dipole moment $\overline{\mu}$ in Debye, the sixth column is the polarization α in cubic Angstrom and the last column is the rotational relaxation number Z_{rot}^*.

This database is directly imported to Fluent™ to calculate the mixture-average properties in the detonation propagation simulation. The viscosity is related to the velocity gradient in the

momentum equation, the heat conduction is related to temperature gradient in the energy equation and the mass diffusion is related to the mass concentration gradient in the species continuity equation.

2.6.1 Rate of Mass Production

The general equation and definition of reaction mechanisms and thermodynamic data is presented in this section [2]. The chemical source term in the governing conservation equation usually proceeds through a series of elementary reactions called a chemical mechanism. In a system where N_s species participate in a mechanism with N_R reactions, each elementary mechanism reaction could be written as:

$$\sum_{i=1}^{N_s} v'_{i,r} \mathcal{M}_i \rightleftarrows \sum_{i=1}^{N_s} v''_{i,r} \mathcal{M}_i \tag{78}$$

where the indices i are for species and indices r are for reactions; $v'_{i,r}$ is the stoichiometric coefficient for reactant i and reaction r, $v''_{i,r}$ is the stoichiometric coefficient for the product i in the reaction r, $\mathcal{M}_i$ denotes the molar concentration of species i and it is given by

$$\mathcal{M}_i = \frac{\rho_i}{W_i} \tag{79}$$

where W_i is the molecular weight of species i, N_s number of chemical species in the system, N_R number of chemical reactions in the system.

The net rate of mass production of species i, that is used in the species conservation governing equation [10] is computed from the summation over the rate equations of all the elementary reactions as follows:

$$\omega_i = \sum_{r=1}^{N_R} (v_{i,r}'' - v_{i,r}') \left\{ k_{f,r} \prod_{i=1}^{N_s} [\mathcal{M}_i]^{v_{i,r}'} - k_{b,r} \prod_{i=1}^{N_s} [\mathcal{M}_i]^{v_{i,r}''} \right\} \tag{80}$$

where $k_{f,r}$ forward rate constant for reaction r and $k_{b,r}$ is backward rate constant for reaction r. The forward reaction rate constant, $k_{f,r}$, in the reaction r is computed from the Arrhenius expression

$$k_{f,r} = A_r T^n e^{\frac{-E_r}{RT}} \tag{81}$$

and the backward reaction rate constant $k_{b,r}$ is calculated from the forward reaction rate constant

$$k_{b,r} = k_{f,r}/K_r \tag{82}$$

where K_r is the equilibrium constant for the rth reaction computed from the thermodynamic properties.

When more energy is released in bonding or is required in splitting the molecules a third-body designated by "M" appears in the elementary reaction equations; see Table A-1 in Appendix A elementary reaction # 6. The net rate of mass production is calculated using

$$\omega_i = \sum_{r=1}^{N_R} (v_{i,r}'' - v_{i,r}')[M_i] \left\{ k_{f,r} \prod_{i=1}^{N_s} [\mathcal{M}_i]^{v_{i,r}'} - k_{b,r} \prod_{i=1}^{N_s} [\mathcal{M}_i]^{v_{i,r}''} \right\} \tag{83}$$

When there is third-body is involved in the reaction. The concentration of the third-body M_i is defined as

$$M_i = \sum_{i=1}^{N_s} \alpha_{ir} [\mathcal{M}_i] \tag{84}$$

where α_{ir} is the third-body efficiency factor of species i in the reaction r.

CHAPTER 3

NUMERICAL METHODS AND VALIDATION

3.1 Porous Medium Model Validation

The flame arrestor element is made from small isosceles triangular channels formed by crimping sheet metal. The key design characteristic in application where inline-flame arrestors are used is the pressure drop. The pressure drop across the flame arrestor element is predominantly associated with the crimp design. Modeling the fluid domain in an individual triangular channel is difficult and computationally intensive. Therefore, the porous medium model is developed for the arrestor flame element for numerical simulation.

3.1.1 Experimental Flow Test of the Small-Scale Arrestor Element

A small-scale arrestor element sample is shown in Figure 3-1. The sample is mounted in a special housing to run the flow test at the Emerson Flow Test Laboratory in McKinney, Texas, USA.
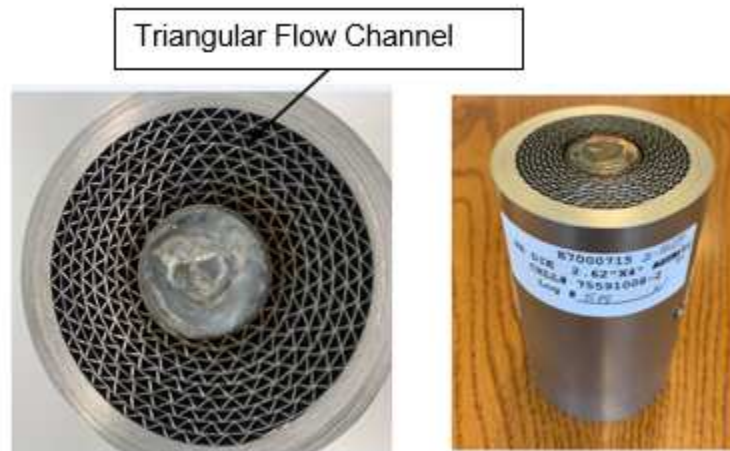

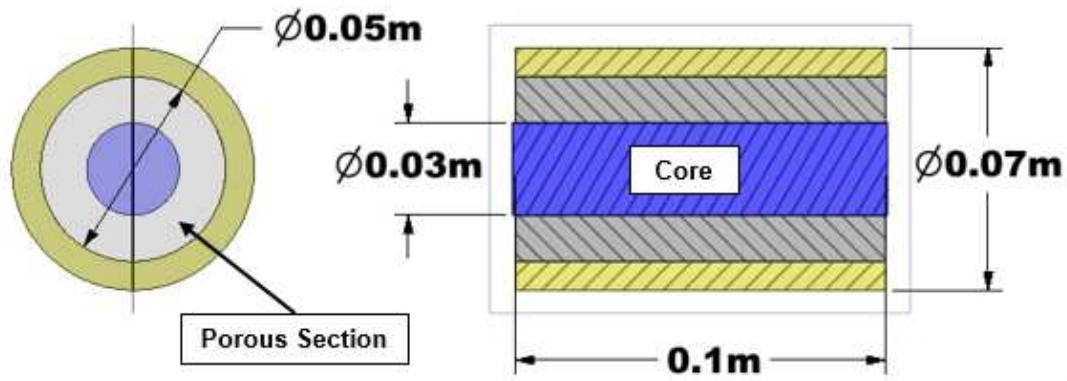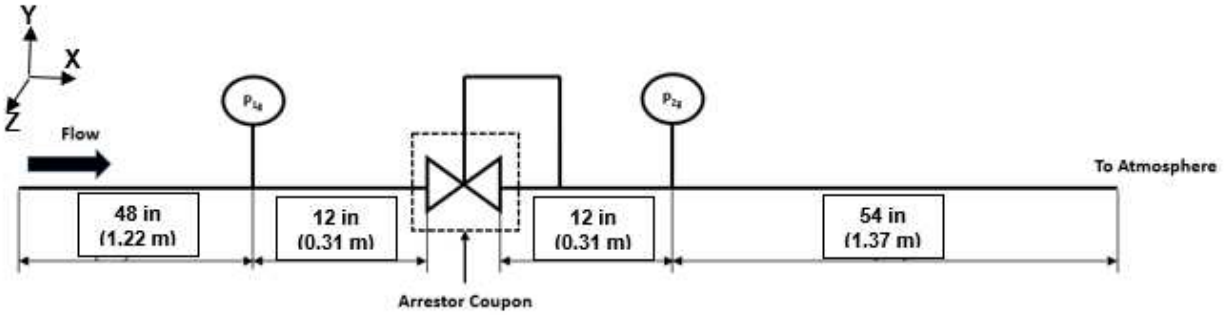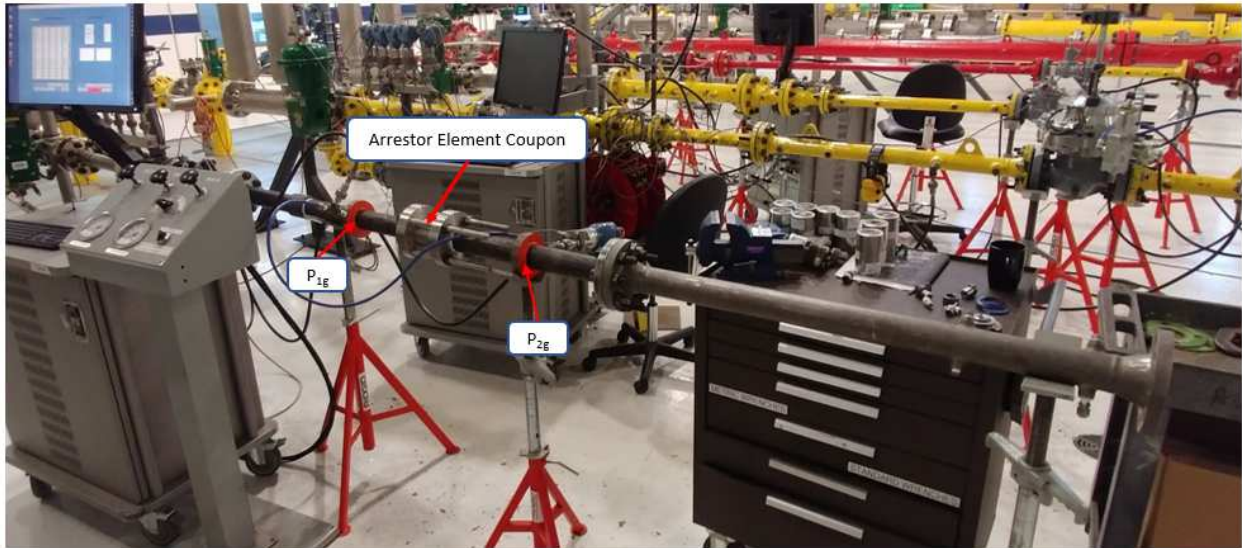Figure 3-1Small scale flame arrestor element photograph

Figure 3-2 Small-scale flame arrestor element drawing

A schematic of the test setup is shown in Figure 3-3(a) and a photograph is shown in Figure 3-3(b). The test is conducted with air at standard temperature and pressure. The inlet and outlet pipe are made of 0.0508 m (2 in) diameter, schedule 40 stainless steel pipe. The sample is mounted 1.53 m (60 in) downstream of the pipe opening that is connected to an air supply (not shown) to vary the inlet pressure $P1 = 0-69,000\ Pa\ (0-10\ psi)$. The inlet pressure $P1$ is measured at 0.31 m (12 in) ahead of the arrestor element sample. The pressure of the flow leaving the sample $P2$ is measured at 0.31 m (12 in) downstream. The flow then left the pipe to the atmosphere through an additional 1.37m (54 in) pipe. The pressure measurements were made with Rosemount-3051model pressure transmitters rated for 0-446,000 Pa abs (0 – 50 psi) with an uncertainty of 2 percent (full scale). The flow rate measurement is performed with a Micro-Motion CMF200 Coriolis flowmeter with a range of 0-2,800 sm^3/h (0–100,000 SCFH) with an uncertainty of 2 percent (full scale). Data were acquired by a National Instruments data acquisition system sampled at 20/s. Five data points were obtained for each measurement and averaged.

(a)

(b)

Figure 3-3 Small-scale flame arrestor element test setup
(a). Schematic, (b). Photograph

3.1.2 Arrestor Element Sample Flow Test Results

The average velocity of the flow is obtained simply from the volumetric flow rate as

$$\bar{u} = \frac{4Q}{\pi d^2}$$

(85)

where Q is the volumetric flow rate and d is the internal diameter of the pipe.

The average outlet velocity calculated from the experimental flow rate data ranges from 1.8 m/s to 150 m/s for pressure drop 0.003 kPa to 65 kPa.

The Reynolds number $Re = \frac{\rho \bar{u} L}{\mu}$, where L is the characteristic length, is calculated to determine the flow regimes. The characteristics length used for the Reynolds number calculation in the inlet and outlet pipe is the inside diameter of the pipe, 0.0525m (2.067 in) and the characteristics length used to calculate the Reynolds number in the arrestor element sample is the hydraulic diameter of the triangular channel in the sample element, 0.00141m (0.0555 in). Using the properties of the flow medium, air, at STP conditions, the Reynolds number in the inlet and outlet pipe ranges from 6,300 to 529,000 which is well in the turbulent region for internal pipe flow [5], for the test conditions used in the experiment. The Reynolds number in the arrestor sample element ranges from 160 to 14,000, which is within the laminar or transition regime. However, considering the flow regimes in the porous medium model [12], the flow in the arrestor element sample is in the high inertia region where the Forchheimer relation is valid.

Figure 3-4 shows a plot of the pressure drop $\Delta P = P_1 - P_2$ versus the average velocity. The experimental data for the pressure-drop versus the velocity is shown with small blue dots. A least-squares quadratic fit passing through the origin to the experimental data is performed and is shown on Figure 3-4 by a black line. The quadratic equation is given by

$$-\Delta P = 75.1\bar{u} + 2.41\bar{u}^2 \tag{86}$$

The correlation coefficient of the curve fit is $r^2 = 0.9995$. Hence the Forchheimer constants are determined to be $a = 75.1 \pm 1.1$ kPa·s/m and $b = 2.41 \pm 0.01$ kPa·s²/m²
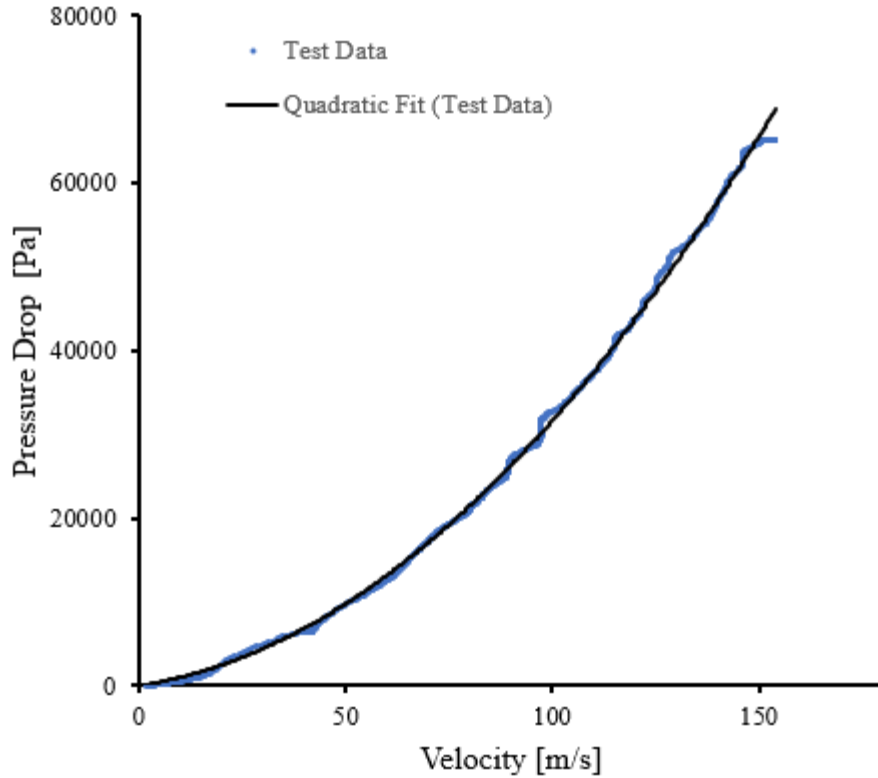
Figure 3-4 Small scale flame arrestor element pressure drop vs. velocity

3.1.3 Numerical Flow Simulation Through the Small-Scale Arrestor Element Sample

The numerical flow simulation is conducted using ANSYS® Fluent™. The flow domain consisted of the inlet, outlet pipes represented by fluid domain, and the arrestor element represented by a porous medium model with solid core where the flow is partially blocked.
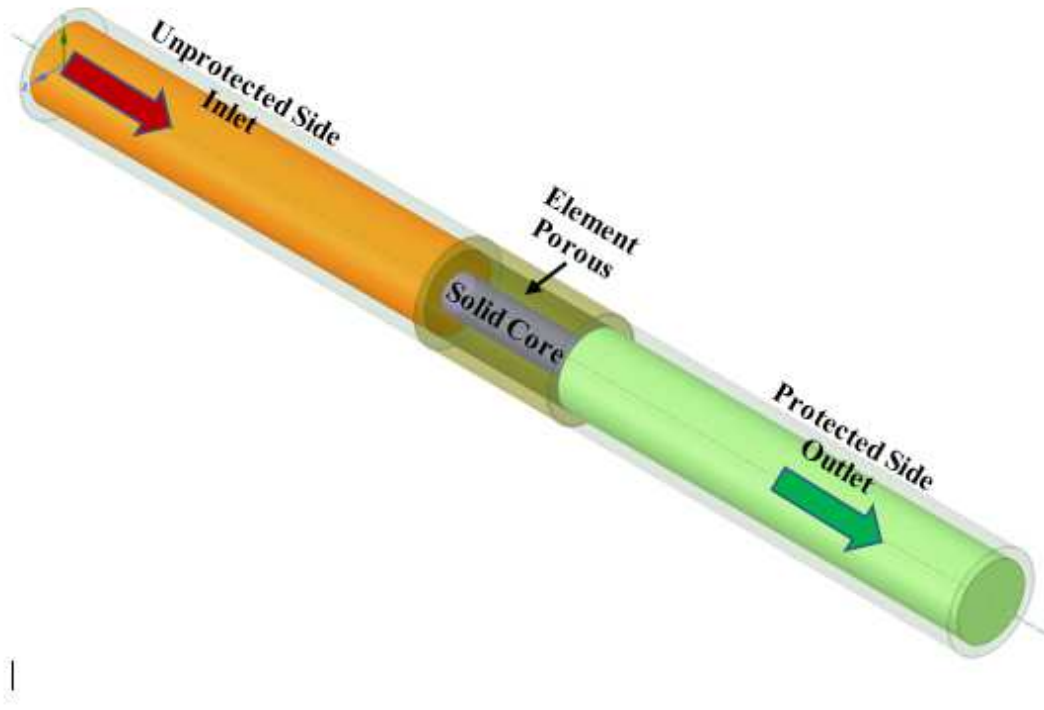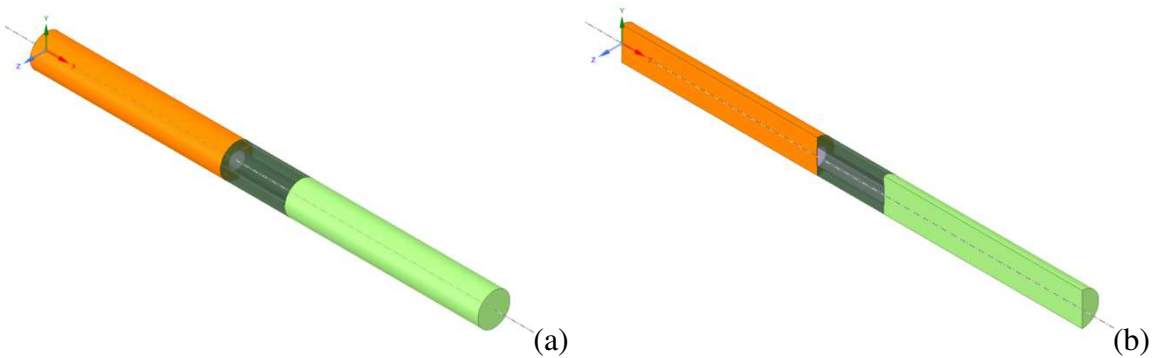
Figure 3-5 Small scale flame arrestor element simulation domain

3.1.4 Model Dependence Studies

Numerical flow simulation studies were conducted on three simulation models. The three-dimensional-full-geometry model, the three-dimensional-half-geometry model and the two-dimensional axisymmetric model.

(a)   (b)
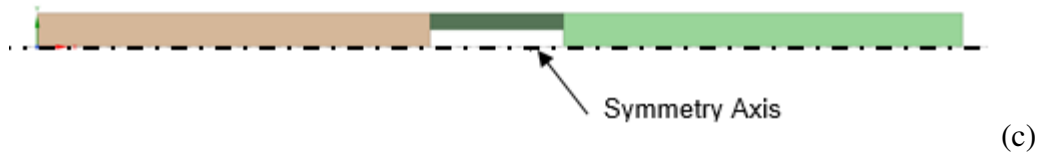
Symmetry Axis

(c)

Figure 3-6 Flow simulation domain models
(a) 3D full geometry, (b) 3D half geometry, (c) 2D axisymmetric

The simulation model boundary conditions were setup exactly as the experimental test setup and it is shown in Figure 3-7.
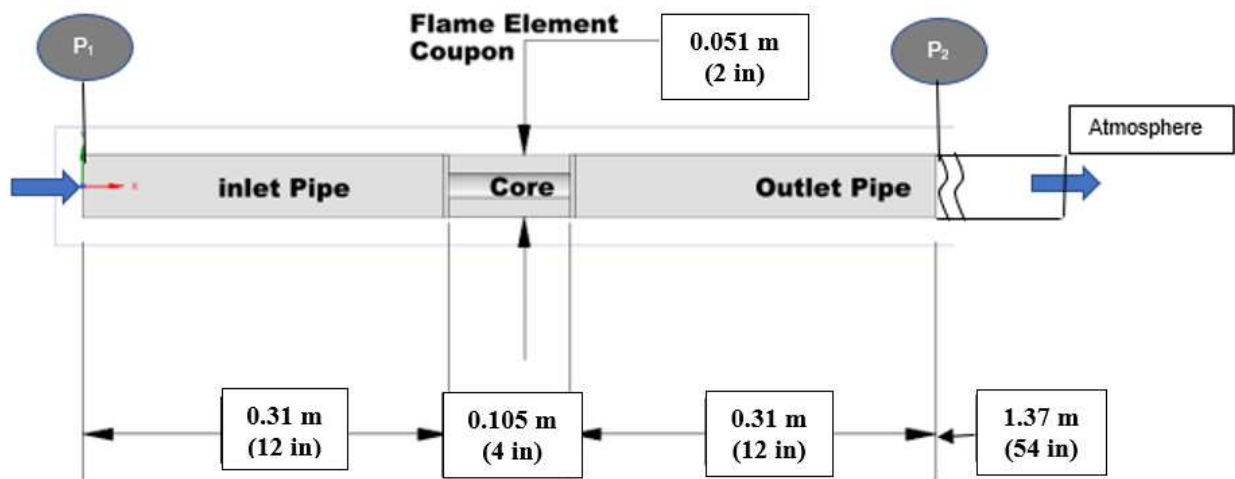

Figure 3-7 Arrestor element numerical flow simulation domain drawing

The two-dimensional axisymmetric model has 13,224 elements, the two-dimensional half model has 361,923 elements which is more than 25 times the axisymmetric model. The three-dimensional full model has 1,428,682 elements which is more than 100 times the axisymmetric model.

The inlet boundary condition is set to the pressure $P1$ which varies from $100 – 70,000$ Pa gauge pressure, and the outlet is set to atmospheric, namely, 0 Pa gauge pressure. The boundary

condition on the wall is set to the no-slip condition for the velocity and the thermal boundary condition is set to adiabatic. The fluid is air as ideal gas at standard temperature and pressure. The flow is turbulent flow and is solved using the Reynolds Averaged Navier-Stokes (RANS) equations. The turbulence is modeled using the Shear Stress Transport, SST k-ω model. Fluent™ default settings were used for the SST k-ω model empirical parameters. Laminar flow is used to resolve the flow in the porous medium, arrestor element region. The porous medium model parameters, the permeability and inertia resistance factor were calculated from the Forchhiemer equation developed from the experimental test data as described previously. The porosity is calculated from the crimped arrestor element geometry.

The mass flow rate comparison at 13800 Pa (2 psi) pressure drop for the three models is presented in Table 3-1. The overall mass flow rate comparison for the pressure drop 0 to 69,000 Pa (0 to 10 psi) for all mesh sizes is shown in Figure 3-8 and the outlet velocity profile comparison is presented in Figure 3-9.

Number of Elements	Number of Nodes	Model Type	Mass flow Rate [kg/s]
13224	14285	2d-axisymmetric model	0.1371
361774	383493	3d-half model	0.1366
1428682	1415379	3d-full model	0.1367

Table 3-1 Mass flow rate comparison at 13800 Pa (2 psi) for different models
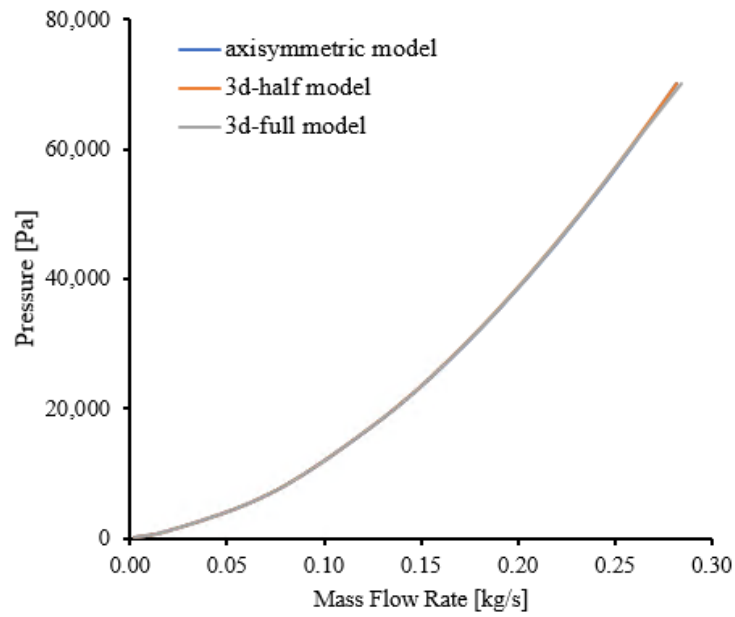
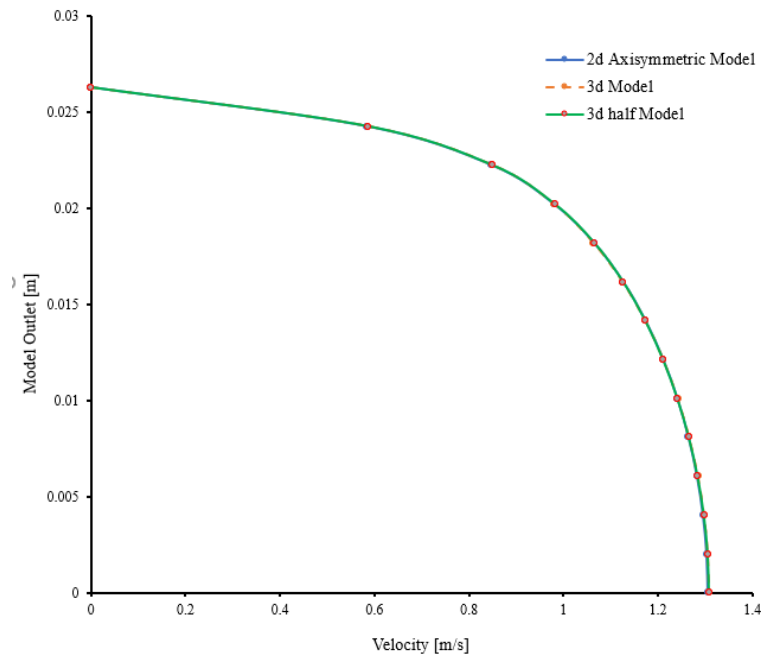Figure 3-8 Mass flow rate comparison for different models

Figure 3-9 Outlet velocity profile comparison for different models

There is no significant difference between the 2D-axisymmetric model, the 3D-full model and the 3D-half model.

3.1.5 Mesh Dependence Studies

   The mesh dependence study is conducted using the two-dimensional axisymmetric model. The simulation domain boundary conditions and physical parameters were set as described previously for model dependence study. Grid sizes of 0.5 mm, 1 mm and 2 mm were evaluated. The simulation results of these three grid sizes were compared to each other. Table 3-2 shows the comparison of mass flow rate calculated using numerical simulation for different mesh sizes and experimental result at 13800 Pa (2 psi) pressure drop. The overall mass flow rate comparison for a pressure drop 0 to 69,000 Pa (0 to 10 psi) for all mesh sizes is shown in Figure 3-10.

Number of Elements	Number of Nodes	Element Size [m]	Mass flow Rate [kg/s]
216087	220302	5×10^{-4}	0.1368
53631	55751	1×10^{-3}	0.1369
13224	14285	2×10^{-3}	0.1371

Table 3-2 Mass flow rate comparison at 13800 Pa (2 psi) for different mesh sizes
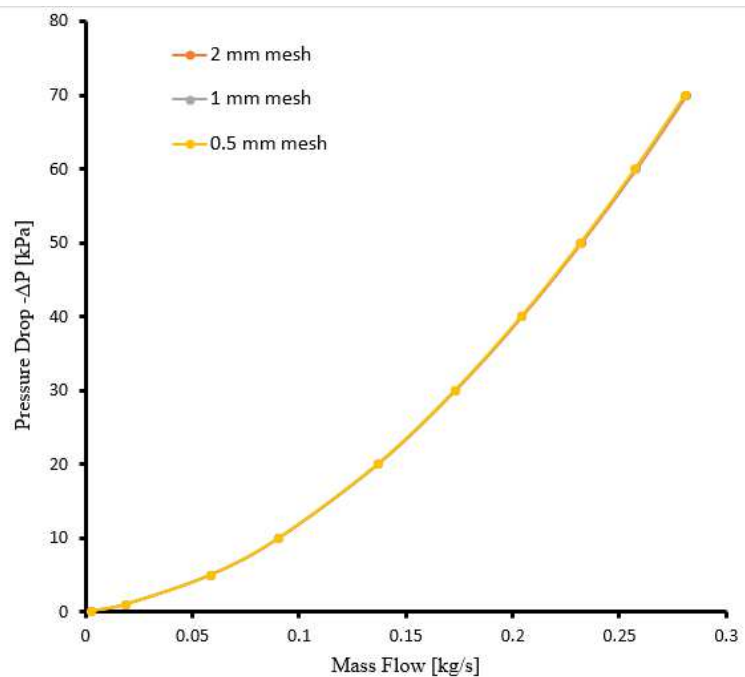

Figure 3-10 Mass flow rate comparison graph for different mesh sizes

The difference in numerical flow simulation result is independent of the grid size, the mass flow calculated is using different grid size has less than 0.5 % variation. Based on the geometrical model evaluation and the mesh dependence study, an axisymmetric model discretized using 2mm grid is used for numerical flow simulation in the flame arrestor applications.

3.1.6 Numerical Simulation Result Comparison to Experimental Data

The numerical simulation result using the porous medium model were compared to experimental data. Pressure drop versus outlet velocity is shown in Figure 22. The trend of the graph is the same as the experimental data; however, parameters of the porous medium model needs to be adjusted to obtain satisfactory comparison.
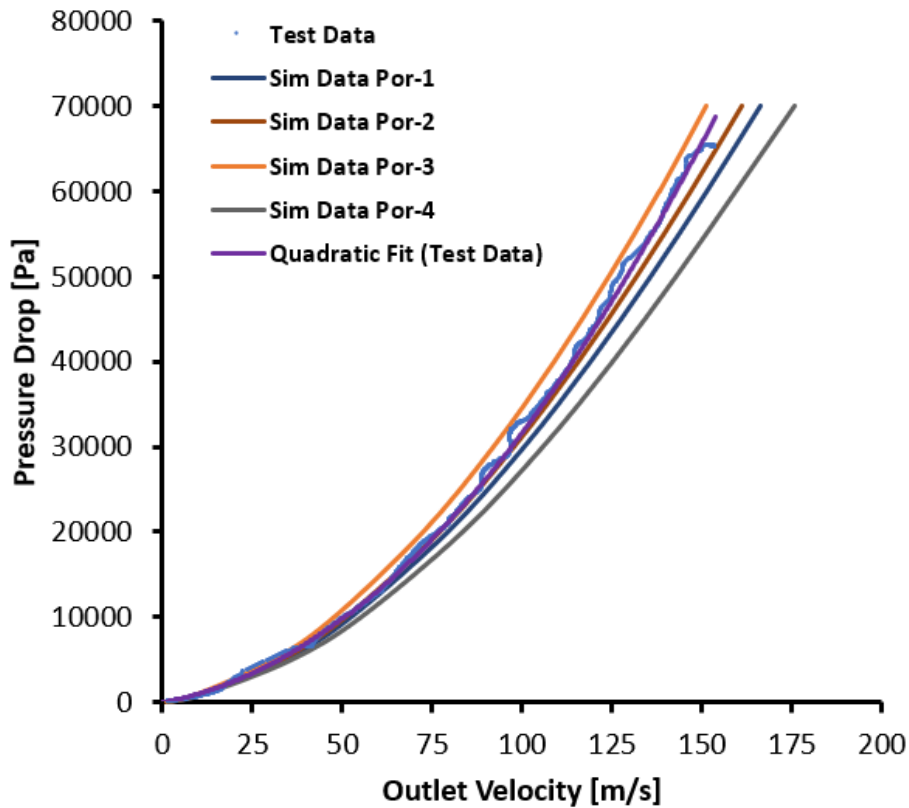

Figure 3-11 Flow simulation result compared to test data

The input parameters for the porous medium model are; the permeability $\frac{1}{\alpha}$ calculated from the Forchheimer viscous resistance coefficient "a", the inertia resistance factor C_2 calculated from coefficient "b" in the Forchheimer equation and the porosity of the medium defined as the passage area open to the flow divided by the total area of the flow. The Forchheimer coefficients "a" and "b" are derived from experimental test data. The porosity of the medium is calculated from the design of the crimped arrestor element. The calculated porosity value does not consider the variation in the manufacturing of the crimping and the rolling process. Inspecting the sample used for testing, there is some area, where the triangular channel is deformed at the start and end of rolling the crimped geometry, due to inherent process of spiral rolling. It should be expected also that due to the tension applied during the rolling process that there will be some additional deformation and variation of the crimped geometry.

3.2 Detonation Propagation Numerical Simulation

A series of numerical simulations were conducted using the ANSYS® Fluent™ CFD software to verify the capabilities of simulating detonation propagation in flame arrestor applications using the porous medium model. Fluent™ has well proven capabilities in solving complex, compressible reacting flow problems. In this research, in addition to the complex physics for the detonation propagation in the flame arrestor application, the complicated flow geometry in the flame arrestor element geometry is an added challenge.

3.2.1 Detonation Tube Simulation.

A two-dimensional axisymmetric chemically reacting flow in a detonation tube is used for verifying the numerical method. The detonation tube is modeled using a 50 mm long tube and a 5

47

mm diameter axisymmetric domain, see Figure 3-12. This tube is filled with a hydrogen–oxygen stoichiometric mixture with initial condition of 101.3kPa pressure and 300 K temperature. The left wall of the simulation domain is set to wall boundary condition and the right side is set to outlet boundary condition, where the atmosphere outside of the simulation domain is set to stoichiometric hydrogen-oxygen mixture at 101.3 kPa and 300K. Ignition is accomplished by patching four to five cells, ~ 2 mm width, of the simulation domain by the left wall of the tube with initial condition of 3.55 MPa pressure, 3500 K temperature and stoichiometric hydrogen–oxygen detonation species predicted by the NASA chemical equilibrium analysis program (CEA) [37] presented in Table 3-3.
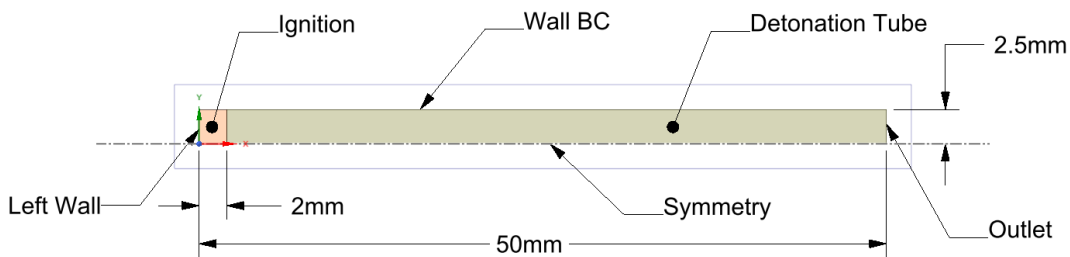

Figure 3-12 Detonation tube computational domain

Items	H	HO2	H2	H2O	H2O2	O	OH	O2
Mass Fraction	0.005564	0.00042	0.022537	0.660831	0.000047	0.041296	0.165947	0.103357

Table 3-3 Ignition domain chemistry

A 21-step hydrogen–oxygen chemical reaction mechanism, with 19 elementary reactions and 2 repeating reactions, and 10 species is used for simulation. The reaction mechanism used for this simulation is verified and prepared in CHEMIKIN format by O'Conaire et-al. [23]. The chemical kinetics mechanism, thermodynamics parameters and the transport parameters are down loaded from Lawrence Livermore National Laboratory [36] and directly imported to the Fluent™

solver to resolve the species reaction mechanism and they are presented in Table A1, Table A2 and Table A3 respectively. A stiff chemistry solver with In-Situ Adaptive Tabulation (ISAT) integration method is used to accelerate the calculation [10].

To resolve the detail of the detonation wave characteristics, the governing equation are discretized using an explicit spatial and temporal method. A density based coupled flow solver, which implements a finite volume approach is used. The flux vectors are computed using the second-order accurate Advection Upstream Splitting Method (AUSM) scheme, since this scheme is suitable for resolving flows with discontinuities and adverse pressure gradients. The transient solver utilizes the 4th-order Runge-Kutta time integration scheme for the explicit time stepping. The Courant-Friedrichs-Lewy (CFL) condition is used to adjust the time step based on the mesh size to assure convergence of the solution. Details of the ANSYS® Fluent™ solver setting are presented in Appendix B, Table B-1

3.2.2 Detonation tube mesh sensitivity analysis

An inviscid chemically reacting flow simulation of the detonation tube is conducted numerically using different grid sizes to study mesh sensitivity. The detonation characteristics, detonation wave speed, pressure and temperature were compared to CEA values [37]. Table 3-1 shows the comparison of the numerical simulation result with different grid sizes to the CEA result. Figure 3-13(a) shows detonation speed comparison and Figure 3-13(b) shows detonation temperature comparison. From the mesh sensitivity analysis, the 0.1 mm mesh axisymmetric model simulation result is within 3% of the CEA result. Thus, in this research axisymmetric model with 0.1 mm mesh is used for detonation propagation study Figure 3-14(a) and Figure 3-14(b) shows pressure and temperature time chart respectively.

Number of Elements	Number of Nodes	Element Size [mm]	u_D [m/s]	p_s [atm]	T_D [K]
CEA	-	-	2836	18.66	3676
12500	13026	1×10^{-4}	2758	17.48	3675
50001	51052	5×10^{-5}	2759	15.70	3658
139408	141154	3×10^{-5}	2575	15.40	3598

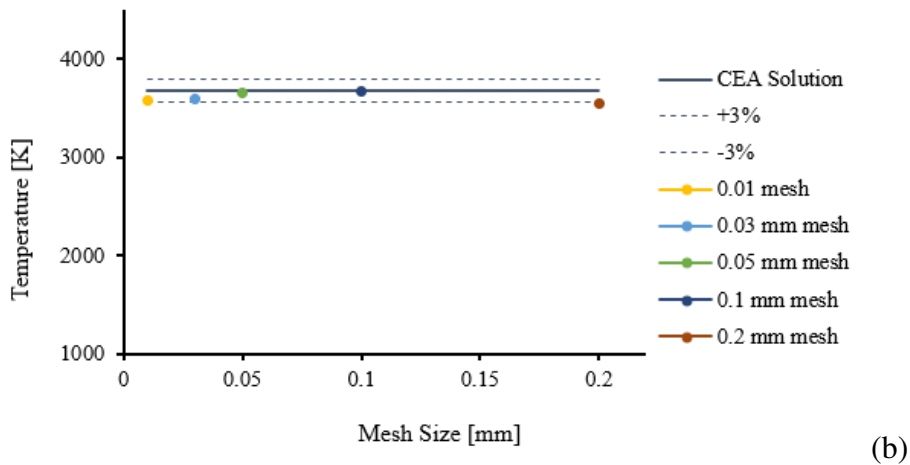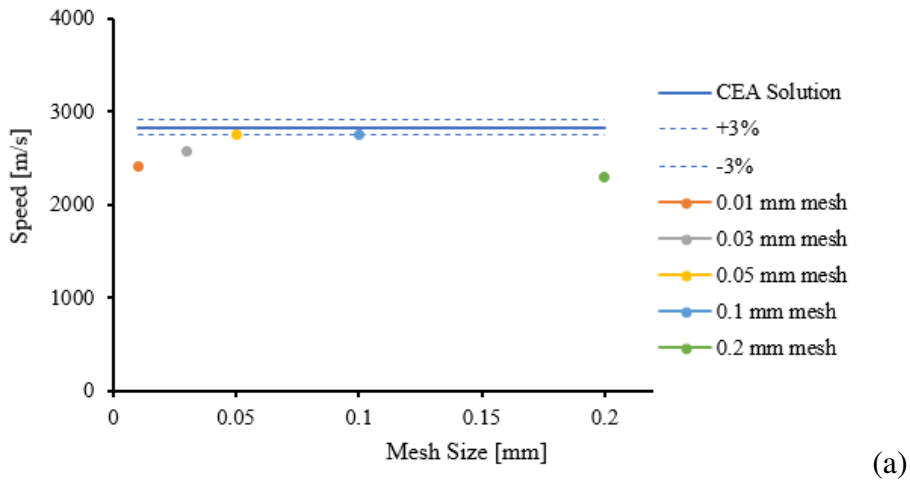Table 3-4 Mesh sensitivity analysis simulation vs CEA value

(a)

(b)

Figure 3-13 Detonation tube mesh sensitivity analysis plots
(a). Detonation Speed, (b). Detonation Temperature
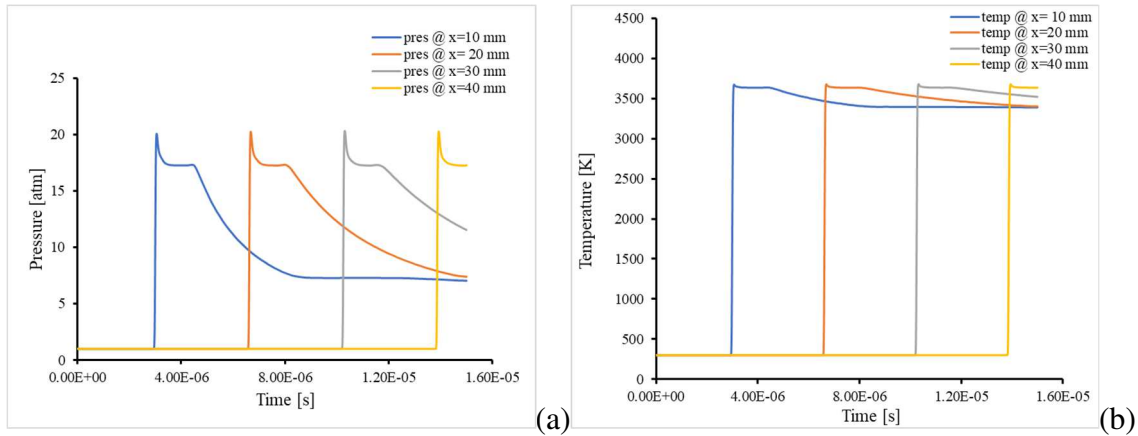
Figure 3-14 Snapshots of detonation wave propagation in tube with 0.1 mm mesh
(a) Pressure, (b) Temperature

3.2.3 Detonation Propagation Simulation in Flame Arrestor Test Setup.

The numerical validation described above confirms the capability of the detonation propagation numerical simulation method in the flame arrestor test setup configuration. The test setup configuration is based on the standards (ISO_16852 2nd Edition [11]) used to validate the detonation flame arrestor product in applications. The test setup configuration is presented in Figure 3-15 [11]
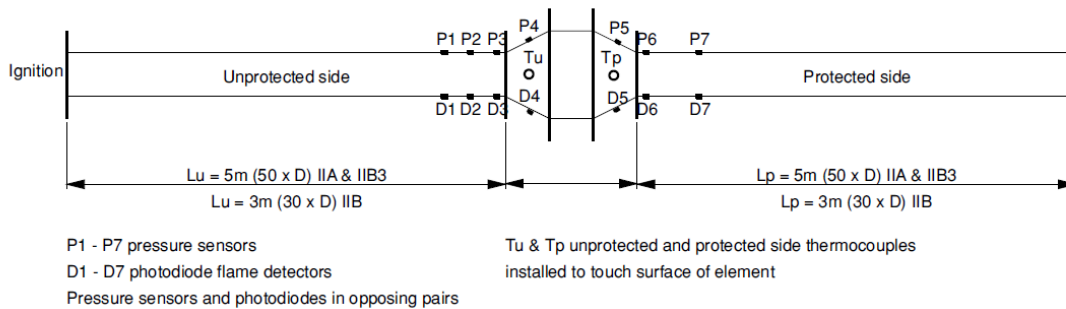
Figure 3-15 Test setup for detonation flame arrestors per IS0-16852 standard

51

The flame arrestor test setup configuration is scaled-down to five percent for the detonation propagation simulation. The simulation domain is shown in Figures 3-16.
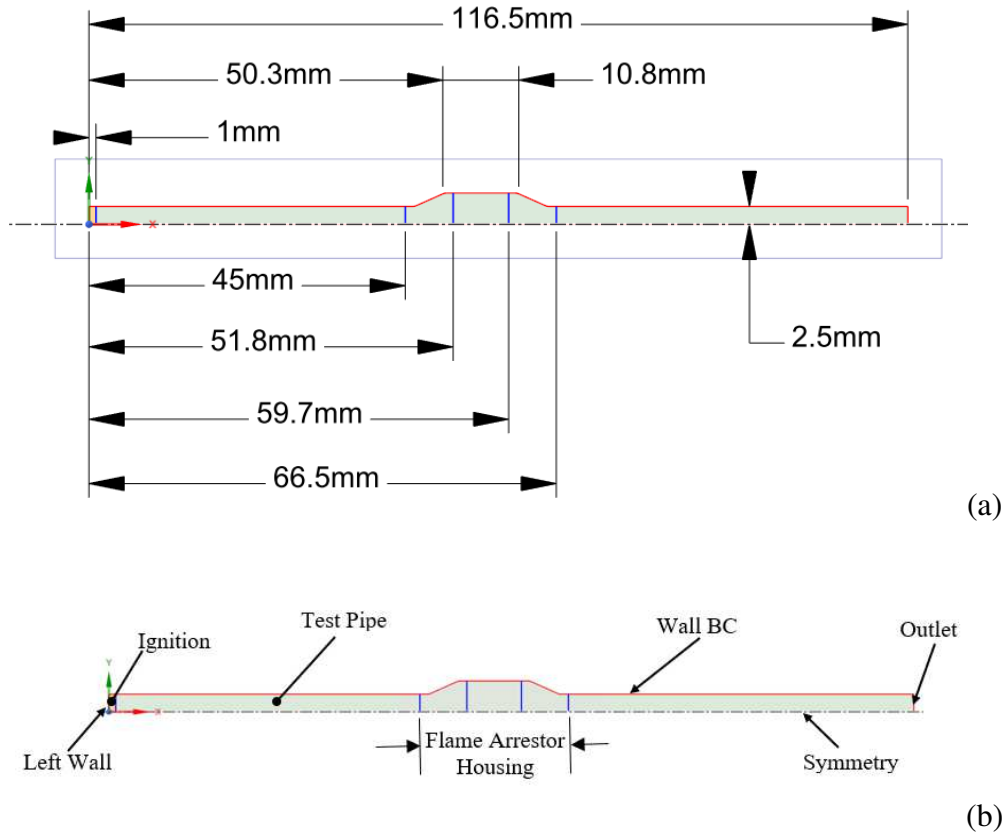

(a)

(b)

figure 3-16 Simulation domain for the test setup
(a) Drawing, (b) Schematic

The inlet pipe, the flame arrestor housing only (excluding the arrestor flame element) and the outlet pipe are used to create the fluid domain for this simulation. The flow domain initial condition and boundary conditions are setup the same as the detonation tube setting. Quadrilateral mesh elements of 0.1 mm are used to discretize the computational domain, which generated 30,623 elements with 31,786 nodes. The solver is setup the same as the detonation tube simulation setup. The flux vectors are computed using Advection Upstream Splitting Method (AUSM) scheme and the convective term is computed using second order upwind

scheme. The transient solution is obtained with an explicit time- stepping regime using 4th-order Runge-Kutta scheme for unsteady flow. Details of the ANSYS® Fluent™ solver setting are presented in Appendix B, Table B-1.

3.2.4 Inviscid Model Simulation Result and Discussion

The test setup simulation domain is divided into five regions, inlet pipe, inlet flange, element housing, outlet flange and outlet pipe. The numerical simulation result is presented and reviewed for each region.

The inlet pipe detonation propagation characteristic is presented in Figures 3-17 and 3-18. The result is the same as the detonation tube analysis as expected.

(a)   (b)
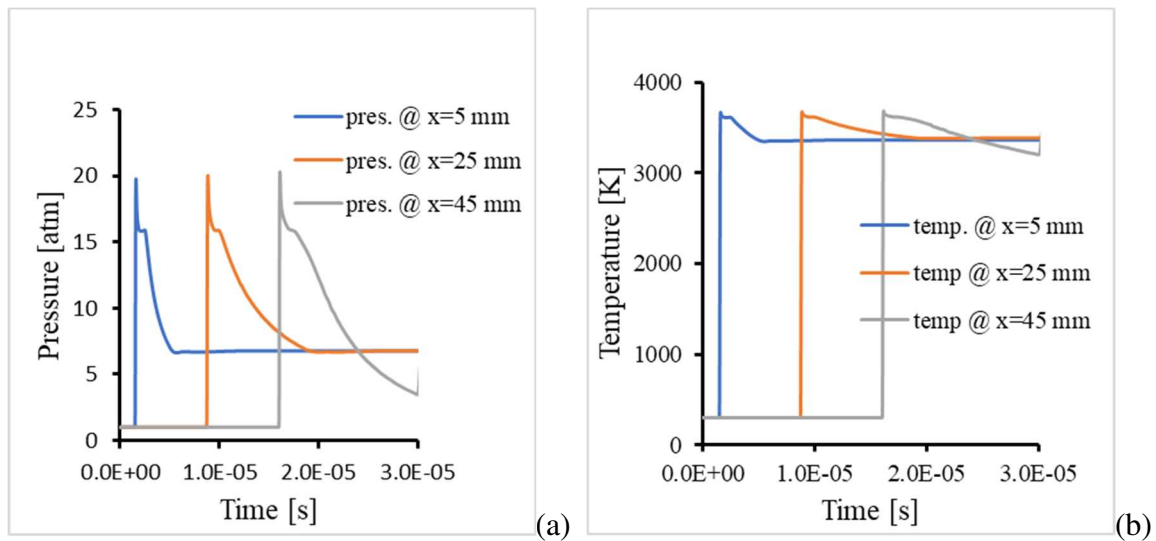
Figure 3-17 Inlet pipe detonation propagation with the inviscid solver
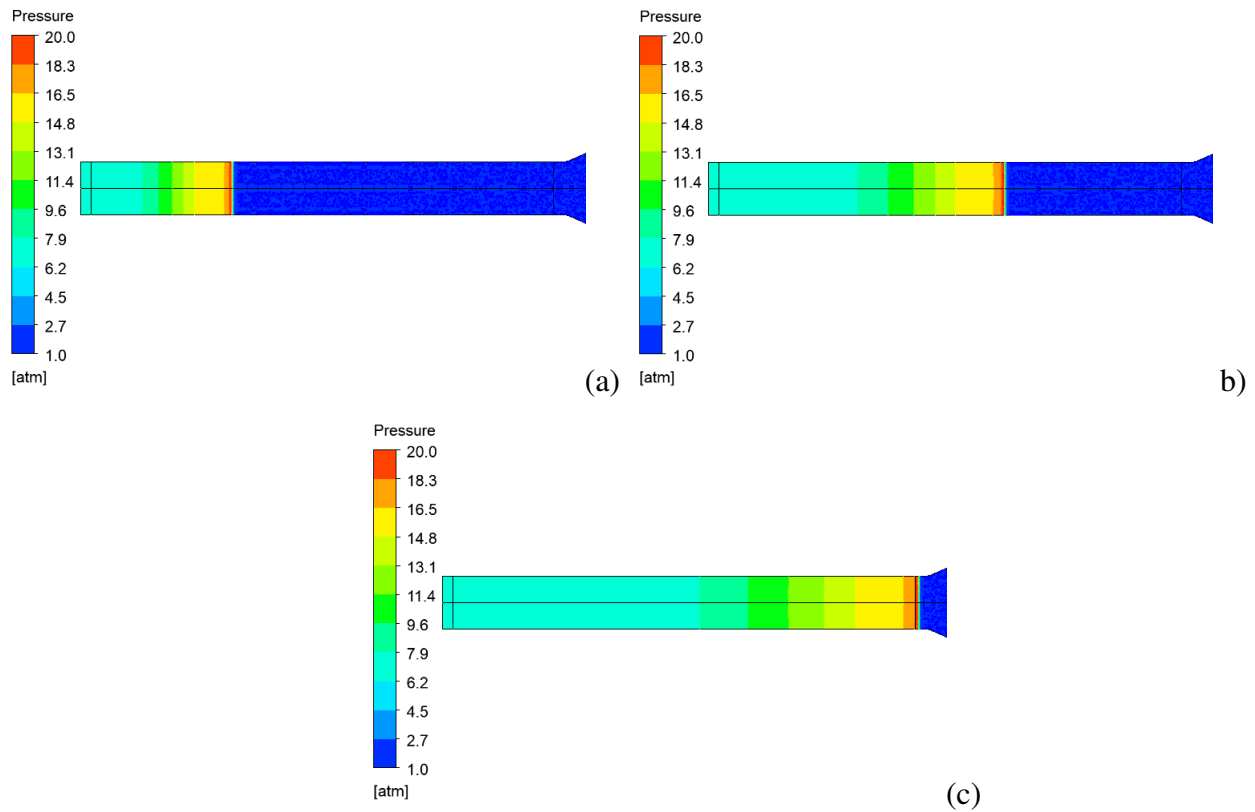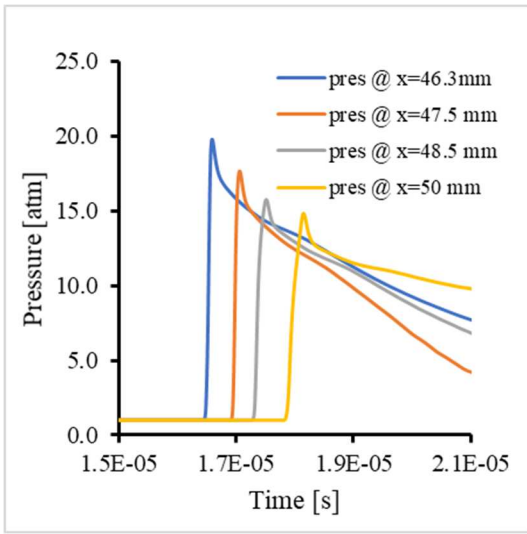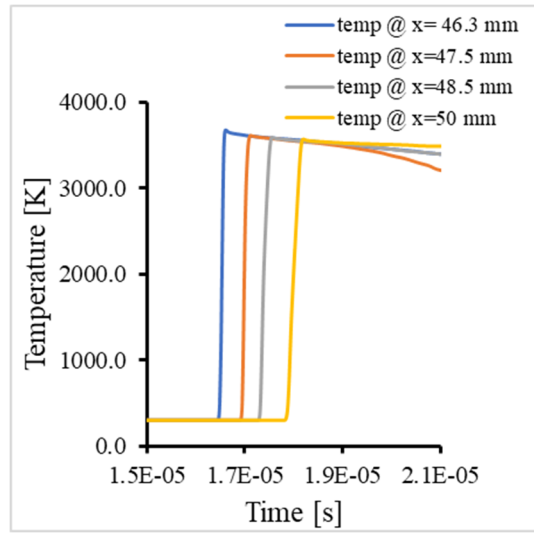(a) Pressure time (b). Temperature time

Figure 3-18 Inlet pipe detonation propagation with the inviscid solver
(a). 5μs, (b). 10μs, (c). 16.2μs

The inlet flange simulation results are shown in Figures 3-19 and 3-20. Since the flow is supersonic and the flange area is increasing the detonation pressure reduces significantly and veloity increases. From the contour plot, it can be observed that the Mach waves reflecting from the flange walls and travelling towards the center of the pipe [6]. These Mach waves reflected from the wall reaches the incoming propagating detonation wave, and the propagating detonation wave develops a bow shape as it travels into the inlet flange.
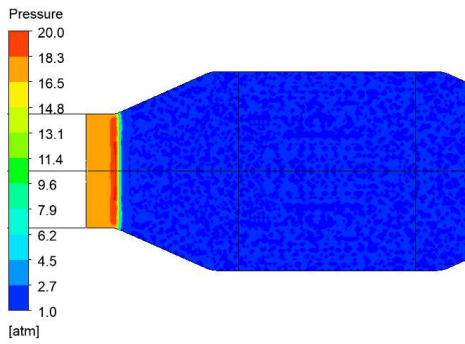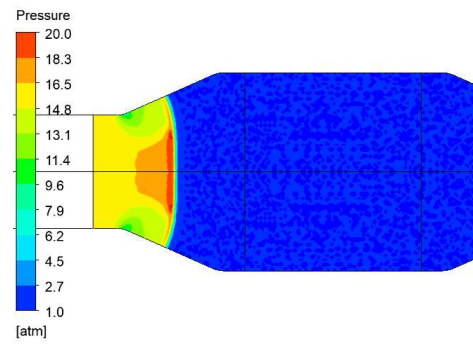
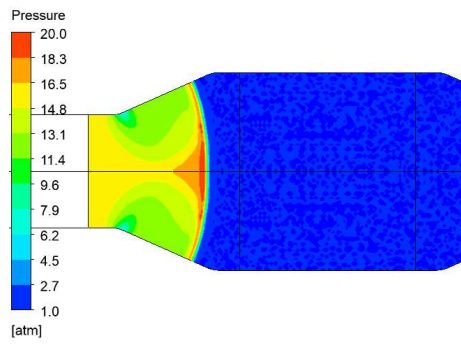Figure 3-19 Inlet flange detonation propagation with inviscid solver
(a) Pressure time (b). Temperature time

Figure 3-20 Inlet flange detonation propagation contour with inviscid solver
(a) 16.6μs, (b). 17.4μs, (c). 18μs, (d).18.6μs

In the flame element housing section, the detonation propagation eventually becomes stable. The detonation propagation simulation results are shown in Figures 3-21 and 3-22

(a)   (b)

Figure 3-21 Housing detonation propagation using the inviscid solver
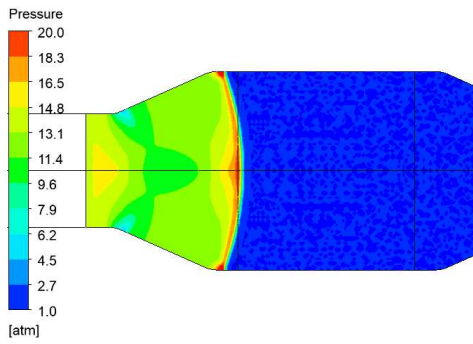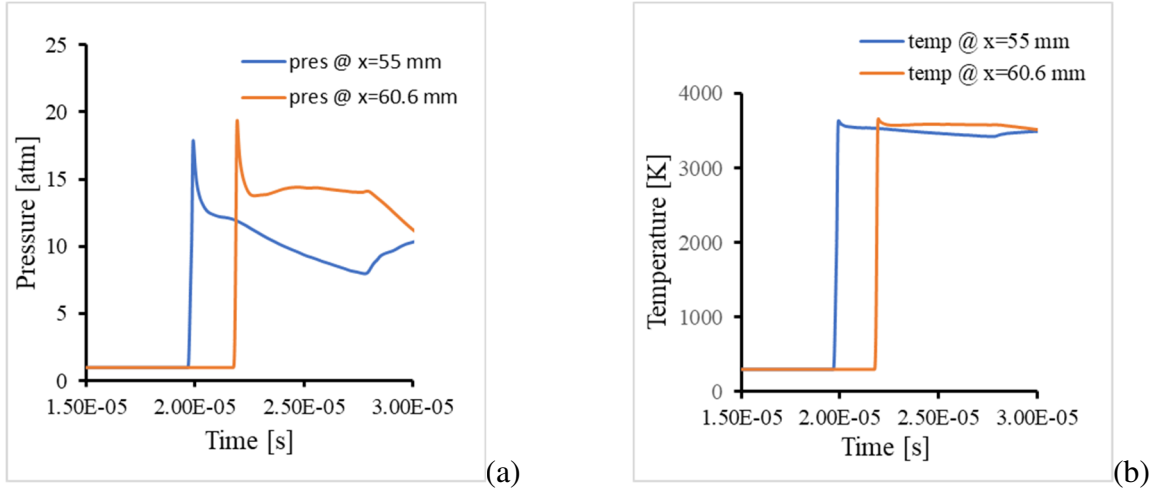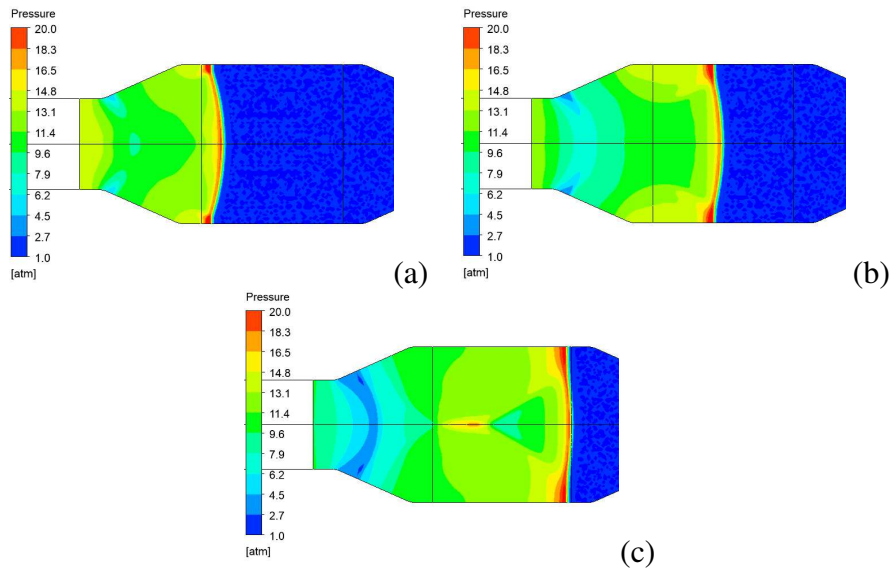(a). Pressure time (b). Temperature time

(a)   (b)

(c)

Figure 3-22 Housing detonation propagation contours using inviscid solver
(a) 19μs, (b). 20μs, (c). 21.5μs

The outlet flange detonation propagation characteristics is the most interesting. Since the flow is supersonic, the reduction in area causes the pressure to increase. The reflected shock waves from the wall collides with the incoming propagating wave generating extremely high pressure focused in the center. The detonation pressure increases to much higher value (60 to 70 atm) compared to the CJ detonation pressure (~20 atm) which puts it in the overdriven detonation category. In the pressure contour plots high-pressure points are observed.
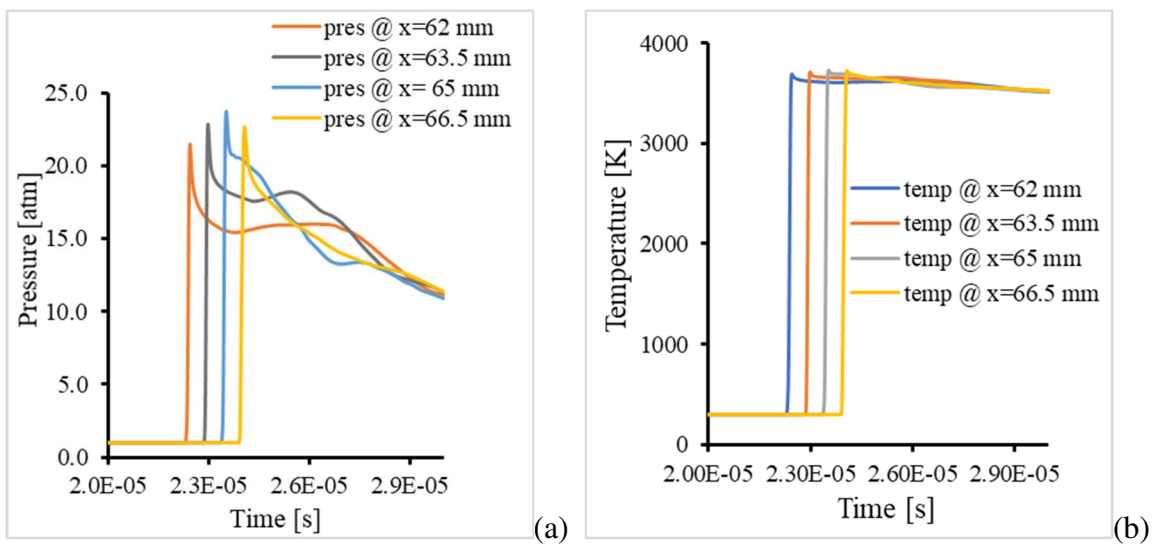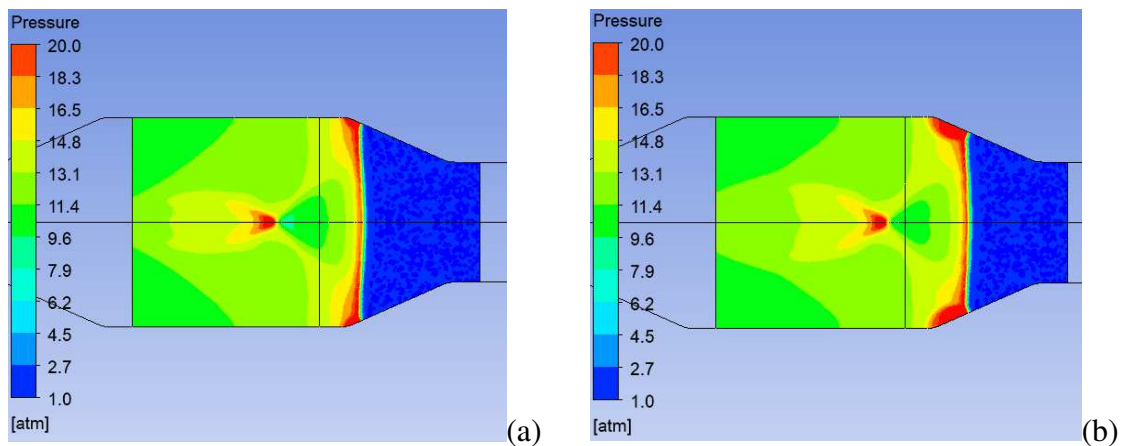

(a)   (b)

Figure 3-23 Outlet flange detonation propagation using the inviscid model
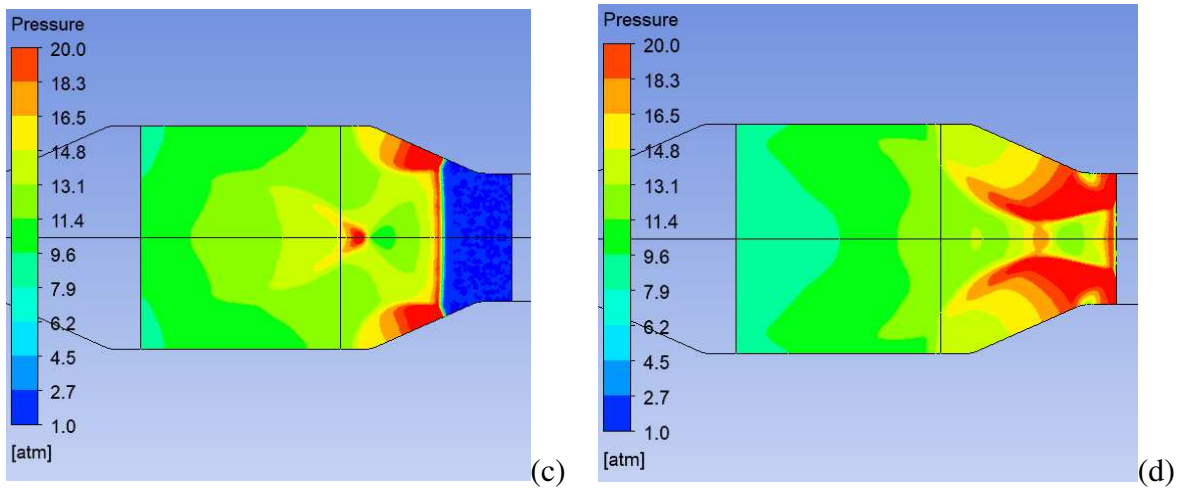(a). Pressure time (b). Temperature time

(a)   (b)

(c)

(d)

Figure 3-24 Outlet flange detonation propagation contours using the inviscid model
(a) 22µs, (b)22.5µs (c)23 µs (d) 24µs

The outlet pipe detonation characteristics are presented in Figures 3-25 and 3-26. At the entrance
to the outlet pipe, the detonation pressure is higher than the Chapman–Jouguet stable detonation
pressure. However, eventually the reacting gas will catchup with the detonation wave and slows it
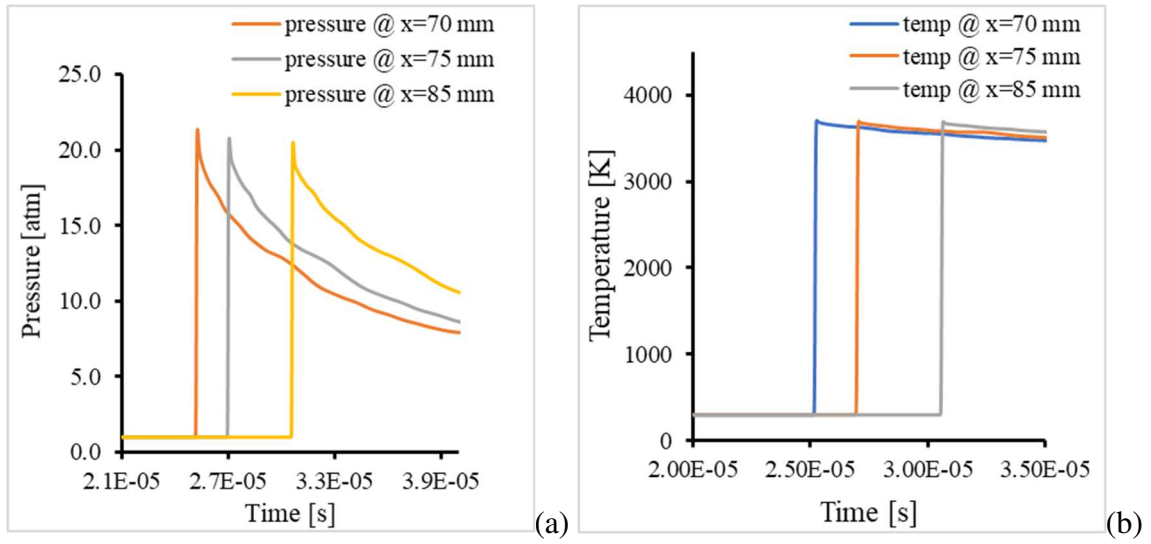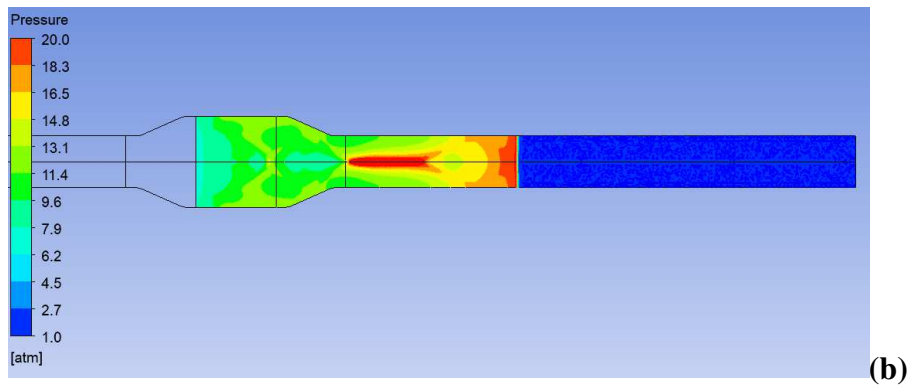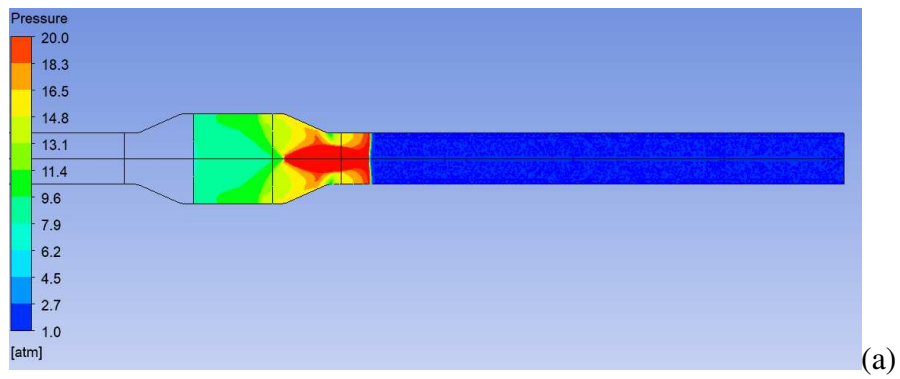down until it achieves the Chapman–Jouguet condition.

Figure 3-25 Outlet pipe detonation propagation using the inviscid model
(a). Pressure time (b). Temperature time

(a)

(b)

59
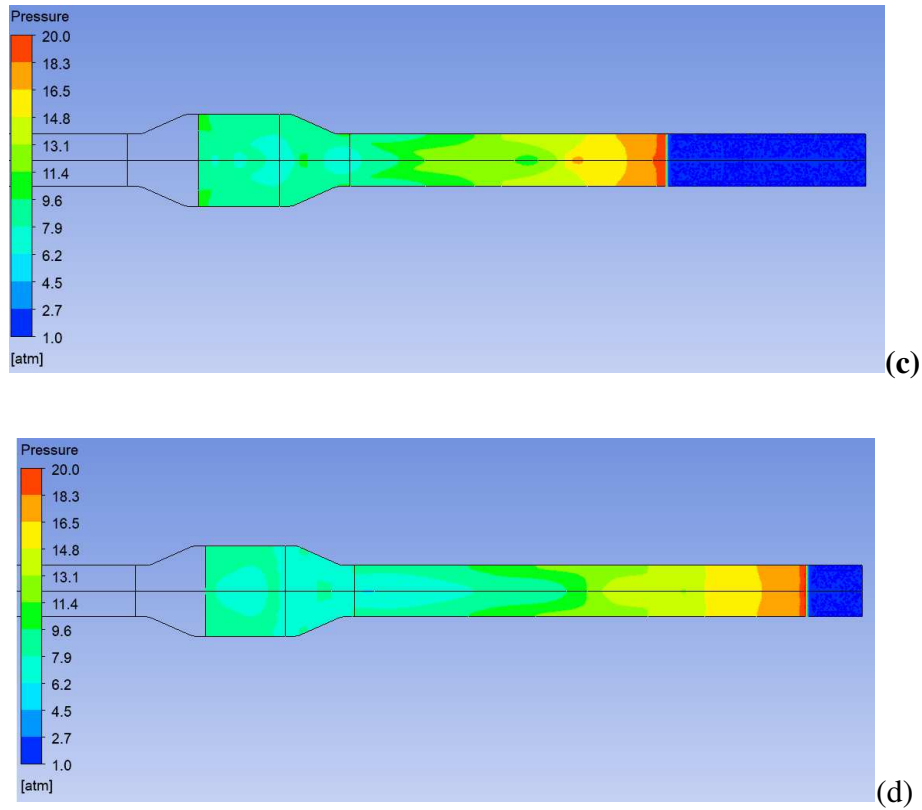
Figure 3-26 Outlet pipe detonation propagation contours using the inviscid model
(a) 25µs, (b) 30µs (c) 35 µs (d) 40µs

In summary the inviscid simulation of detonation propagation in a flame arrestor test setup configuration is feasible. The simulation results in the inlet and outlet pipes matches the detonation tube simulation result. The behavior of the detonation propagation in the inlet and outlet flange agree with CJ theory [8].

3.2.5 Turbulent Adiabatic Model Numerical Simulation Result and Discussion

The computational domain and the boundary conditions used for the viscous adiabatic model are the same as the inviscid model. In the viscous model, the axisymmetric reactive Navier-Stokes equations are used. The flow is setup as turbulent flow where the turbulent viscosity is

modeled using the Shear Stress Transport k-ω two-equation model. The ANSYS® Fluent™ solver settings used in the simulation are given in Appendix B, Table B-2.

As in the inviscid simulation the flow domain is divided into five regions and the result and review is presented.

(a)   (b)

Figure 3-27 Inlet pipe detonation propagation using a turbulent adiabatic model
(a). Pressure Time (b). Temperature Time

(a)   (b)

(c)

(d)

Figure 3-28 Inlet pipe detonation propagation contours using a turbulent adiabatic model
a) 5µs, b)15µs c) 20µs d) 21µs

(a)

(b)
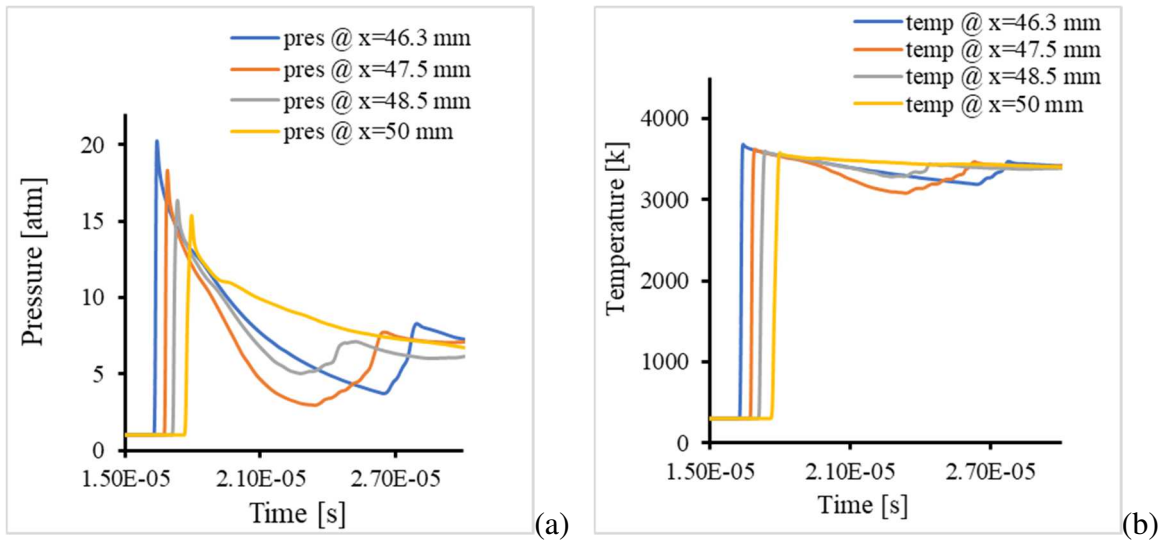
Figure 3-29 Inlet flange detonation propagation using a turbulent adiabatic model
(a). Pressure time (b). Temperature time

(a)   (b)   (c)
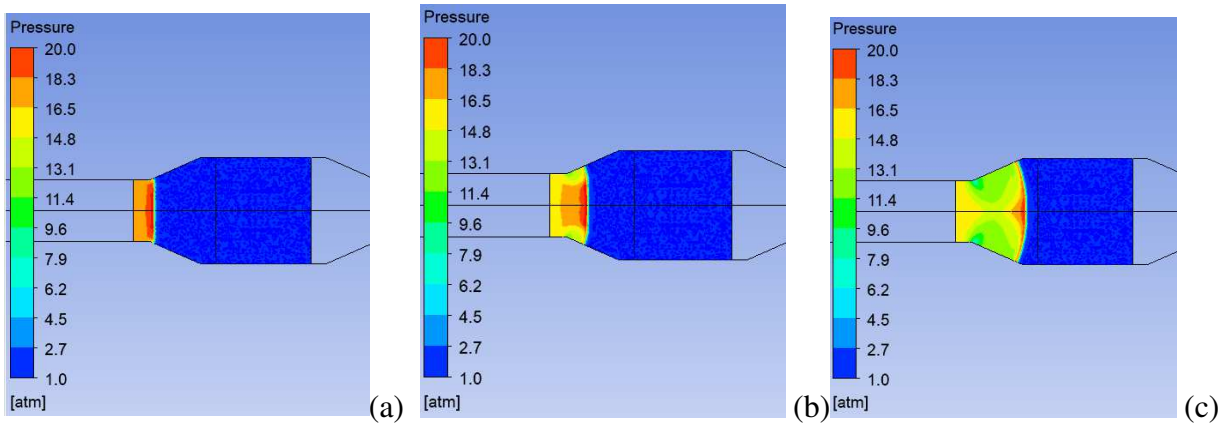
Figure 3-30 Inlet flange detonation propagation contours using a turbulent adiabatic model
(a). 16.5μs, (b). 17μs (c). 18μs

(a)   (b)
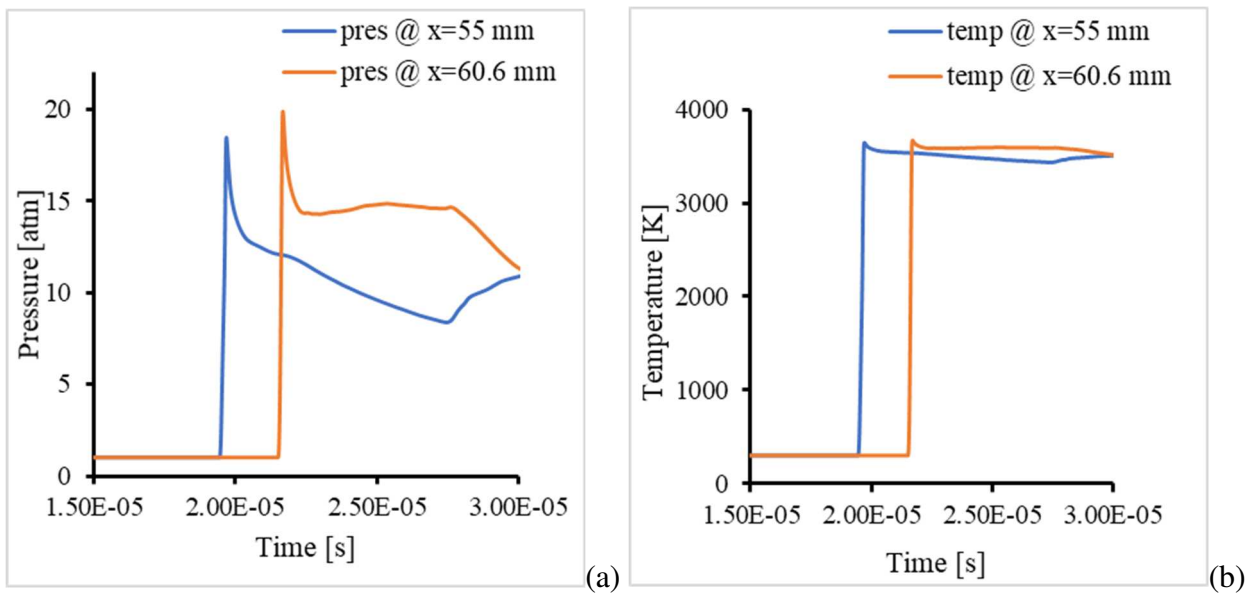
Figure 3-31 Housing detonation propagation using a turbulent adiabatic model
(a). Pressure time (b). Temperature time
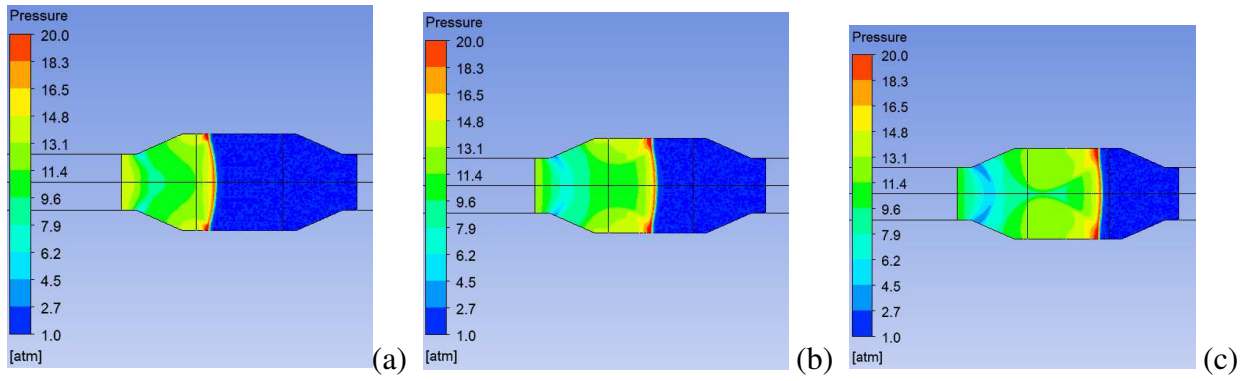
Figure 3-32 Housing detonation propagation contours using a turbulent adiabatic Contour
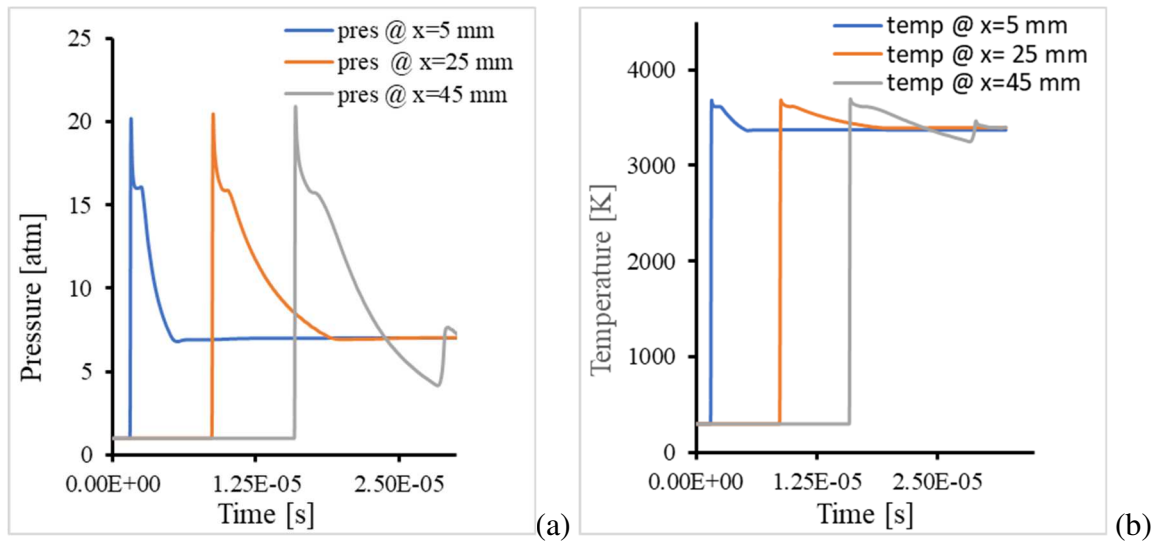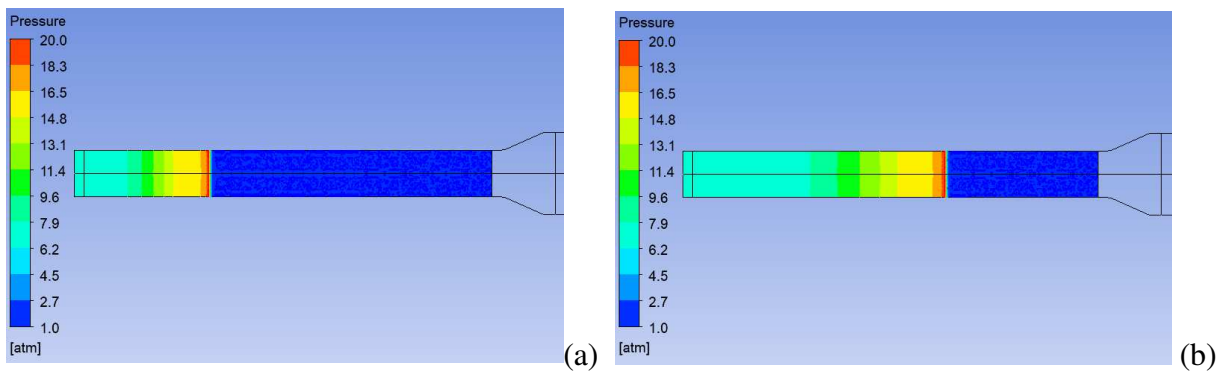(a). 19μs, (b). 20μs (c). 21μs

Figure 3-33 Outlet flange detonation propagation using a turbulent adiabatic model
(a). Pressure time (b). Temperature time

Figure 3-34 Outlet flange detonation propagation contours using a turbulent adiabatic model
(a). 22μs, (b). 22.5μs (c). 23μs (d). 23.5μs, (e). 24μs (f). 24.5μs
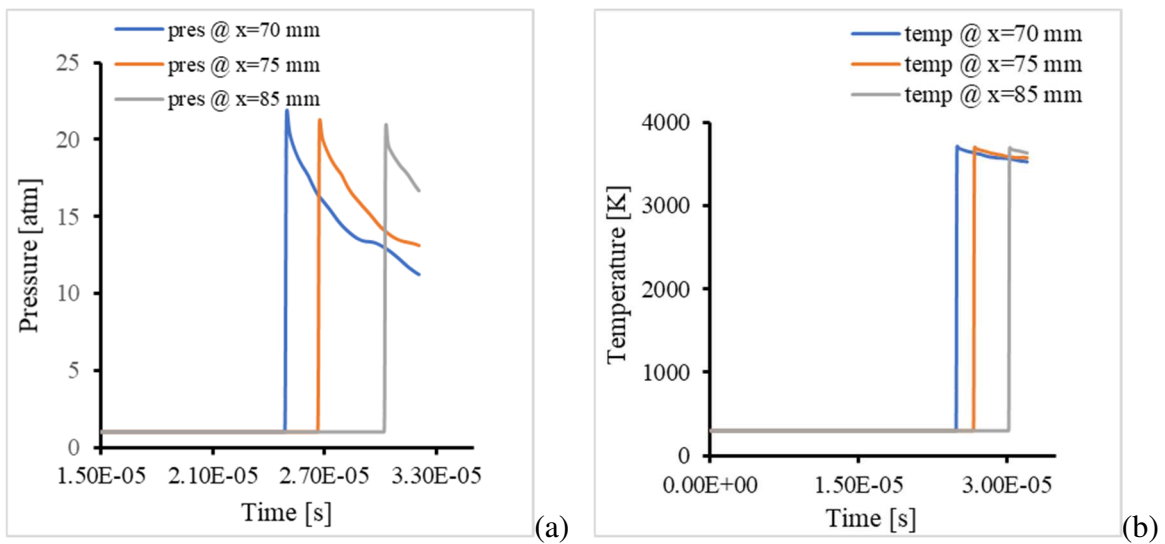
Figure 3-35 Outlet pipe detonation propagation using a turbulent adiabatic model
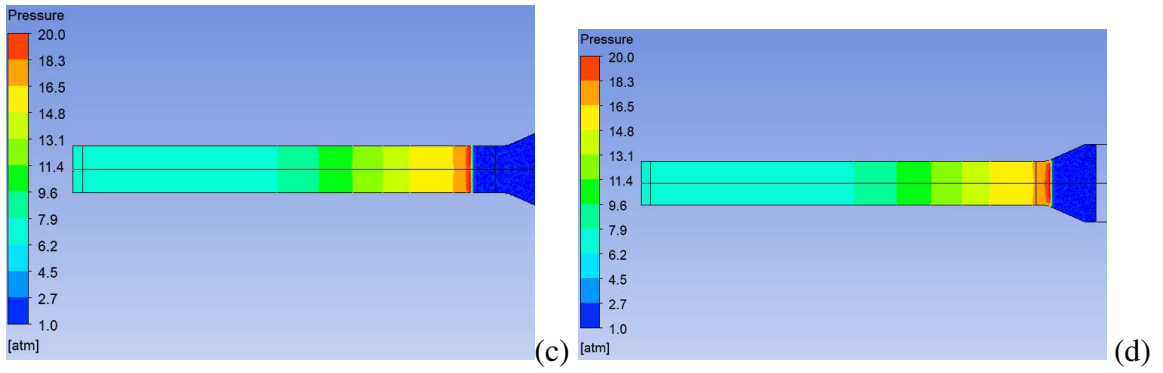(a). Pressure time (b). Temperature time

(a)

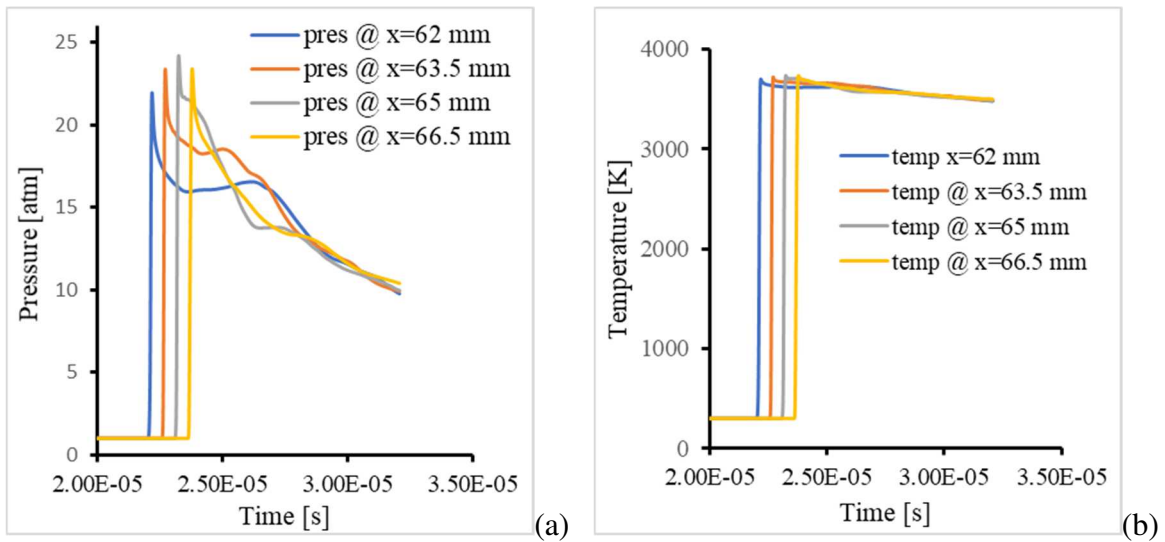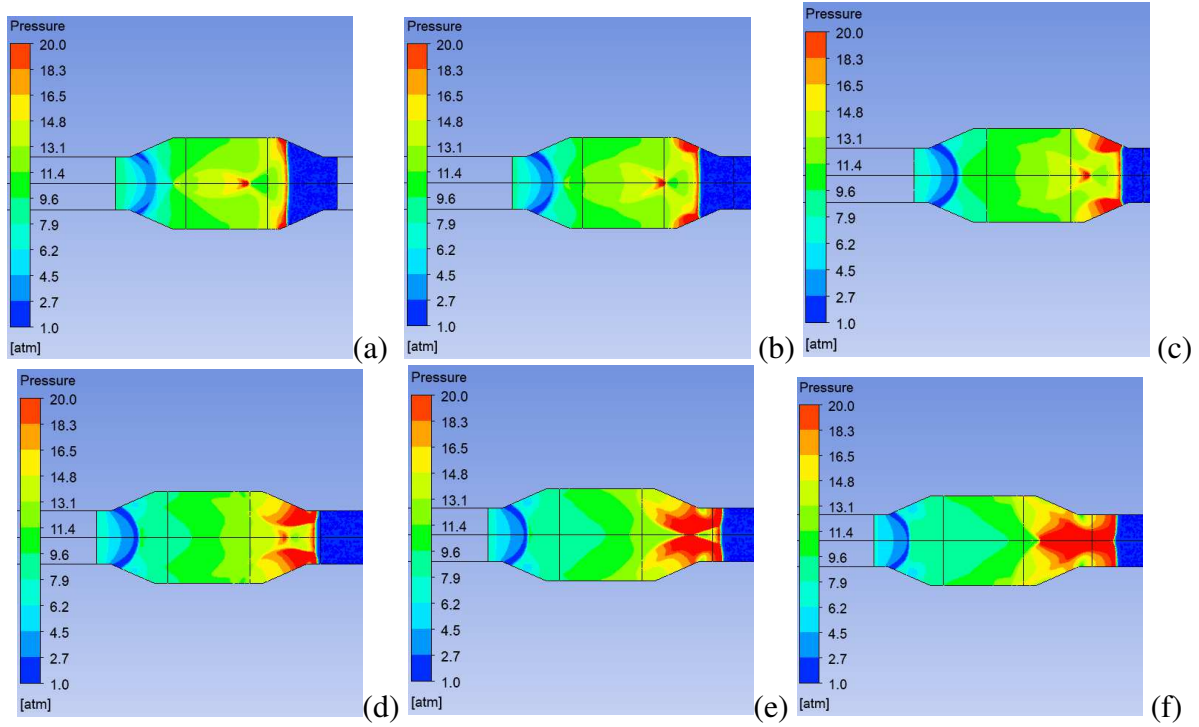

(b)

(c)

(d)
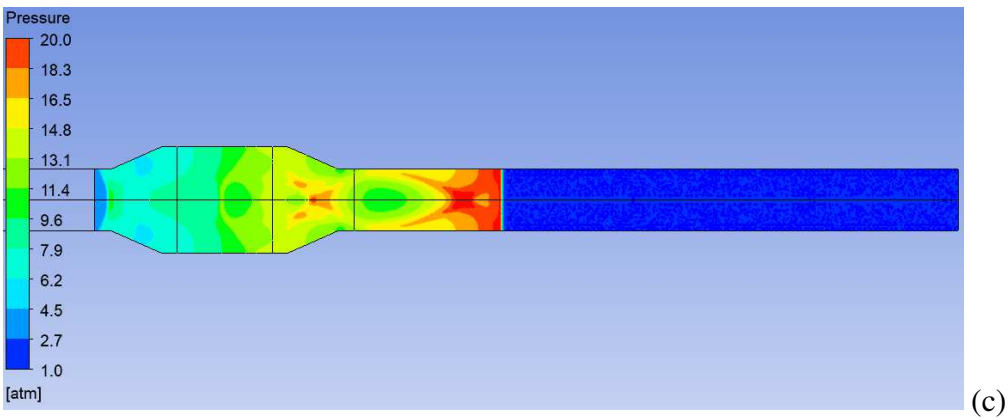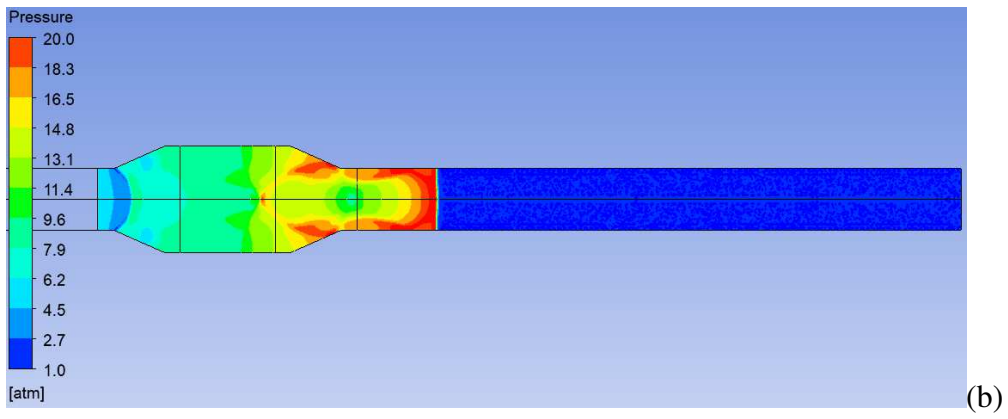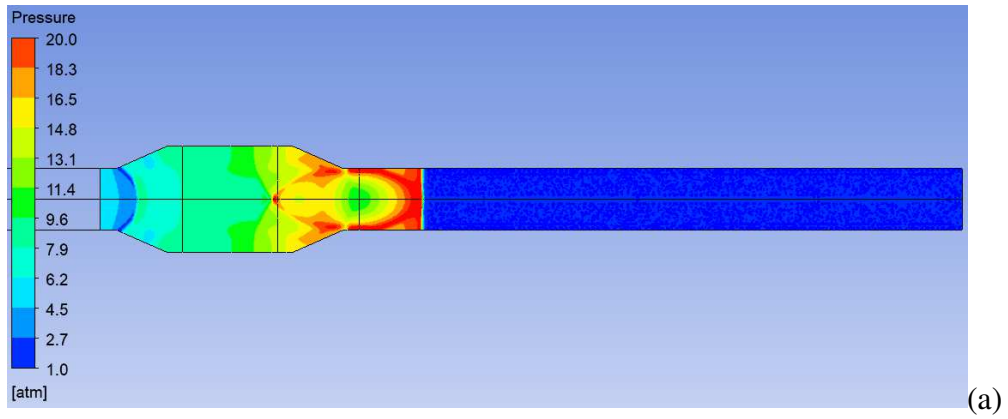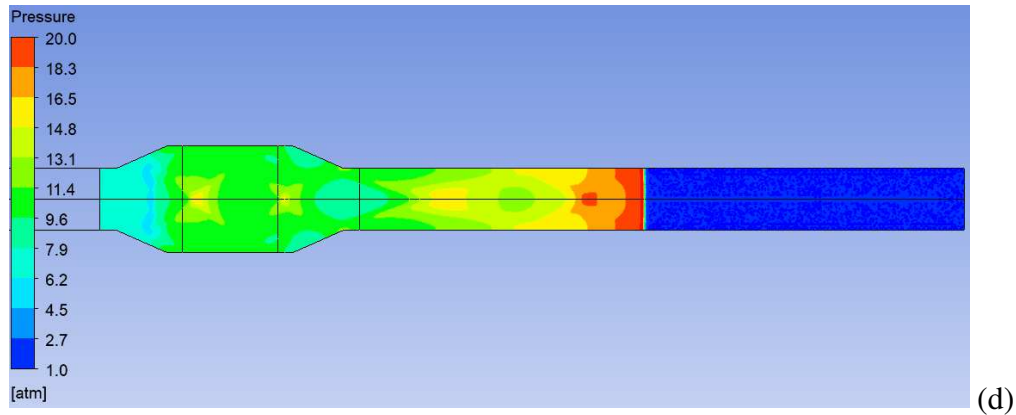
Figure 3-36 Outlet pipe detonation propagation contours using a turbulent adiabatic model
(a). 25μs, (b). 26μs (c). 28μs (d). 32μs

3.2.6 Turbulent with Heat Transfer Model Numerical Simulation Result and Discussion

The computational domain for the turbulent with heat transfer model is the same as the

turbulent adiabatic model. An isothermal wall boundary condition is used for the turbulent heat

transfer model. A constant heat transfer coefficient is prescribed for this simulation. In the

turbulent model, the axisymmetric reactive Navier-Stokes equations are used. The turbulent

viscosity is modeled using the Shear Stress Transport k-ω two-equation model. The solver setting

used is the same as the turbulent adiabatic model. The only difference from the turbulent adiabatic

model is the wall boundary conditions. A mixed wall boundary condition is used where the heat

transfer coefficient is set to 10 w/m^{2}K, the freestream temperature is 300 K, the external emissivity

is unity, the external radiation temperature is 300 K, the wall thickness 0.00038 m for element

housing and flanges, and 0.0003 m for inlet and outlet pipes. Detail simulation setup and boundary

condition setup is shown in Appendix B. Table B-3.

As in the previous cases the simulation flow domain is divided into five regions. The numerical

simulation results and reviews are presented below. The simulation result appears similar to the

67

turbulent adiabatic simulation results. The heat transfer characteristics of the boundary wall has a

minimum effect on the detonation propagation.
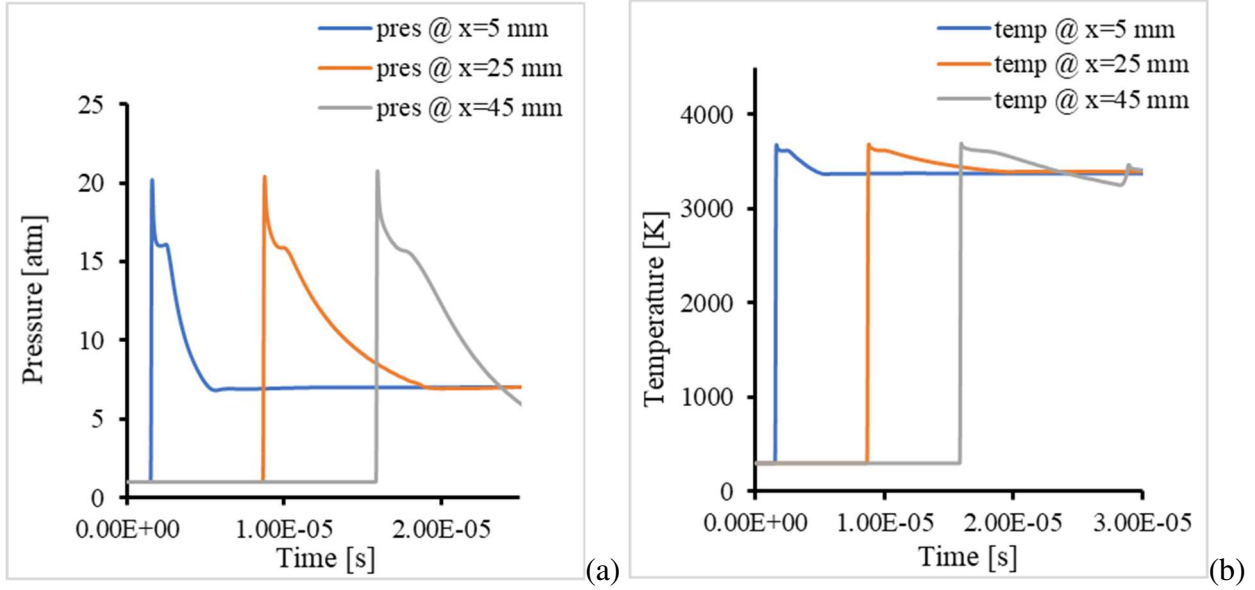
Figure 3-37 Inlet pipe detonation propagation with turbulent heat transfer model
(a). Pressure time (b). Temperature time
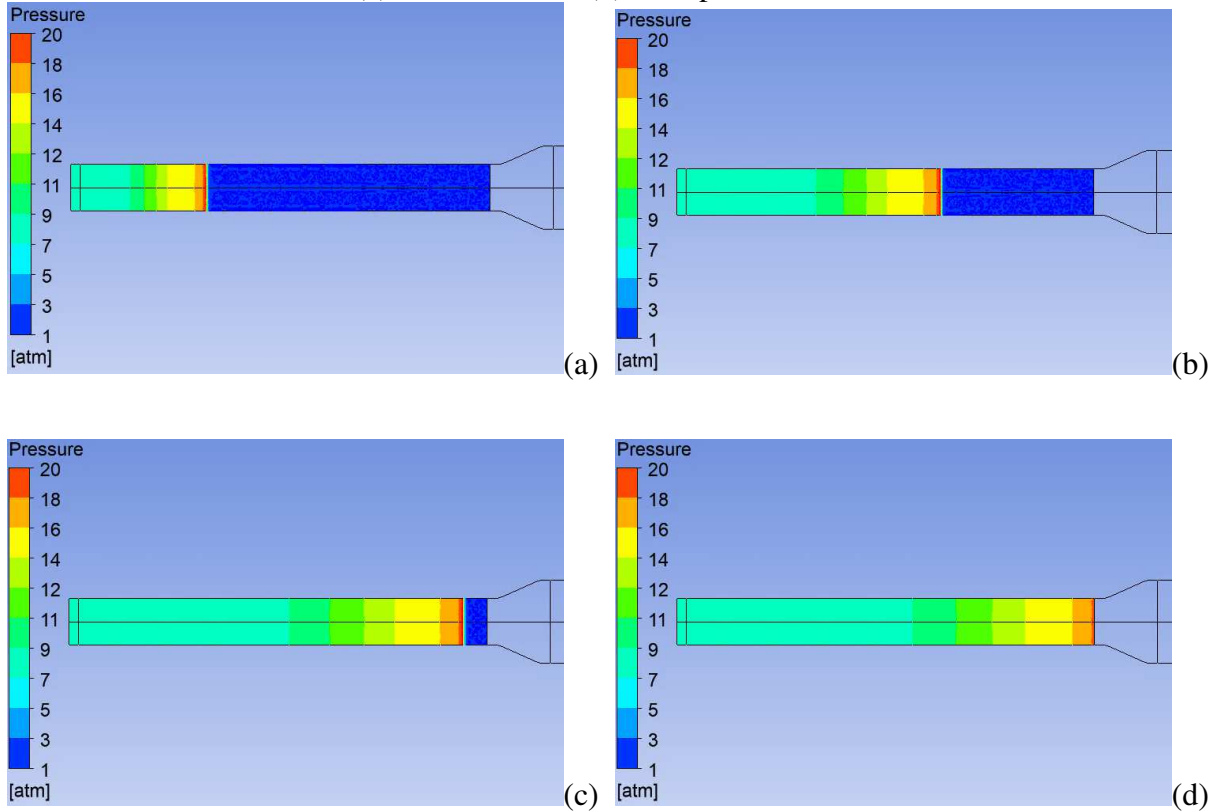
Figure 3-38 Inlet pipe detonation propagation contours with turbulent heat transfer model
(a). 5μs, (b). 10μs, (c). 15μs, (d). 16μs

(a)

(b)
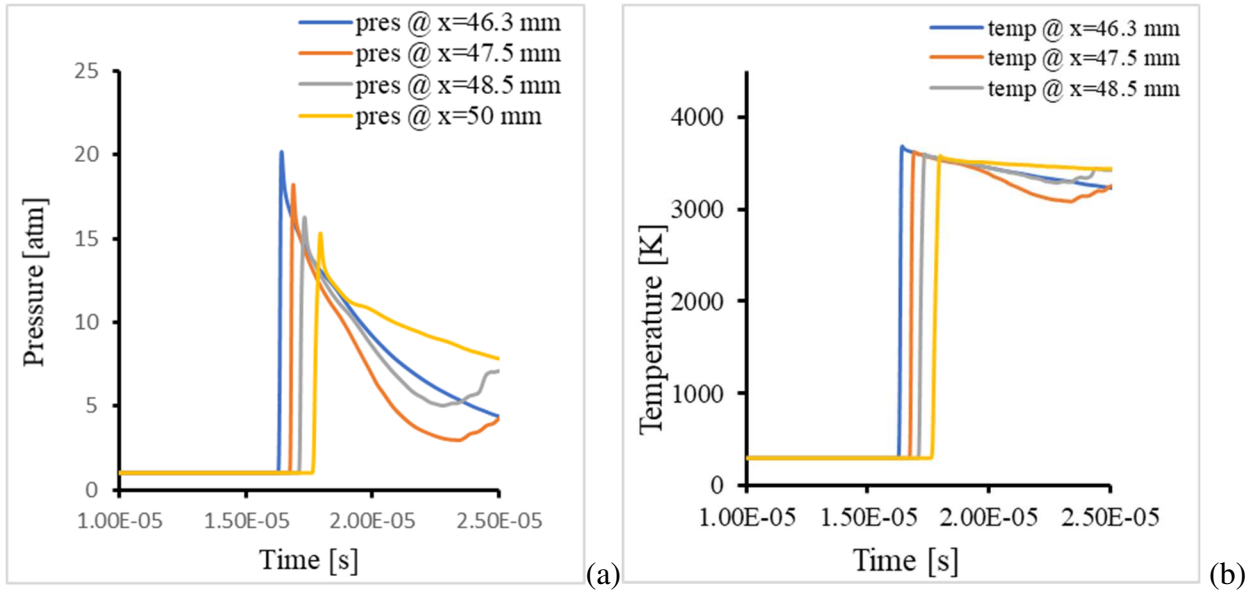
Figure 3-39 Inlet flange detonation propagation with turbulent heat transfer model
(a). Pressure Time Chart, (b). Temperature Time Chart

(a)   (b)   (c)
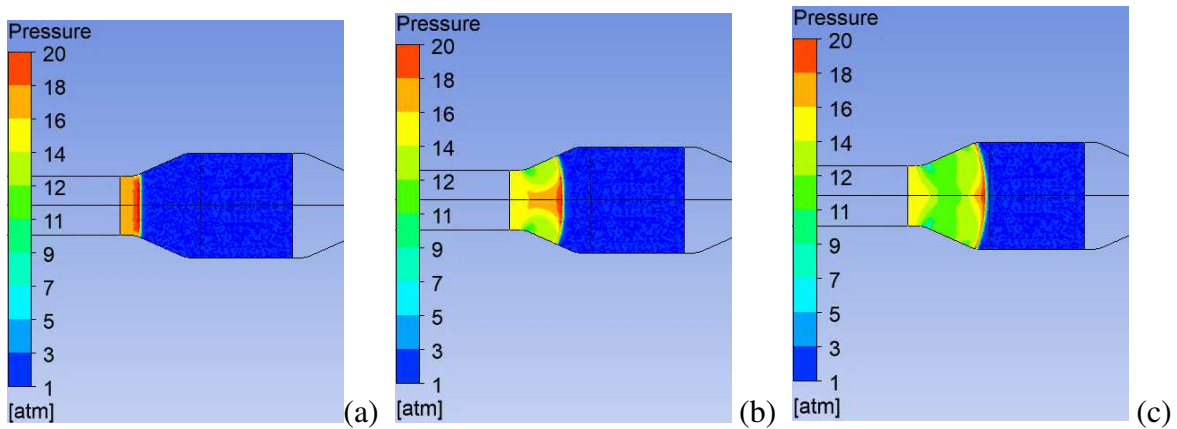
Figure 3-40 Inlet flange detonation propagation contours with turbulent heat transfer model
(a). 16.5μs, (b). 17.5μs, (c). 18.24μs
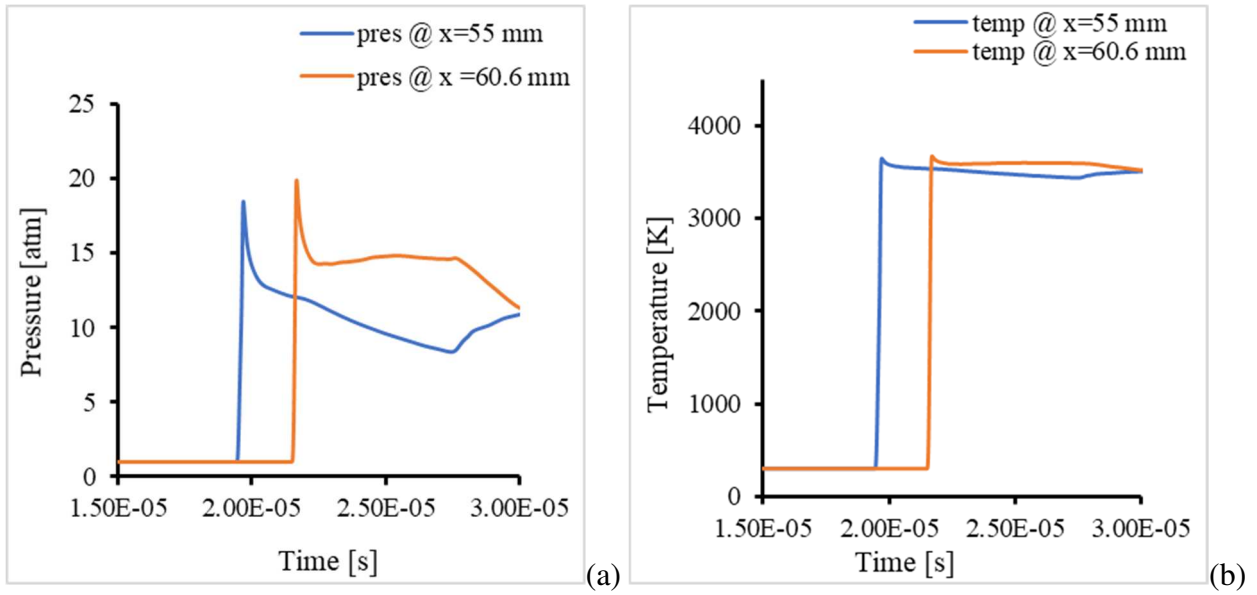
Figure 3-41 Housing detonation propagation with turbulent heat transfer model
(a). Pressure time (b). Temperature time
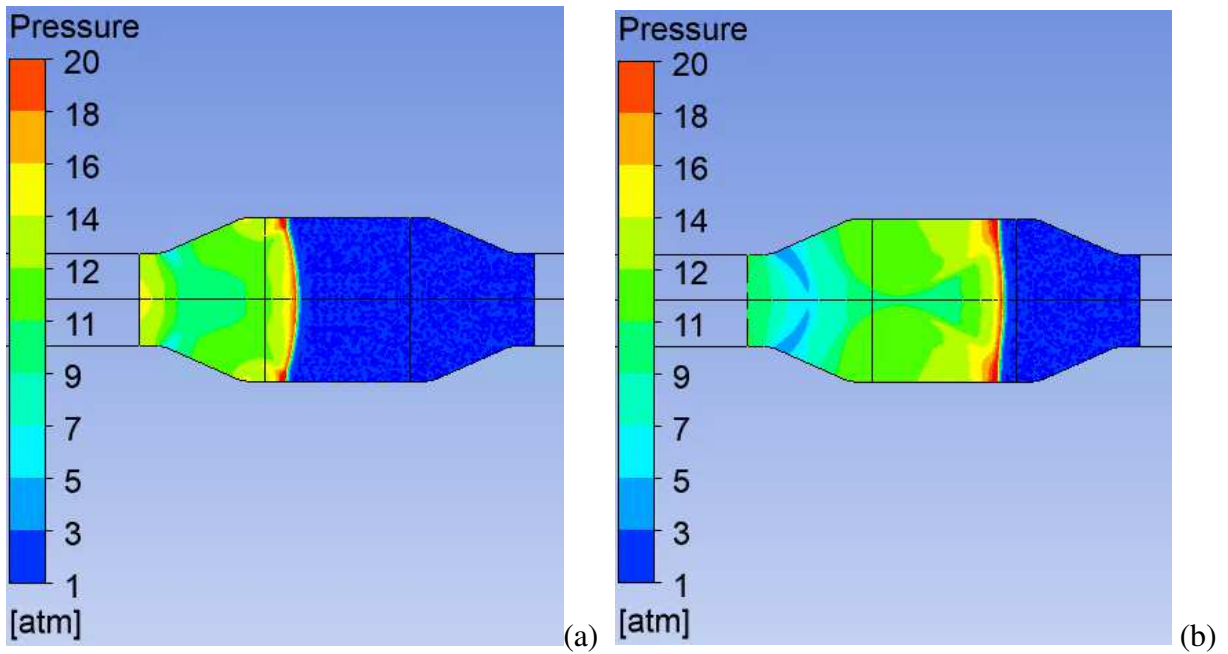
Figure 3-42 Housing detonation propagation contours with turbulent heat transfer model
(a).19μs, (b). 21μs
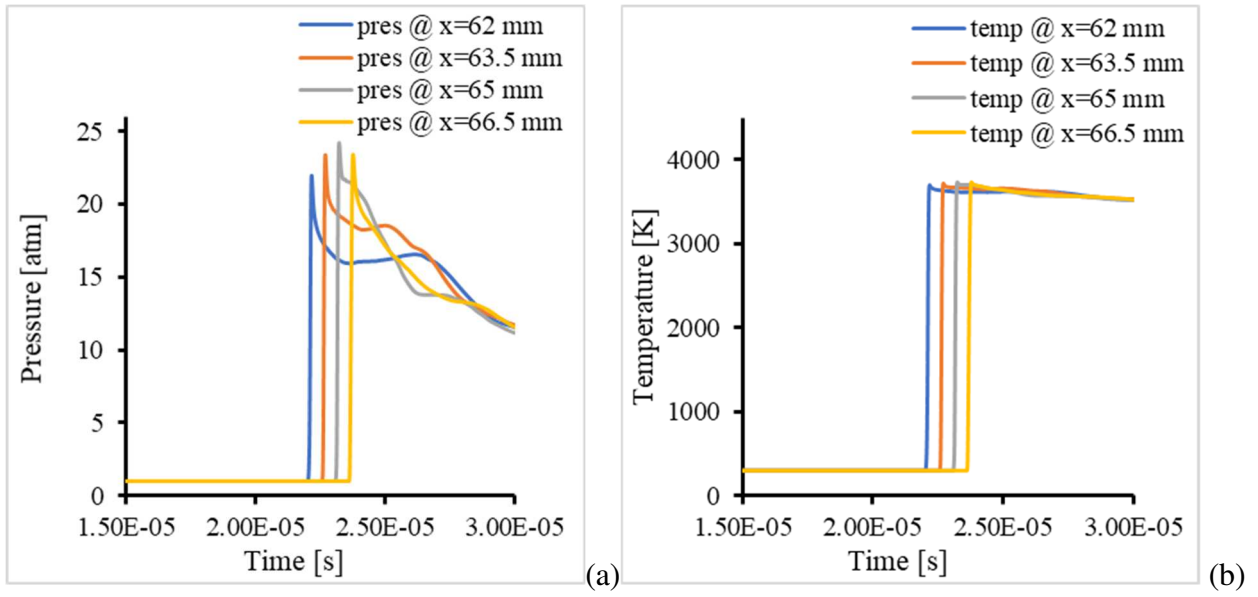
Figure 3-43 Outlet flange detonation propagation with turbulent heat transfer model
(a). Pressure time, (b). Temperature time
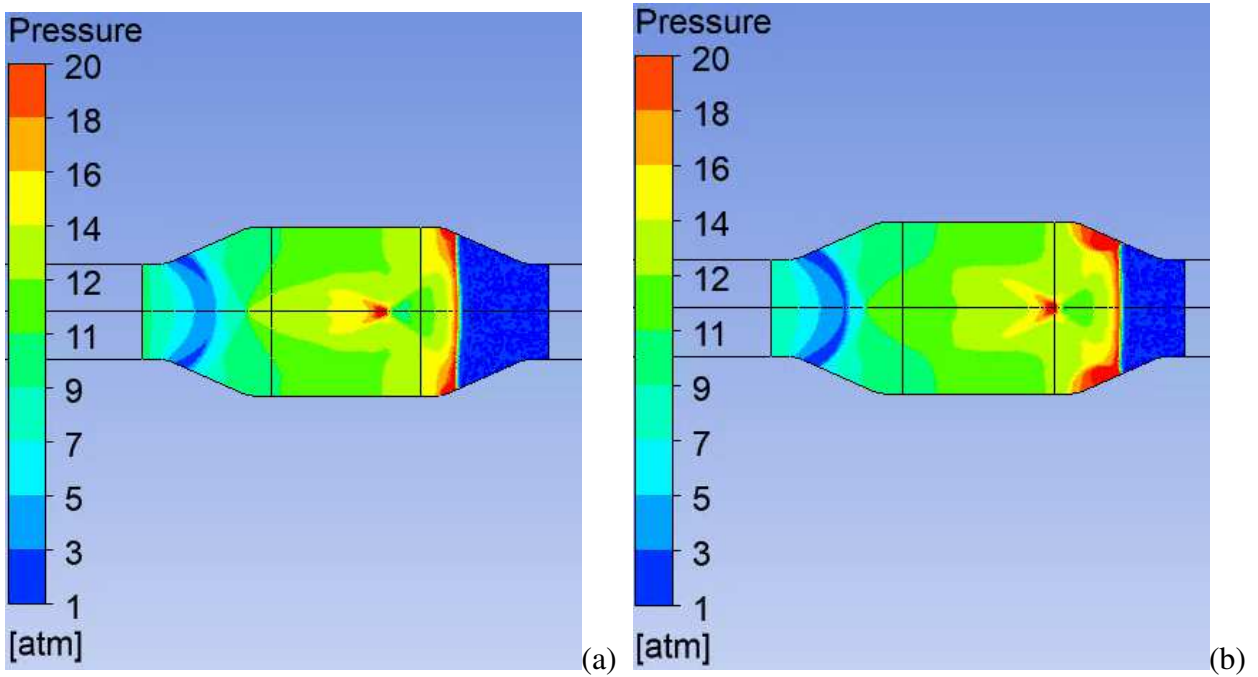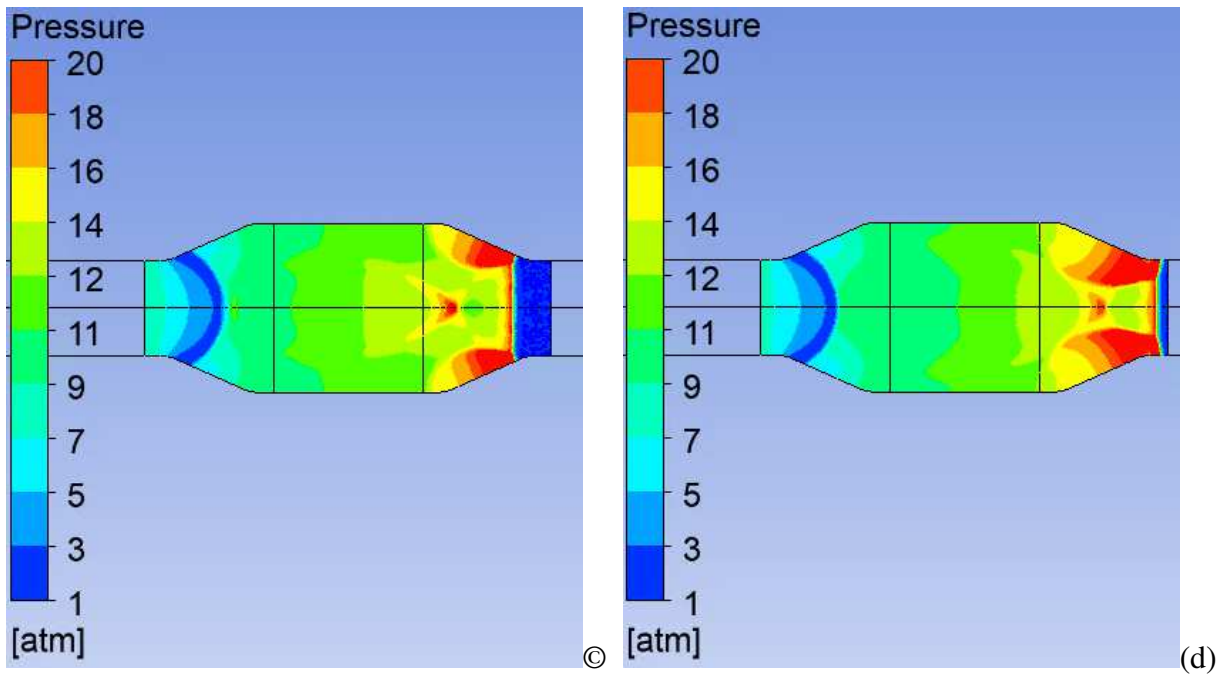
Figure 3-44 Outlet flange detonation propagation contours with turbulent heat transfer
(a). 22μs, (b). 22.5μs, (c). 23μs, (d). 23.5μs
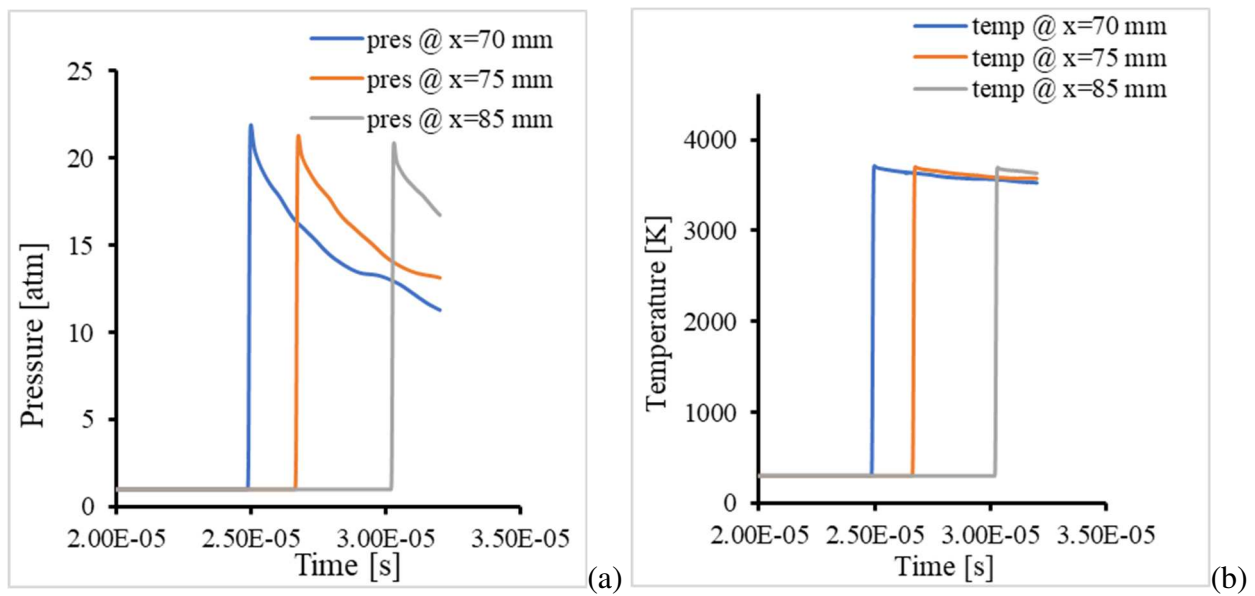
Figure 3-45 Outlet pipe detonation propagation with turbulent heat transfer
(a). Pressure time, (b). Temperature time

(a)

(b)

(c)

(d)

(e)

(f)
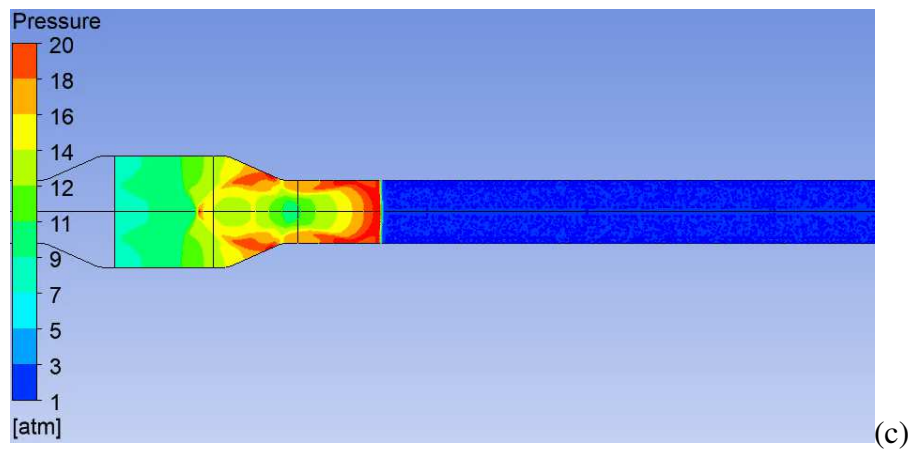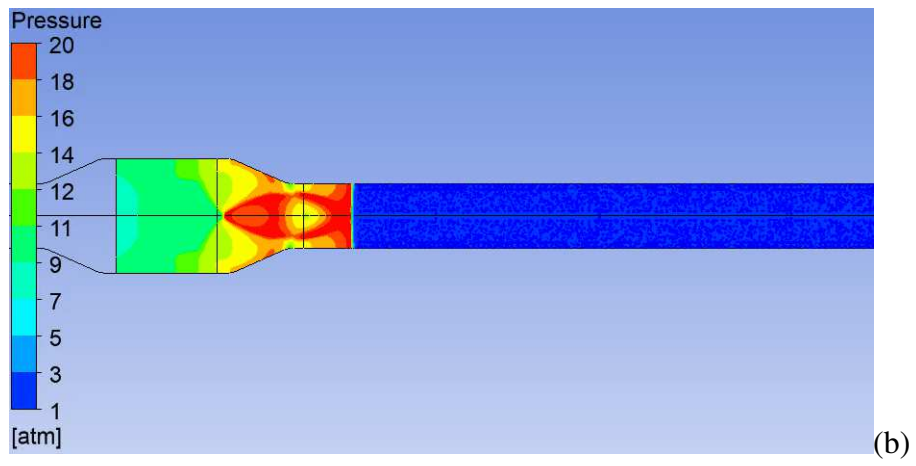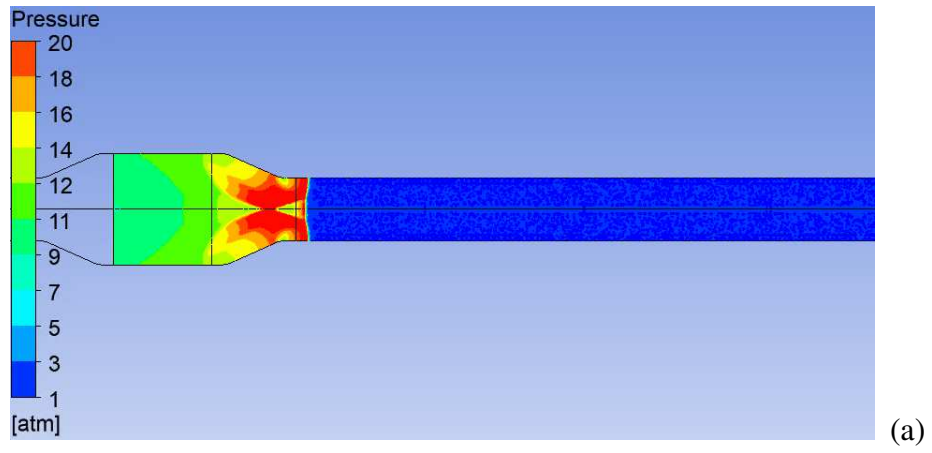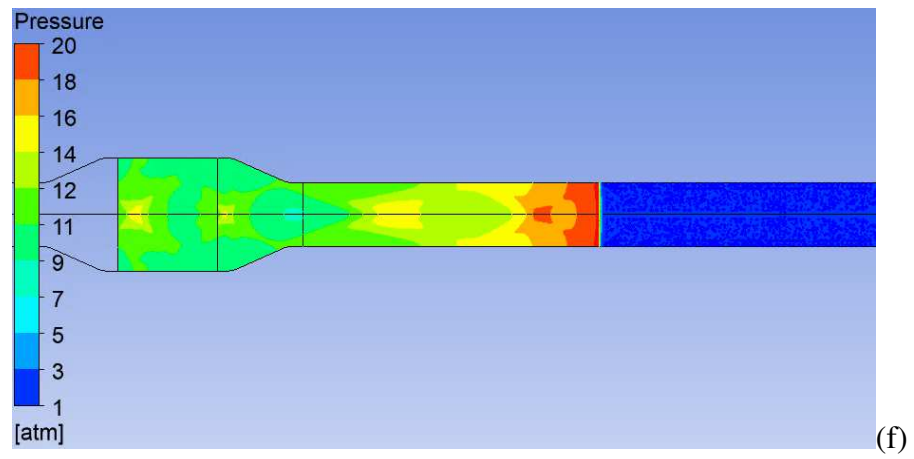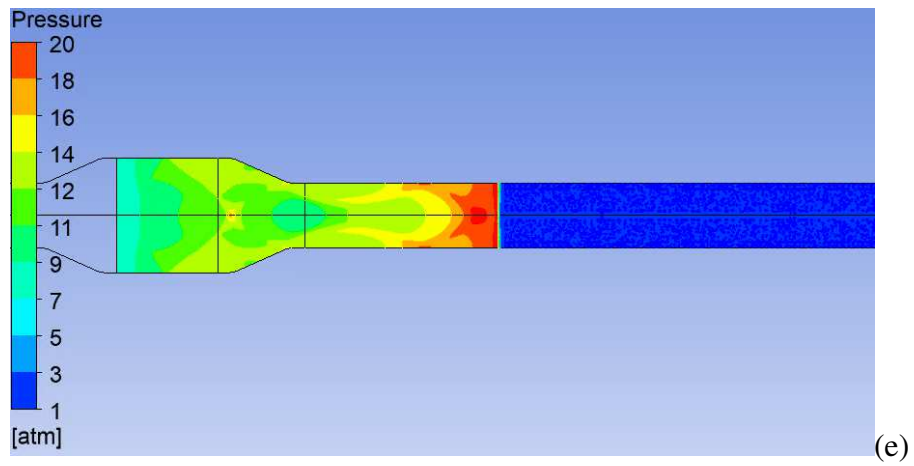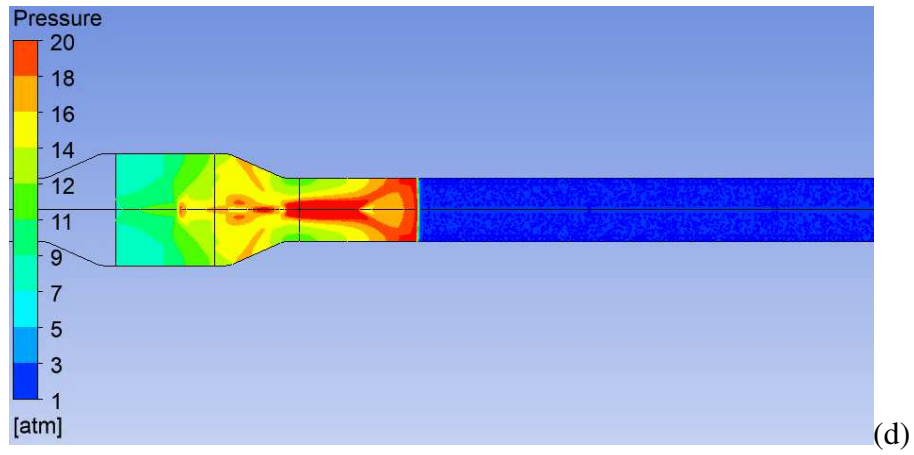
Figure 3-46 Outlet pipe detonation propagation contours with turbulent heat transfer
(a). 24μs, (b). 25μs, (c). 26μs, (d). 27μs, (e). 29μs, (f). 32μs

3.2.7 Numerical Simulation Results Comparison

Comparison of the inviscid, turbulent adiabatic and turbulent with heat transfer model is presented in this section. The comparison shows that there is no significant difference in the inlet pipe between these models. The result observed in the inlet pipe confirms that in one dimensional, constant cross-sectional area, detonation propagation, the effect of the viscosity and heat transfer is negligible for such short distances. In the outlet flange where we have diverging cross-sectional area, there is some difference between the turbulent models and the inviscid model. Slightly higher detonation pressure and velocity is observed in the turbulent models; however, the results of the turbulent adiabatic model and the turbulent with heat transfer model are very similar. In all cases, inviscid and turbulent, the detonation pressure is reduced, and the velocity of the gas increases in the inlet flange.
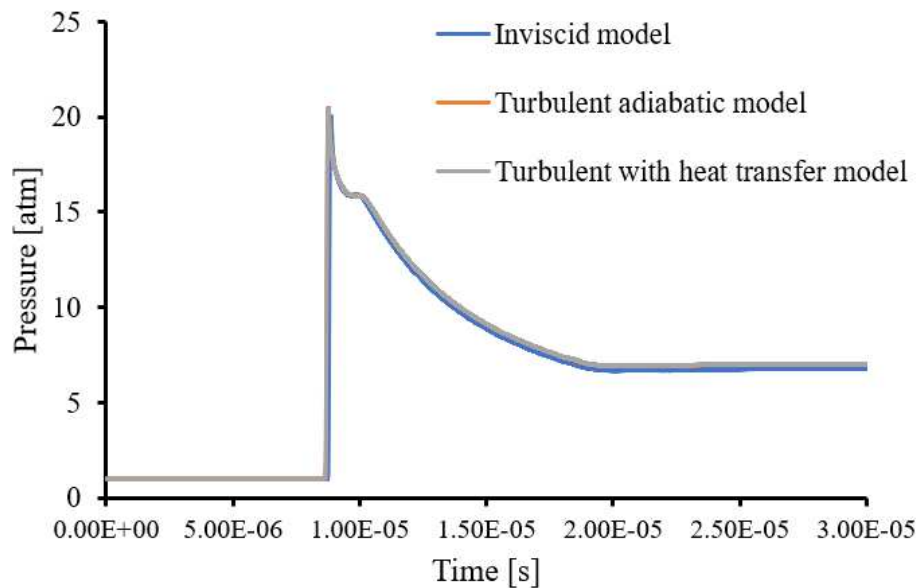
Figure 3-47 Comparison of inlet pipe pressure using different numerical models
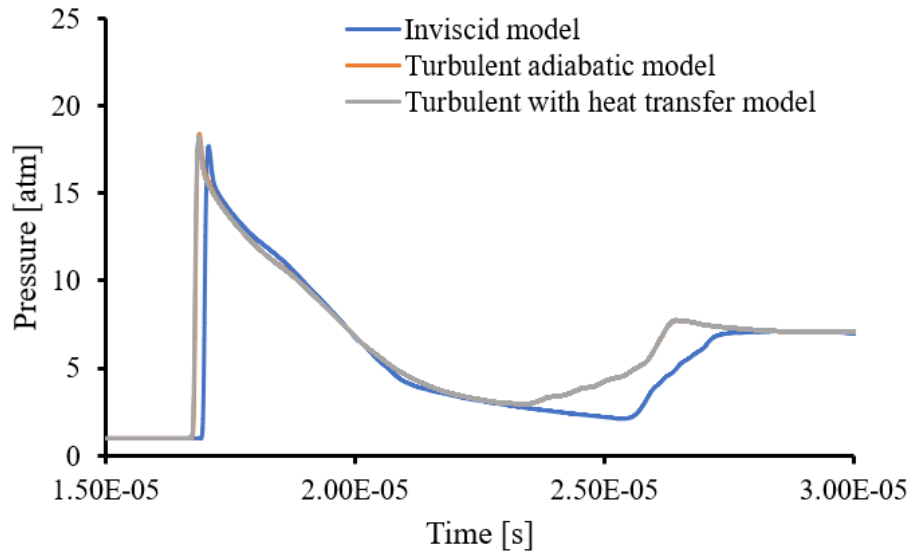
Figure 3-48 Comparison of inlet flange pressure using different numerical models
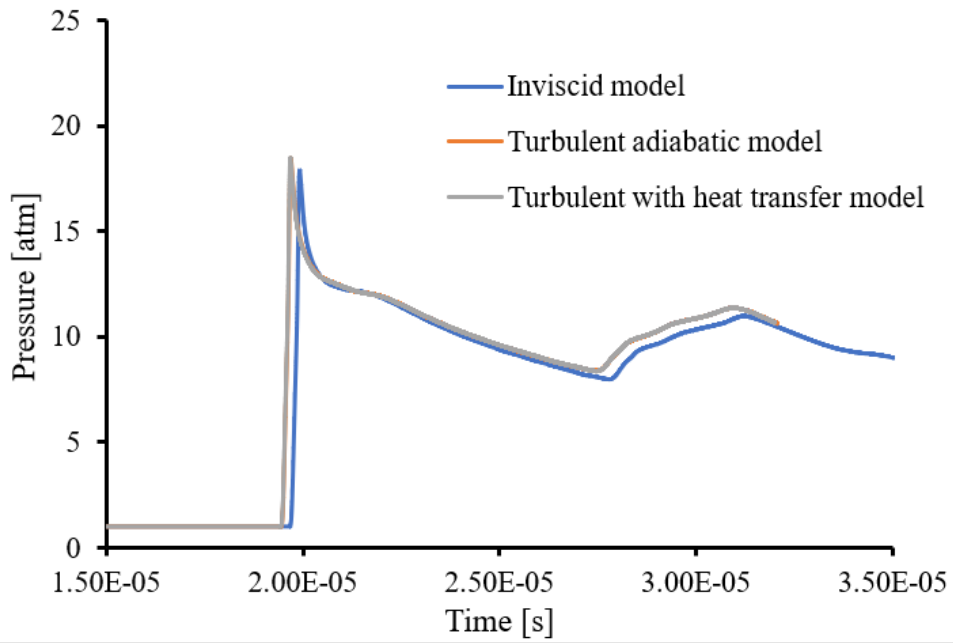
Figure 3-49 Comparison of arrestor element housing pressure using different numerical models
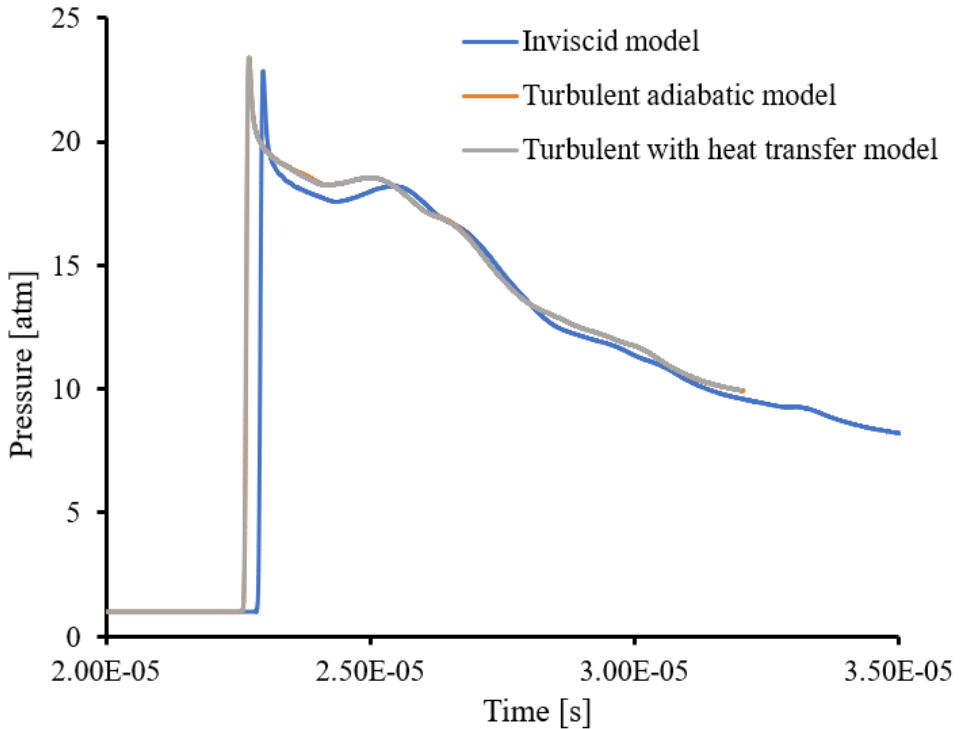
Figure 3-50 Comparison of outlet flange pressure using different numerical models

CHAPTER 4

DETONATION FLAME ARRESTOR PERFORMANCE

Numerical simulation of detonation flame arrestor performance and interaction with a detonation wave is investigated and presented in this chapter. This study includes two aspects. The first section is the study of the detonation flame arrestor effect on flow in vapor/ gas transport pipelines systems in normal operation. The second study is the evaluation of the performance of the detonation flame arrestor in interrupting detonation propagation to the protected side of the vapor/gas transport pipelines systems. In the normal operation case study, the characteristic of the flow calculated using numerical porous medium model simulation are compared with experimental results. The porous medium model characteristic used for the flame arrestor flow simulation is developed from a small-scale arrestor element sample, which has the same crimp geometry as the four-inch detonation flame arrestor. The detonation propagation and interaction with the flame element cell study is conducted using a turbulence model while the flame element is included in the simulation domain using porous medium model. Mixed wall boundary conditions are used, where the heat transfer coefficient is set to 10 w/m^2K, the free stream temperature 300 K, the external emissivity is unity, the external radiation temperature 300 K, the wall thickness 0.00038 m for element housing and flanges, and 0.0003 m for inlet and outlet pipes. The simulation domain is divided into five regions, inlet pipe, inlet flange, flame element, outlet flange and outlet pipe. The numerical simulation result is presented and reviewed for each region.

4.1 Detonation Flame Arrestor Flow Simulation Using the Porous Medium Model

The four-inch detonation flame arrestor flow characteristic is simulated using the porous medium model developed using the small-scale arrestor element sample. The simulation result is compared to experimental data for validation.

Two-dimensional axisymmetric model of a 10% scaled-down detonation flame arrestor flow test setup is used for simulation. This simulation domain has ~ 19200 quadrilateral elements and ~ 19900 nodes. The flow domain is set to air at standard pressure and temperature. The simulation is conducted varying the inlet pressure, P_1, from 0 to 70,000 Pa (0 to 10 psi) and the pressure P_2 is monitored downstream of the flame arrestor. The outlet pressure is set to 101325 Pa (1 atm). The simulation domain configuration is shown in Figure 4-1. The simulation fluid domain is defined by three regions. The inlet region which consists of the inlet pipe and the arrestor flange, set as a full fluid domain, followed by the flame arrestor element region which consists a porous annular section and a solid core, and the outlet region, which has the outlet flange and the outlet pipe defined as a full fluid domain.
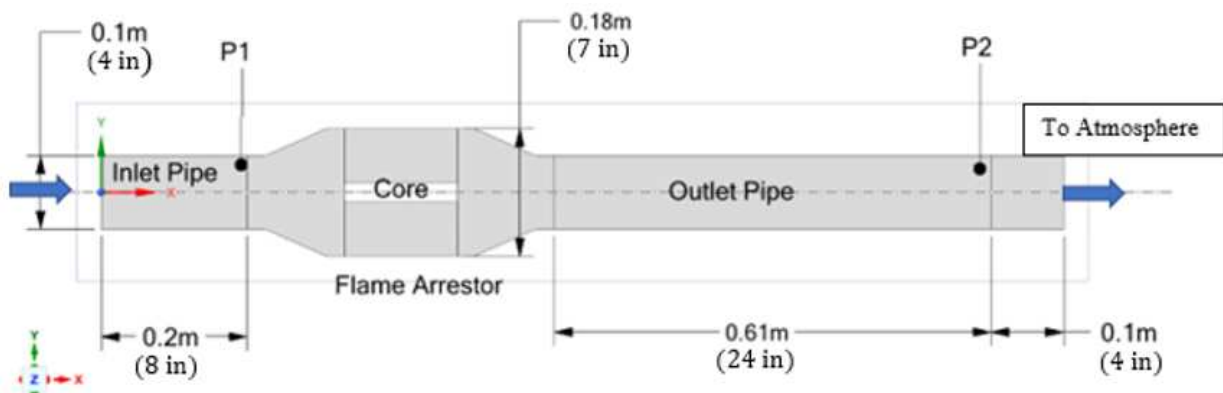
Figure 4-1 Four-inch detonation arrestor full scale domain

The arrestor element porous region is modeled by the Forchheimer equation as a momentum sink in the governing equations. The coefficients developed by the small-scale arrestor element sample is used. This is acceptable because the same crimp geometry is used for the detonation flame arrestor as the small-scale sample.

The simulation results are compared to experimental data obtained from the tests conducted at the Emerson Flow Test Laboratory in McKinney, Texas, USA. The experimental test setup schematics and photograph are shown in Figures 4-2 and 4-3. Air at standard temperature and pressure conditions is used as test gas. Piping used for the inlet and outlet is constructed from and 0.102 m (4-in) diameter schedule 40 stainless steel pipes. The detonation flame arrestor is mounted 1.53 m (60 in) downstream of the Coriolis meter that is connected to a pressure regulator (not shown) to vary from $P_1 = 0 - 69000$ Pa (0 –10 psi). The pressure P_1 is measured at 0.2 m (8 in) ahead of the detonation flame arrestor. The pressure of the flow leaving the detonation arrestor P_2 is measured at 0.61 m (24 in) downstream. The flow then left the pipe to the atmosphere through an additional 0.1 m (4 in) pipe. The pressure measurements were made with Rosemount-3051 model pressure transmitters rated for $0 - 446,000$ Pa abs ($0 - 50$ psi) with an uncertainty of 2 percent (full scale). The flow rate measurement is performed with a Micro-Motion CMF200 Coriolis flowmeter with a range of $0 - 2,800$ sm^3/h (0–100,000 scfh) with an uncertainty of 2 percent (full scale). Data were acquired by a National Instruments data acquisition system sampled at 20/s. Five data points were obtained for each measurement and averaged.
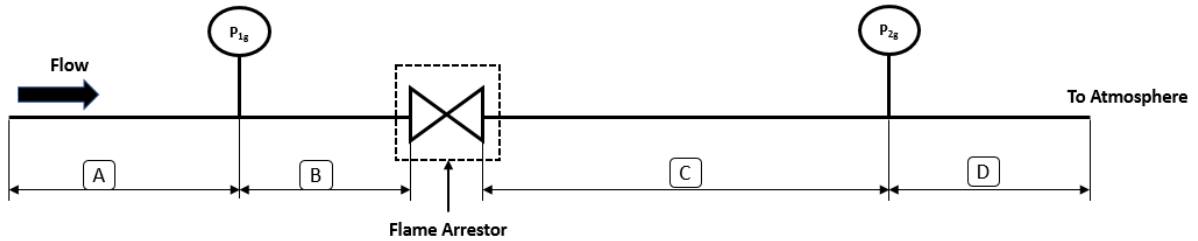
Figure 4-2 Four-inch detonation flame arrestor (DFA) test setup schematic

Figure 4-3 Four-inch detonation flame arrestor (DFA) test setup photograph

Comparison of simulation result with experimental test data is shown in Figure 4-4. The simulation result has the same trend as the experimental data. The comparison is similar to the comparison result obtained in Section 3.1.2 for the small-scale arrestor sample flow test. Some adjustments to the porosity parameter are needed to obtain result within 3% experimental data. The 3% deviation is the average value, at higher pressure drops deviation is higher up to 5% and at lower pressure drop deviation is with is within 1%.
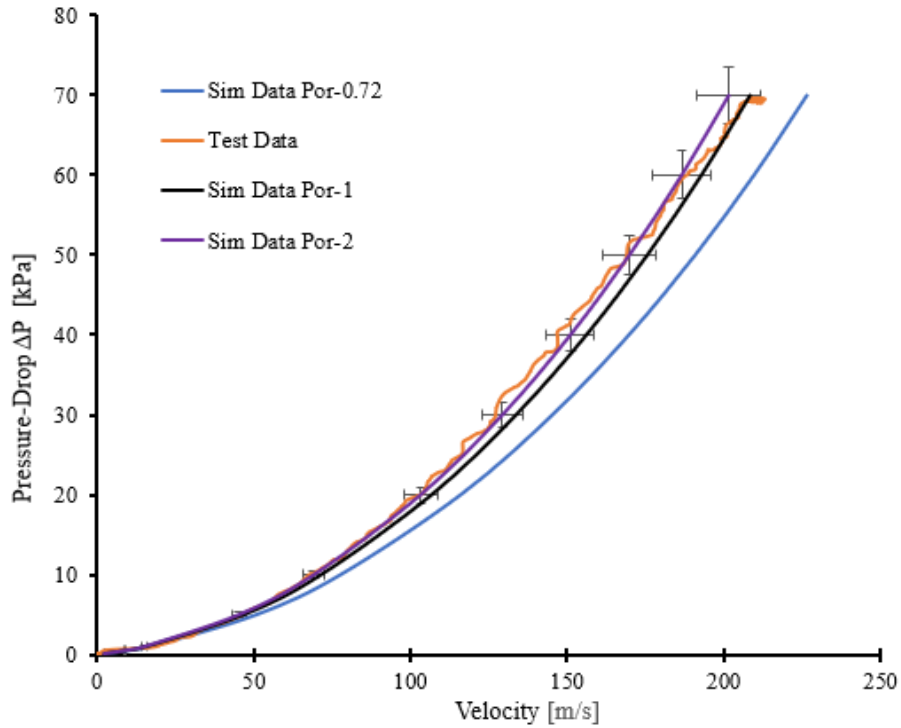
Figure 4-4 Detonation flame arrestor flow simulation data vs. experimental result.

The simulation contours of pressure and velocity, and velocity vectors are shown in Figures 4-5, 4-6 and 4-7. The pressure contour is similar to the flame arrestor element sample test; however, there is some difference in the velocity contour which can be attributed to the inlet and outlet flange geometry which acts as nozzles in the detonation flame arrestor geometry and to the solid core inside the flame arrestor element.
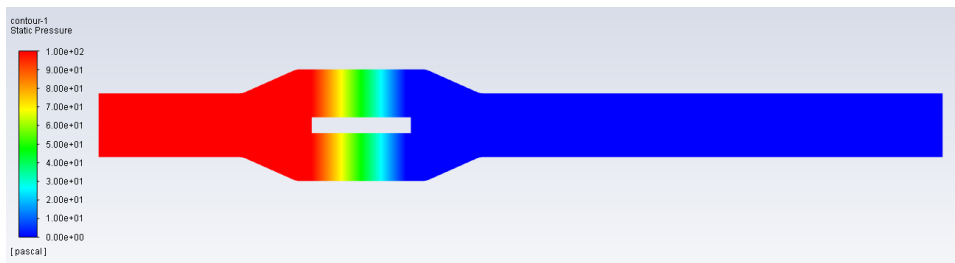
Figure 4-5 Four-inch detonation arrestor pressure contour
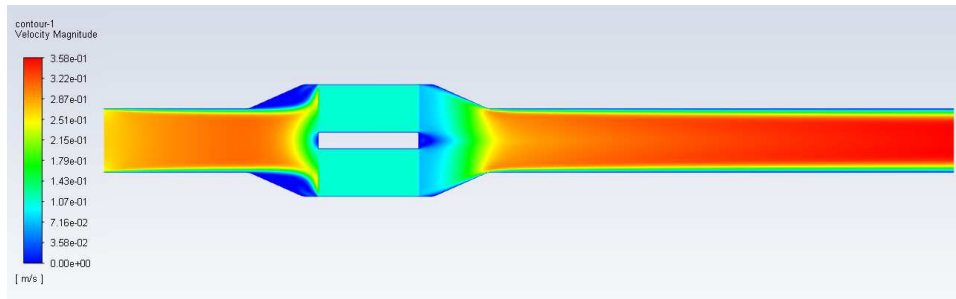
Figure 4-6 Four-inch detonation arrestor velocity magnitude contour
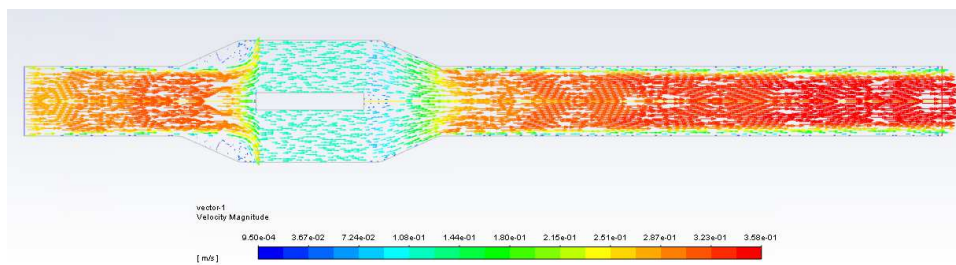
Figure 4-7 Four-inch detonation arrestor velocity vectors

4.2 Detonation Propagation Simulation Result and Discussion

The mechanism of detonation wave propagation is modeled with the axisymmetric Reynolds Averaged Navier-Stokes (RANS) equations. The Shear-Stress Transport (SST) k-ω turbulent model is used to solve the turbulent viscosity. A 21-step reaction mechanism with 19 elementary reactions and 2 duplicate reactions is used for the simulation. This reaction mechanism involves10 species, 8 reactive and 2 inert species, for hydrogen-oxygen combustion.

A ten-percent scaled down 4-inch detonation flame arrestor test setup is used for the computational domain in the detonation propagation numerical simulation. The simulation domain is shown in Figure 4-8 and the initial and boundary conditions are presented in Table 4-1
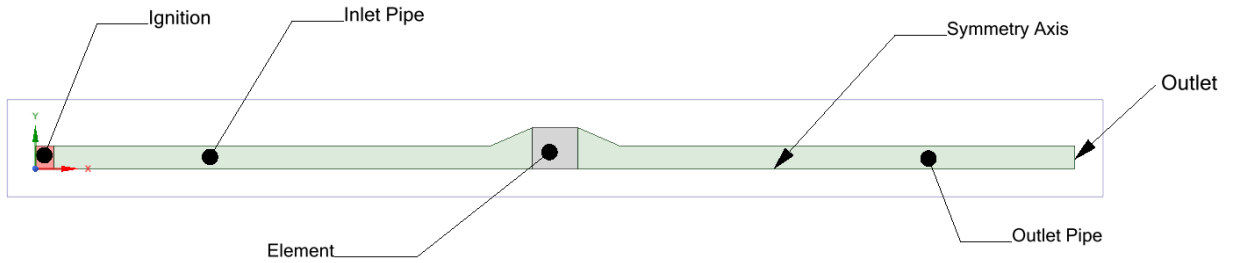
Figure 4-8 Computational domain for detonation simulation

Characteristic		Ignition	Inlet Pipe	Flame Arrestor Flanges & Element	Outlet Pipe
Temperature		3500 K	300 K	300 K	300 K
Pressure		35 atm.	1 atm.	1 atm.	1 atm.
Gas Mixture		Stoichiometric H_2/O_2 Detonation Mixture	H_2/O_2 Stoichiometric Mixture	H_2/O_2 Stoichiometric Mixture	H_2/O_2 Stoichiometric Mixture
Wall Boundary Condition	Momentum	Stationary wall No Slip Smooth	Stationary wall No Slip Smooth	Stationary wall No Slip Smooth	Stationary wall No Slip Smooth
	Thermal	Adiabatic	Mixed*	Mixed*	Mixed*
	Species	No Diffusion	No Diffusion	No Diffusion	No Diffusion

Table 4-1 Initial and boundary conditions for detonation simulation

Mixed wall boundary conditions are used, where the heat transfer coefficient is set to 10 w/m^2K, the free stream temperature 300 K, the external emissivity is unity, the external radiation temperature 300 K, the wall thickness 0.00038 m for element housing and flanges, and 0.0003 m for inlet and outlet pipes. The simulation domain is divided into five regions, inlet pipe, inlet

flange, flame element, outlet flange and outlet pipe. The numerical simulation result is presented

and reviewed for each region.
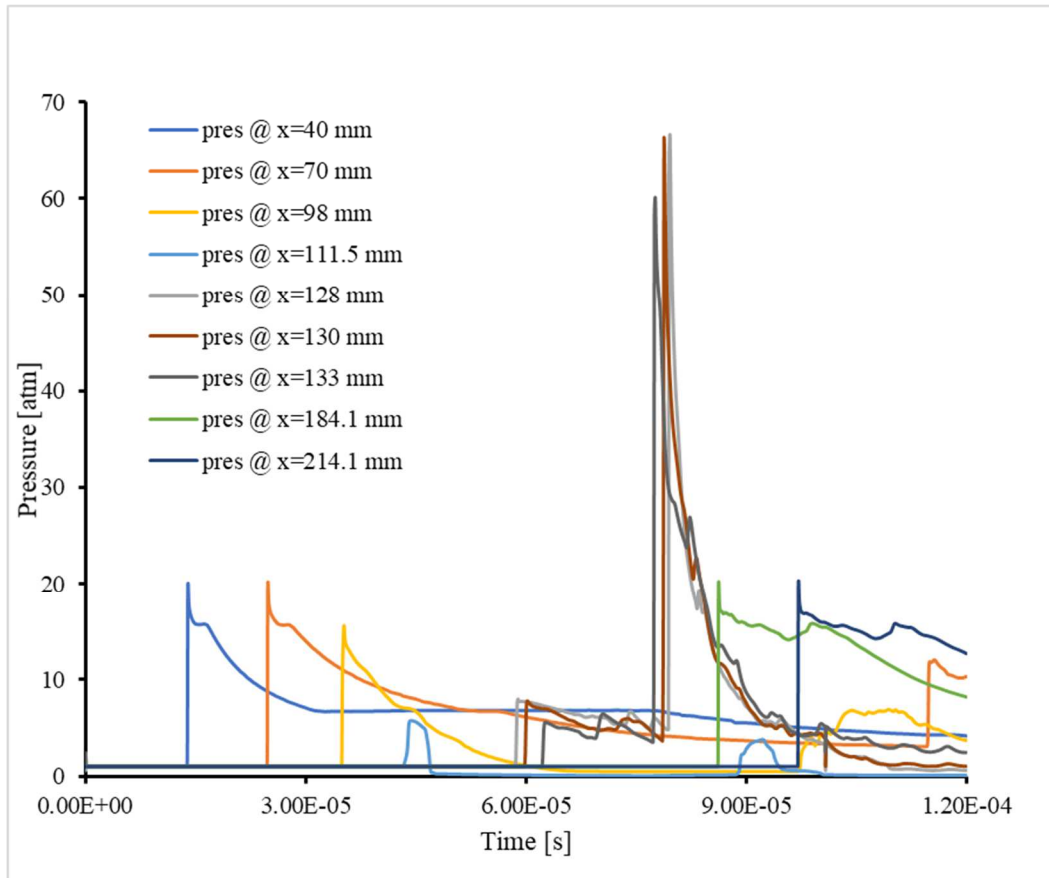
Figure 4-9 Detonation pressure history

The simulation result for the four-inch flame arrestor is different from the test setup

simulation result in the crimped flame arrestor element region. The flame arrestor element, namely,

the porous region, stops the detonation from propagating the propagation of the detonation. A

shockwave of 7 to 9 atm magnitude is observed passing through the crimped flame arrestor

element. At the outlet flange the shock wave is reflected from the walls. At the connection of the

outlet flange to the outlet pipe, the reflected shockwaves collide with each other and the incident

shock wave, generating a spot with very high pressure and temperature. This high temperature and pressure cause self ignition of the stochiometric hydrogen/oxygen mixture. The combustion adds to the increase in temperature and pressure, creating an unstable detonation with a pressure of up-to 70 atm in the outlet flange and outlet pipe. This exreamly high detonation pressure and temperature accelerates the reacting gas flow which eventually catches up with the detonation wave and slows it down. Close to the end of the outlet pipe stable detonation propagation is observed similar to the inlet pipe.
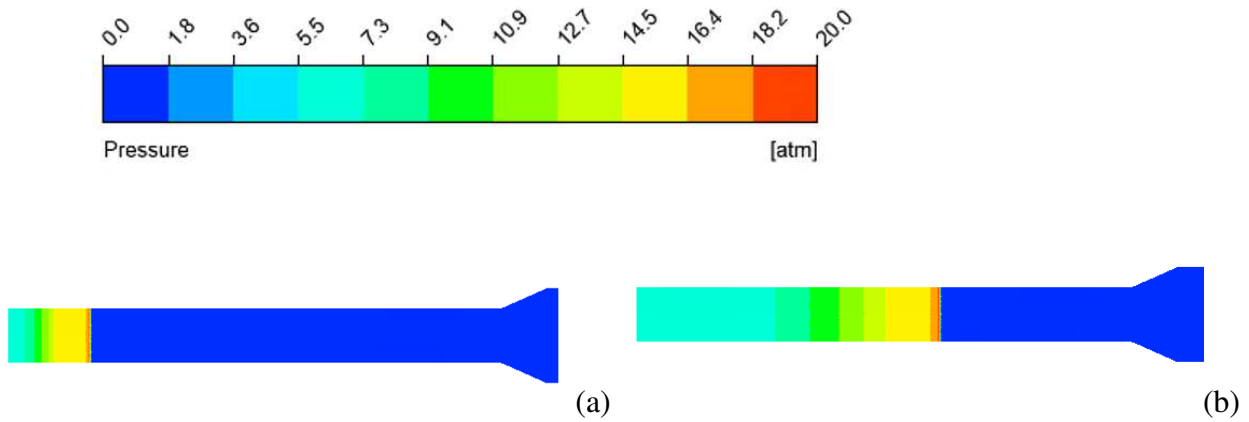
Figure 4-10 Inlet pipe detonation pressure contours
(a). 5μs, (b). 20μs
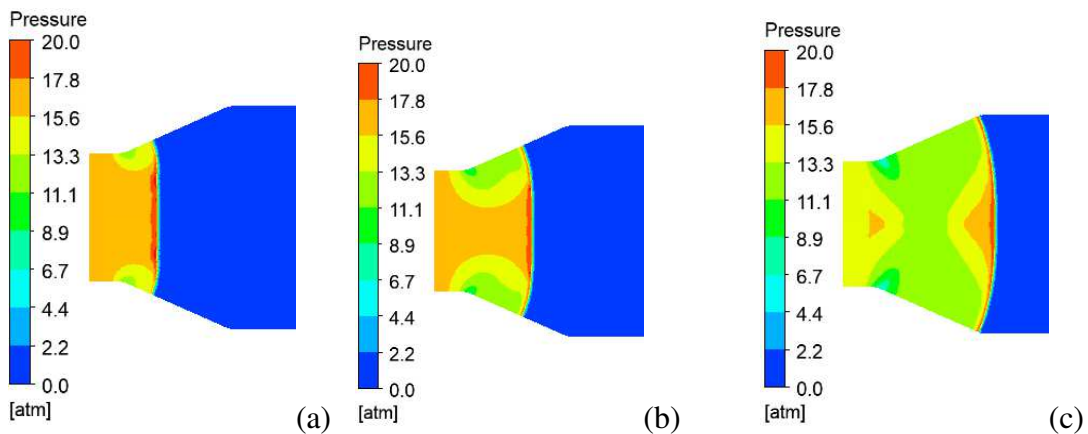
Figure 4-11 Inlet flange detonation pressure contours
(a). 34μs, (b). 35μs, (c). 35.5μs

(a)   (b)   (c)
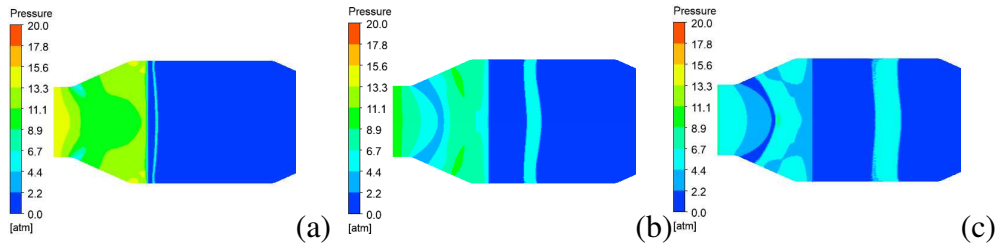
Figure 4-12 Flame arrestor element detonation pressure contours
(a). 38μs (b). 43μs (c). 48μs

(b)   (c)   (d)

(e)   (f)   (g)
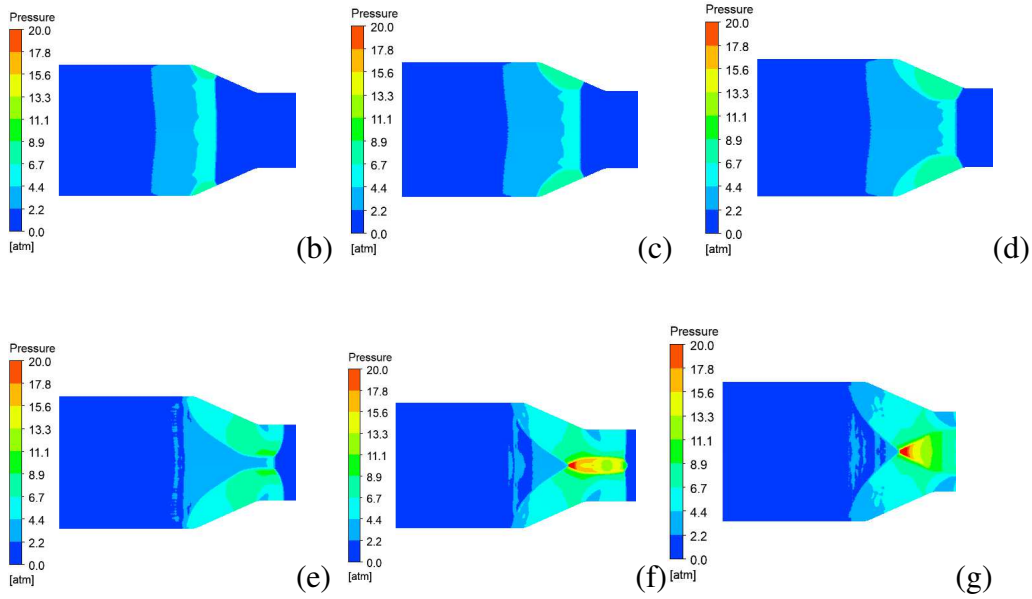
Figure 4-13 Outlet flange detonation pressure contours
(a). 56μs (b). 58μs, (c). 60μs, (d). 60μs, (e). 63μs, (f). 65μs

(a)
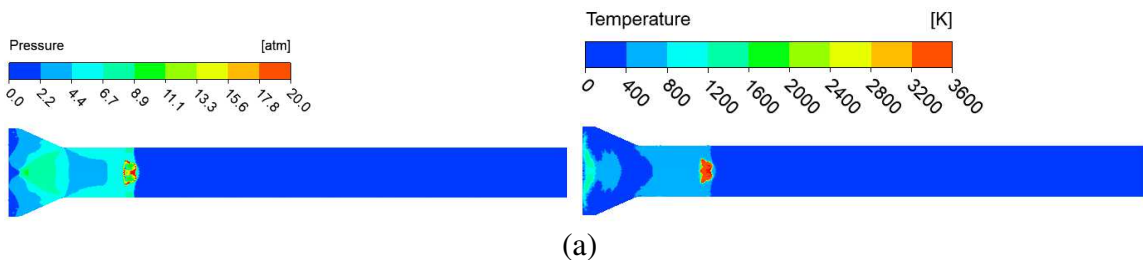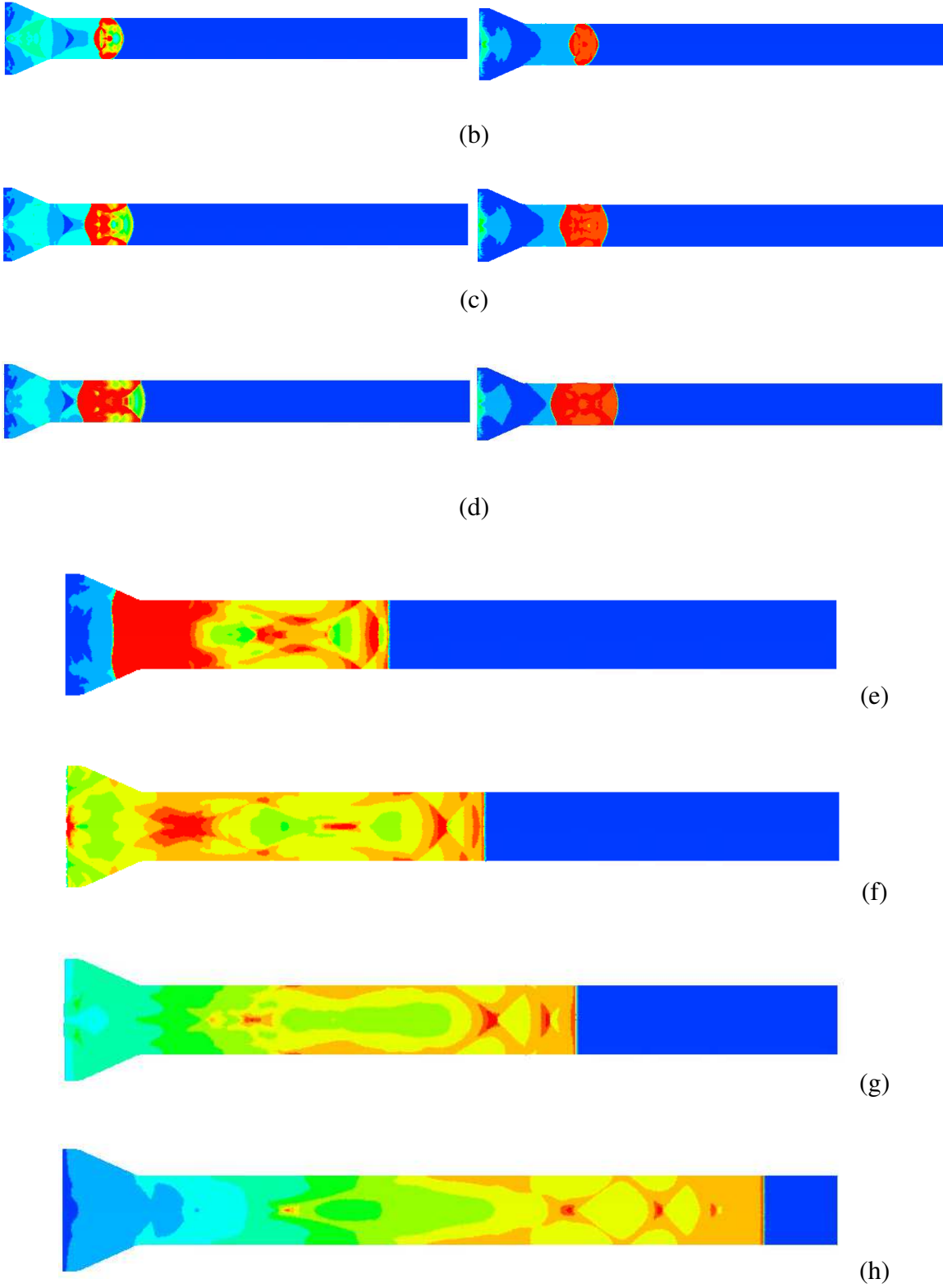
Figure 4-14 Outlet pipe detonation pressure contours
(a). 72μs (b). 73μs (c). 74μs, (d). 75μs, (e). 75μs, (f). 80μs, (g). 90μs, (h). 100μs

4.3 Comparison with Experimental Test Data

The historical test data considered for review and comparison with the numerical simulation result was from a 2017 test conducted by Aber Shock and Detonation Research Limited Laboratory in the United Kingdom. There are some differences between the experimental test setup and the numerical simulation setups. Comparison of the experimental and the numerical simulation setups is summarized in Table 4-2. Since there is a significant difference between test setup and numerical simulation setup, the comparison is only qualitative.

Item	Experimental Test Setup	Numerical Simulation Setup	Variation
Test setup piping	Per ISO 16852:2016 Detonation Arrestor Test	Based on experimental test configuration. Scaled down 10%	Same
Arrestor size pipe diameter	4 in (0.1016 m)	0.4 in (0.01016 m)	Same
Flame Element	8 in (0.2032) diameter printed arrestor element	8 in (0.2032) diameter simplified* crimped arrestor element model	Different
Fuel	Group IIA Gas (nominal 4.2 % C3H8 in air mixture)	Hydrogen-oxygen stoichiometric mixture	Different
Monitoring location	Per ISO 16852-2016	Same as test location.	same

Table 4-2 Comparison of experimental and numerical simulation setups

* The simulation domain is modeled as a single porous medium model where the overall length of the porous medium is equivalent to the detonation arrestor element. In the actual detonation arrestor product, the flame element is made from four flame elements sections separated

by the thin meshed plates. The other deviation from the actual detonation crimped element is the center solid core is not included in the numerical simulation.

The pipe arrangement for the detonation test is based on the international standard ISO 16852-2016 [10] for stable detonation flame arrestor validation and is presented in Figure 4-15. The simulation domain is constructed using a simplified configuration of this test setup, and it is shown in Figure 4-16. In the test set up, one of the challenges is initiating detonation and creating a stable detonation wave ahead of the flame arrestor element that was being tested. Increasing the inlet pipe length and using turbulence enhancing rings are some of the methods used in this testing to overcome these challenges. The method described in detail in chapter 3 is used to initiate detonation in the simulation domain, where a small section (~ 2 mm) by the left wall is assigned high energy, temperature and pressure, with chemical species that represent a detonation reaction of stoichiometric hydrogen-oxygen combustion. The rest of the domain is filled with stochiometric hydrogen-oxygen mixture.
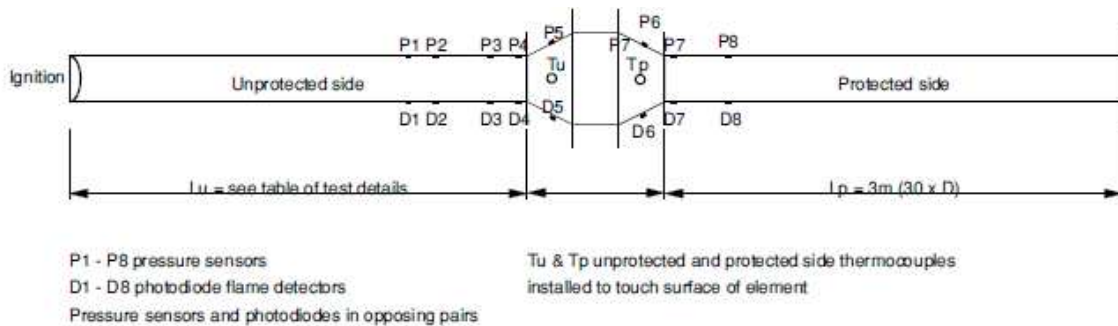
Figure 4-15 Detonation flame arrestor validation test setup configuration
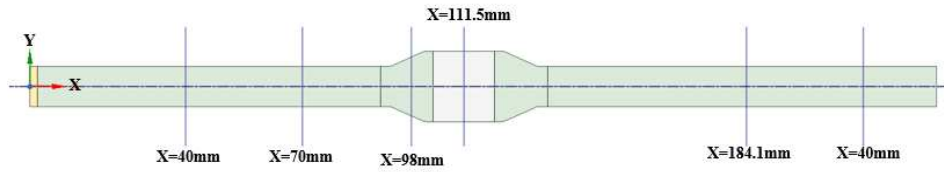
Figure 4-16 Detonation propagation simulation computational domain

Pressures at P3, P4 and P5 are compared to the numerical simulation result data at similarly

scaled location. This pressure time history data comparison is presented in Figure 4-22.
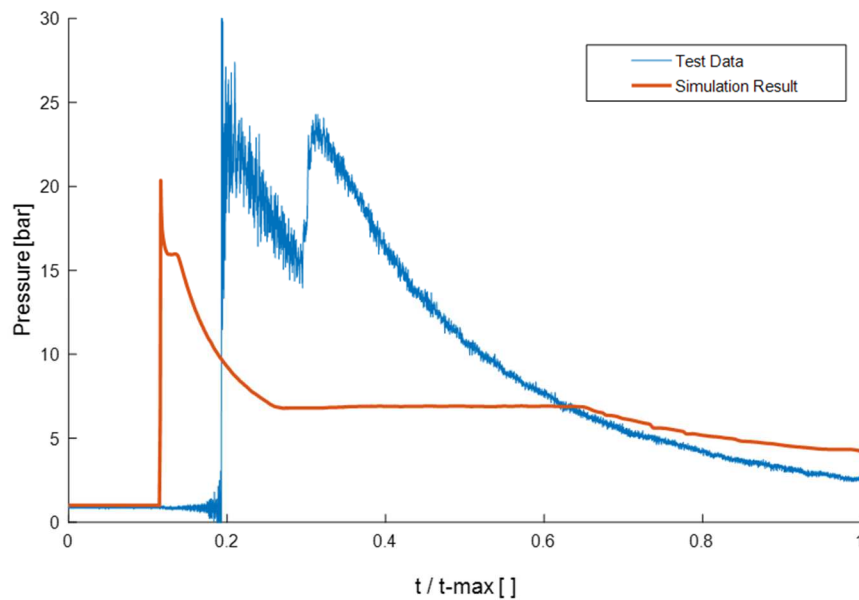
(a) P3 location inlet pipe
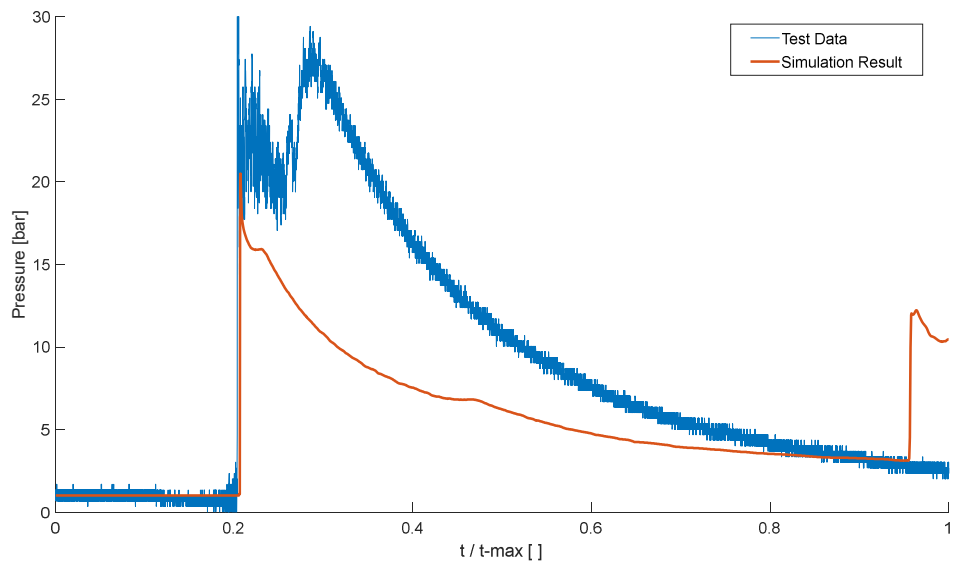
(b) P4 location inlet pipe
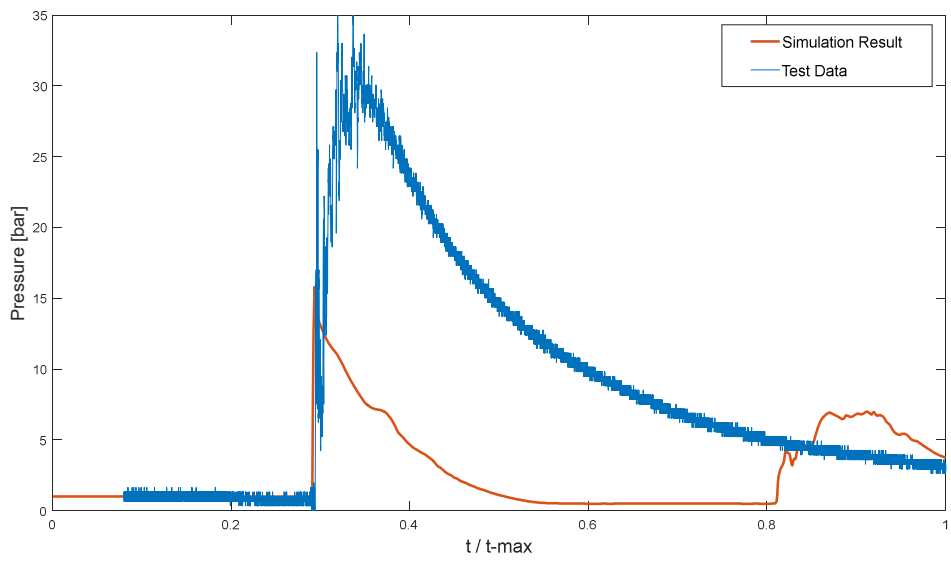
(c) P5 location inlet flange
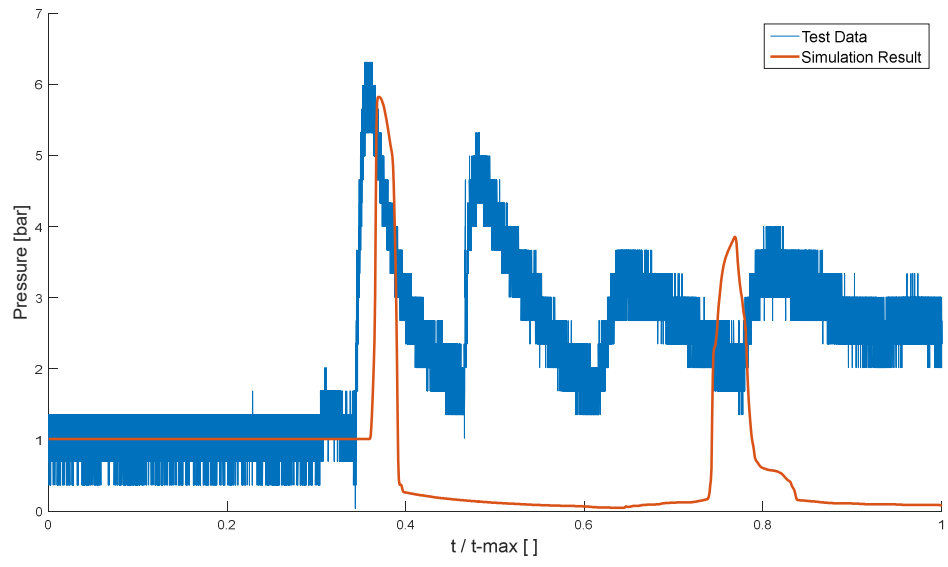
(d) P6 location outlet flange

Figure 4-17 Aber Shock printed flame arrestor detonation test vs. simulation data

4.4 Detonation Propagation Simulation Using Printed Arrestor Element Model.

In this section, the effect of changing the porous medium parameters on the detonation propagation through the flame arrestor element is evaluated. A numerical simulation of detonation propagation in a flame arrestor product with different flame element geometry is conducted. The flame element with lattice structure is prepared using additive manufacturing technology. The porous medium model for the printed flame arrestor element is developed using the method presented in Section 3. The Forchheimer equation developed from the flow test data shown in Figure 4-18 is used to calculate the permeability $1/\alpha$ and the inertial resistance coefficient C_2.
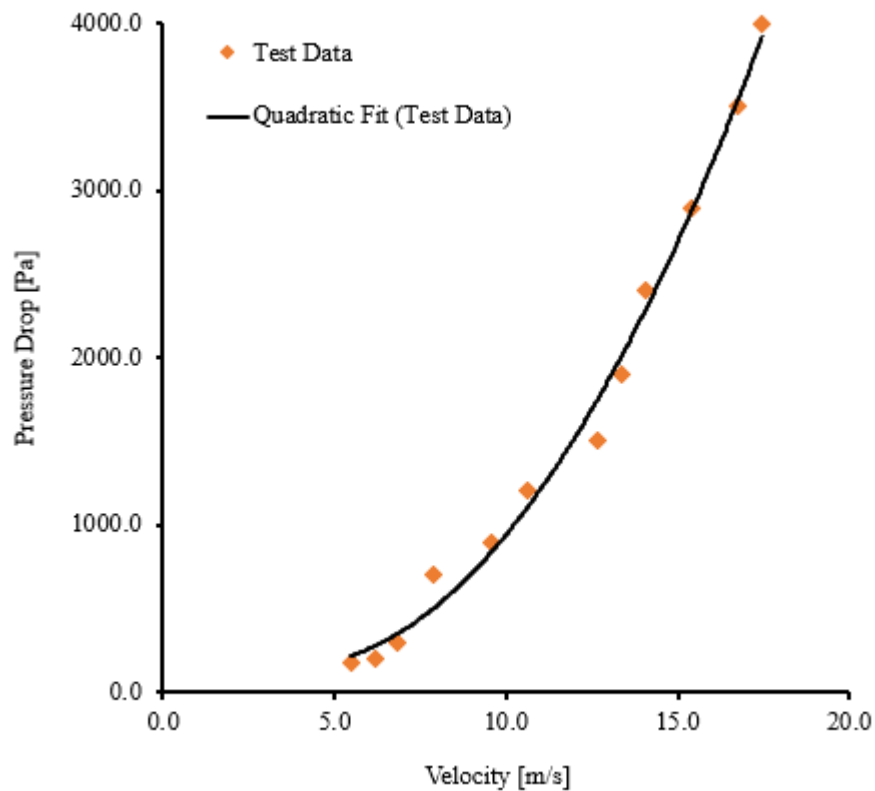
Figure 4-18 Printed flame arrestor flow test data

Detonation propagation simulation was conducted using the same setup and boundary conditions as the 4-inch crimpled flame arrestor, in Section 4.2. The porous medium parameters developed from the printed flame arrestor flow test data were used for the numarical simulation.

The main difference observed in the detonation characteristics is in the flame element region and beyond. The inlet pipe and the inlet flange have the same detonation characteristics as the crimped flame arrestor simulation result. The shock wave transmitted through the printed flame arrestor element is weaker, approximately fifty percent lower compared to the shock wave transmitted through the crimped flame arrestor element. The transmitted shock wave and the reflected waves from the walls are not strong enough to create self-ignition of the stoichiometric hydrogen/oxygen mixture. The numerical simulation result is the same as the experimental detonation propagation recently conducted on the printed flame arrestor [39].
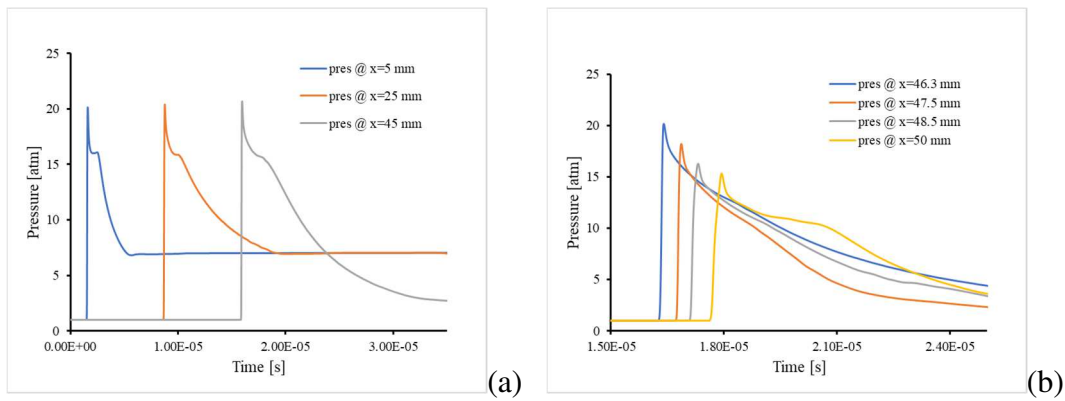
Figure 4-19 Printed flame element detonation pressure
(a) Inlet pipe, (b) Inlet flange
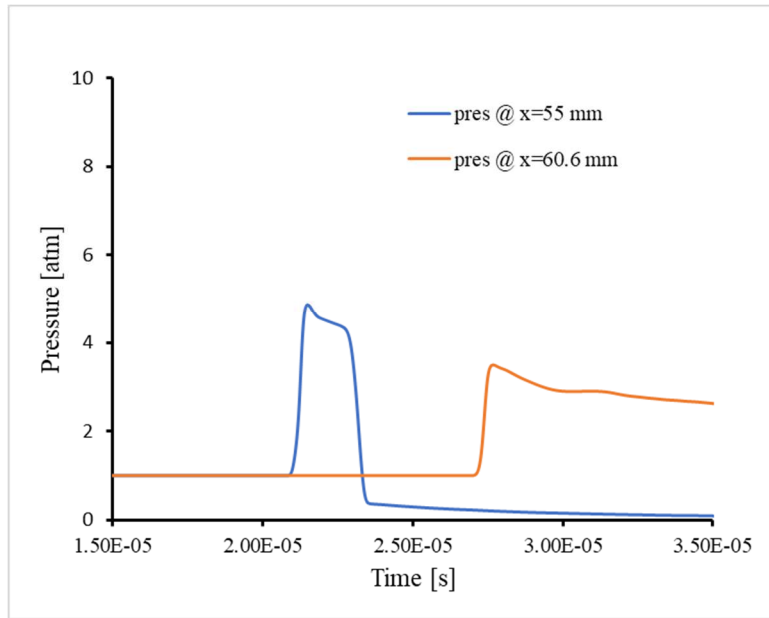
Figure 4-20 Printed flame element detonation pressure: flame arrestor element
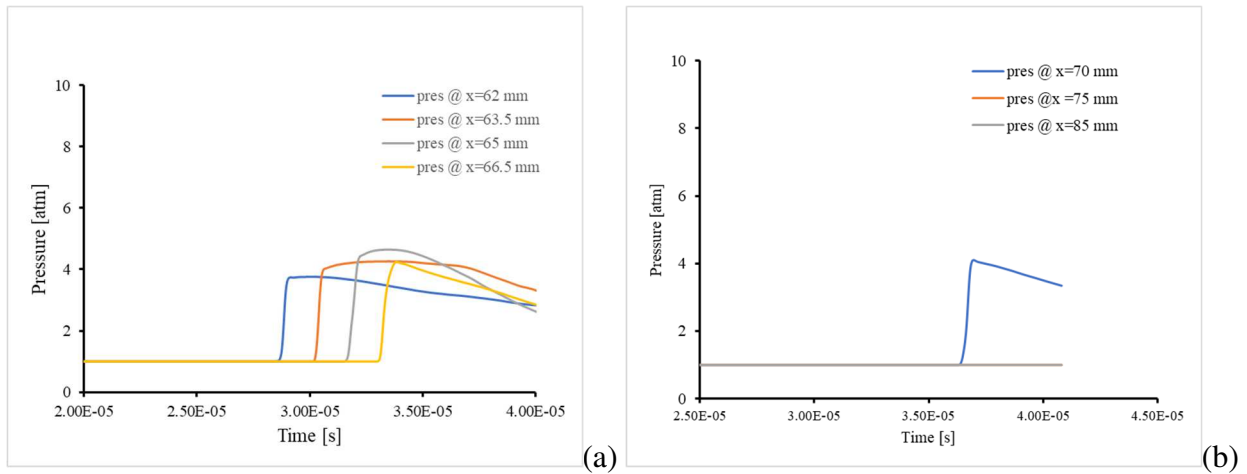
Figure 4-21 Printed flame element detonation pressure
(a) Outlet flange, (b) Outlet pipe
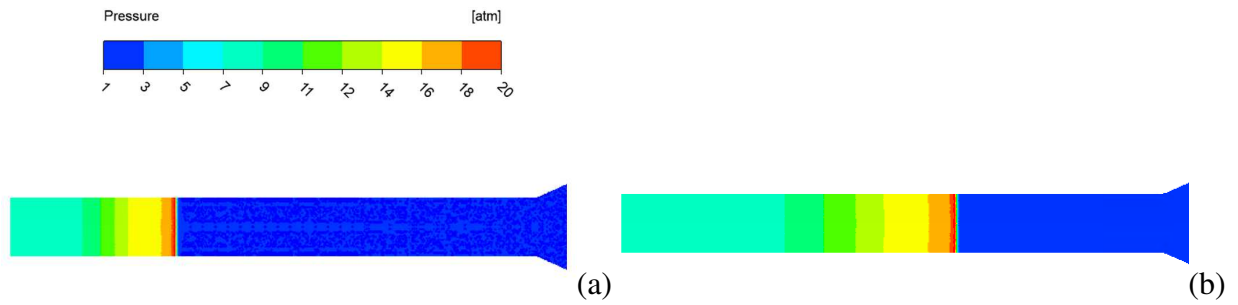
Figure 4-22 Printed flame element pressure contour: inlet pipe
(a). 5μs, (b). 10μs
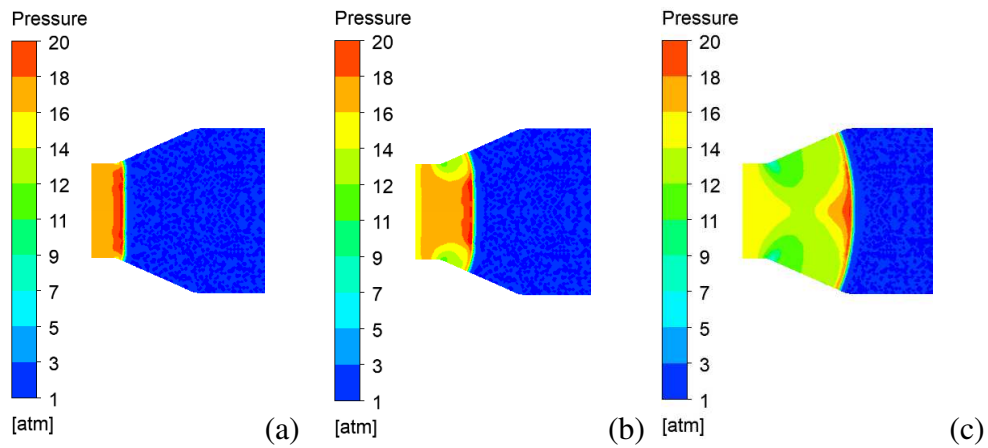
Figure 4-23 Printed flame element pressure contour: inlet flange
(a). 16.5μs, (b). 17μs, (c). 18μs
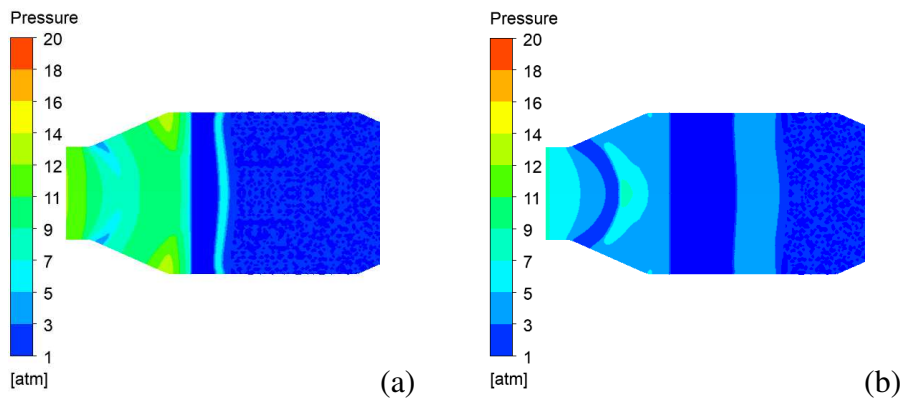
Figure 4-24 Printed flame element pressure contour: flame arrestor element
(a). 20μs, (b). 24μs

97

The shock wave in the printed arrestor element is weakened in the porous medium model compared to crimped flame arrestor element.
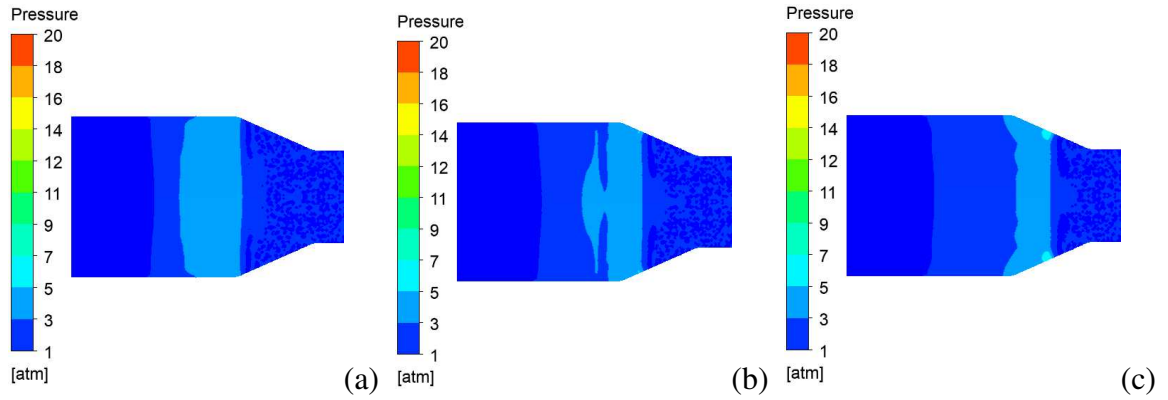
Figure 4-25 Printed flame element pressure contour: outlet flange
(a). 28μs, (b). 29μs, (c). 30μs
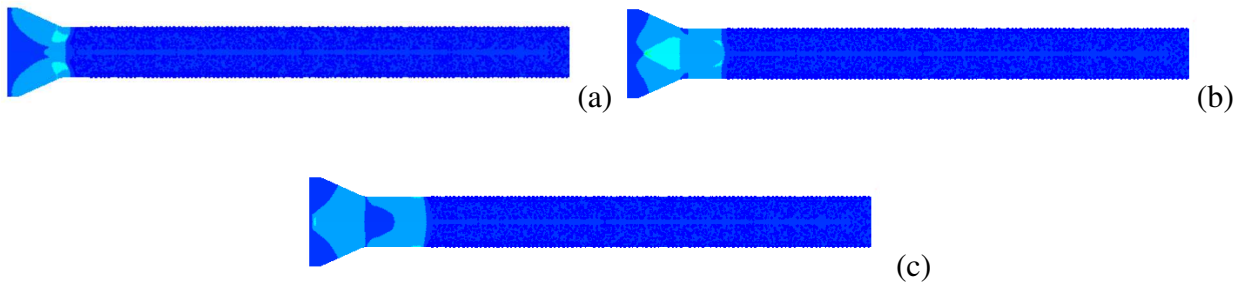
Figure 4-26 Printed Flame Element Detonation Pressure Contour: Outlet Pipe
(a). 32μs, (b). 36μs (c). 38μs

CHAPTER 5

CONCLUSIONS

A numerical simulation method for chemically reacting turbulent flows is developed to investigate detonation flame arrestor performance. A novel approach is used to model the flame arrestor element with porous medium using the Forchheimer equation. A stochiometric hydrogen-oxygen, thermally perfect reacting gas mixture with detail chemistry is used for the detonation propagation simulation using ANSYS® Fluent™ software. The 21-step hydrogen-oxygen reaction mechanism with 10 species chemical kinetic mechanism, thermodynamic database and the transport parameters were obtained from the Lawrence Livermore National Laboratory database in CHEMKIN format and directly imported to the software.

The Forchheimer equation is added to the governing conservation equation as a momentum sink to represent the porous medium, the flame arrestor element region. The Forchheimer equation proportionality coefficients are determined experimentally from the data obtained using a small-scale detonation flame arrestor element sample flow test. The flow of 4-inch detonation flame arrestor is simulated using these parameters. The results are validated using experimental flow test data. The use of a porous medium model to represent the flame arrestor element in the simulation domain is validated.

The axisymmetric reactive turbulent flow Navier-Stokes equations were solved using a finite volume 2nd order upwind Advective Upstream Splitting Method (AUSM) flux differencing scheme and explicit time stepping regime using 4th-order Runge-Kutta scheme. A volumetric reaction model with no turbulence-chemistry interaction (TCI) is used in this simulation. The

chemical source terms are computed using stiff chemistry solver using the general reaction rate expressions without considering the turbulent fluctuations effect on the source term calculations. In-Situ Adaptive Tabulation (ISAT) is used by the software to accelerate the detailed stiff chemistry calculation. The boundary conditions at the solid wall are assigned to as no-slip condition for the velocity, mixed heat transfer condition for the thermal and non-catalytic condition for species. The initial condition is set to stochiometric hydrogen-oxygen mixture at standard temperature and pressure. Detonation is initiated by assigning high energy to a small region by the left wall. The outlet boundary condition is set to stoichiometric hydrogen-oxygen mixture at standard temperature and pressure.

The numerical method is validated using a detonation tube simulation and comparison with one-dimensional analytical solution. In the detonation tube simulation, a mesh sensitivity analysis is conducted to determine the optimum grid spacing that will result in acceptable detonation macroscopic properties and minimize computational intensity. From this study, it is determined that a grid spacing of 0.1 mm is the optimum value. A timestep of 0.1 – 1 ns is used in the simulation; this timestep is monitored by the Fluent™ solver and adjusted automatically to adhere to the Courant-Friedrichs- Lewy (CFL) condition. A computational domain based on the flame arrestor validation test setup configuration is used to evaluate the inviscid model, the turbulent adiabatic model and the turbulent with heat transfer turbulent model. Detonation propagation simulations are conducted using these three models. The numerical simulation result shows that there is no significant difference between the three models in the detonation propagation characteristics.

In the flame arrestor test setup configuration, the detonation propagation characteristic, in the variable cross-sectional area, inlet and outlet flange is interesting. In the inlet flange the

detonation pressure decreases, the velocity of the gases behind the detonation wave increases and reflection of pressure wave from the wall are observed. In the element housing the detonation wave pressure increases gradually and when it reaches the outlet flange the pressure increases further due to decreasing flow area. Extreme change occurs when the reflected wave from the boundaries collides with incoming wave and generate a very high pressure and sets the detonation to the unstable region. In the outlet pipe the reacting gas velocity keep on increasing due to very high detonation pressure and eventually catches up with the detonation wave and weakens the detonation pressure bringing it back to stable detonation.

The interaction of the flame arrestor element with the detonation propagation is studied by including the flame arrestor element in the detonation propagation simulation using the porous medium model. The flame element region in the simulation domain is set as a porous medium. Two porous media characteristics were used in the simulation. In the first simulation the parameters of the porous medium model developed for crimped flame arrestor element using the flow test were used. In the second case the porous medium parameters developed using historical experimental data of printed flame arrestor element is used.

The numerical simulation results of detonation propagation in the porous medium model of the crimped flame arrestor element has shown that, the flame arrestor element has interrupted the detonation wave propagation. However, there is a transmission of a strong shock wave through the porous medium. The transmitted shock is reflected from the wall of the outlet flange. At the end of the flange, the smallest cross-sectional area, the reflected shock waves collide with each other and generate high pressure and temperature leading to self-ignition in the stochiometric hydrogen-oxygen mixture and detonation. In the outlet pipe, the unstable detonation generates

extremely high pressure and temperature which accelerates the flow of the reactant which eventually catches up with the detonation wave and slows it down.

The numerical simulation result obtained using the printed element porous medium characteristics is very different compared to the simulation result from the crimped flame arrestor element. The porous medium, the printed flame element, stopped the transmission of the detonation as the crimped element simulation result in the first case. However, the transmitted shock wave through the printed flame element is weak, and the wave reflected from the walls are weaker compared to the crimped flame arrestor case and are not able to initiate self-ignition. The numerical simulation result of detonation propagation is qualitatively compared to historical test data and is shown they have very similar trend. The other significant observation from the numerical simulation result is that the crimped flame element requires additional shock attenuation mechanism to be successfully used in the detonation flame arrestor product. The numerical simulation results show the printed flame arrestor element succeeded in interrupting the detonation propagation and keeps the detonation from propagating to the protected side without any additional shock attenuation mechanism. This result agrees with recent validation test result conducted on the printed flame arrestor element.

Significant insight is gained from this study from various features of the detonation propagation characteristics, and the interaction of detonation wave with flame arrestor element. This result shows that the porous medium parameters used in the numerical simulation have significant effect on the detonation propagation, interruption or transmission of detonation wave through the porous medium. This preliminary investigation suggests that the feasibility of using numerical simulation methods in evaluating the flame arrestor performance and developing innovative detonation interruption mechanisms. A detailed parametric study of the porous medium

model parameters needs to be conducted to develop a general porous medium model. A more advanced and detailed heat transfer study is recommended for future research. The detail characteristics of the detonation wave in the porous medium region and the unsteady thrust generated on the flame element by the detonation wave were not included in this study, it is recommended for future research.

Appendix A

CHEMICAL KINETICS MECHANISM

	Reaction	A	n	E_a
	H_2/O_2 Chain Reactions			
1	$\dot{H} + O_2 = \dot{O} + \dot{O}H$	1.91×10^{14}	0	16.44
2	$\dot{O} + H_2 = \dot{H} + \dot{O}H$	5.08×10^{4}	2.67	6.292
3	$\dot{O}H + H_2 = \dot{H} + H_2O$	2.16×10^{8}	1.51	3.43
4	$\dot{O} + H_2O = \dot{O}H + \dot{O}H$	2.97×10^{6}	2.02	13.4
	H_2/O_2 Dissociation and Recombination Reactions			
5[a]	$H_2 + M = \dot{H} + \dot{H} + M$	4.57×10^{19}	-1.40	105.1
6[b]	$\dot{O} + \dot{O} + M = O_2 + M$	6.17×10^{15}	-0.50	0.00
7[c]	$\dot{O} + \dot{H} + M = O\dot{H} + M$	4.72×10^{18}	-1.00	0.00
8[d,e]	$\dot{H} + \dot{O}H + M = H_2O + M$	4.50×10^{22}	-2.00	0.00
	Formation and Consumption of HO_2			
9[f,g]	$\dot{H} + O_2 + M = H\dot{O}_2 + M$	3.48×10^{16}	-0.41	-1.12
	$\dot{H} + O_2 = H\dot{O}_2$	1.48×10^{12}	0.60	0.00
10	$H\dot{O}_2 + \dot{H} = H_2 + O_2$	1.66×10^{13}	0.00	0.82
11	$H\dot{O}_2 + \dot{H} = \dot{O}H + \dot{O}H$	7.08×10^{13}	0.00	0.30
12	$H\dot{O}_2 + \dot{O} = \dot{O}H + O_2$	3.25×10^{13}	0.00	0.00
13	$H\dot{O}_2 + \dot{O}H = H_2O + O_2$	2.89×10^{13}	0.00	-0.50
	Formation and Consumption of H_2O_2			
14[h]	$H\dot{O}_2 + H\dot{O}_2 = H_2O_2 + O_2$	4.2×10^{14}	0.00	11.98
	$H\dot{O}_2 + H\dot{O}_2 = H_2O_2 + O_2$	1.3×10^{11}	0.00	-1.629
15[i,f]	$H_2O_2 + M = \dot{O}H + \dot{O}H + M$	1.27×10^{17}	0.00	45.5
	$H_2O_2 = \dot{O}H + \dot{O}H$	2.95×10^{14}	0.00	48.4

16	$H_2O_2 + \dot{H} = H_2O + \dot{O}H$	2.41×10^{13}	0.00	3.97
17	$H_2O_2 + \dot{H} = H_2 + H\dot{O}_2$	6.03×10^{13}	0.00	7.95
18	$H_2O_2 + \dot{O} = \dot{O}H + H\dot{O}_2$	9.55×10^{06}	2.00	3.97
19h	$H_2O_2 + \dot{O}H = H_2O + H\dot{O}_2$	1.0×10^{12}	0.00	0.00
	$H_2O_2 + \dot{O}H = H_2O + H\dot{O}_2$	5.8×10^{14}	0.00	9.56
a	Efficiency factors are: $H_2O = 12.0$; $H_2 = 2.5$			
b	Efficiency factors are: $H_2O = 12.0$; $H_2 = 2.5$; $Ar = 0.75$; $He = 0.83$			
c	Efficiency factors are: $H_2O = 12.0$; $H_2 = 2.5$; $Ar = 0.75$; $He = 0.75$			
d	Original pre-exponential A factor is multiplied by two here			
e	Efficiency factors are: $H_2O = 12.0$; $H_2 = 0.73$; $Ar = 0.38$; $He = 0.38$			
f	Troe parameters; reaction 9: $a = 0.5, T^{***} = 1.0 \times 10^{-30}, T^* = 1.0 \times 10^{30}, T^{**} = 1.0 \times 10^{100}$ reaction 15: $a = 0.5, T^{***} = 1.0 \times 10^{-30}, T^* = 1.0 \times 10^{30}, T^{**} = 1.0 \times 10^{100}$			
g	Efficiency factors are: $H_2O = 14.0$; $H_2 = 1.3$; $Ar = 0.67$; $He = 0.67$			
h	Reaction 14 and 19 are expressed as the sum of the two rate expressions.			
i	Efficiency factors are: $H_2O = 12.0$; $H_2 = 2.5$; $Ar = 0.45$; $He = 0.45$			

Table A-1 Hydrogen-Oxygen Elementary Reactions Mechanism
units: cm^3, mol, s, kcal, K.

Species	ΔH_f^{298K}	S^{300K}	Specific heat capacity, C_p					
			300 K	400 K	500 K	800 K	1000 K	1500 K
$\dot{H}$	52.098	27.422	4.968	4.968	4.968	4.968	4.968	4.968
$\dot{O}$	59.56	38.500	5.232	5.139	5.080	5.016	4.999	4.982
$\dot{O}H$	8.91	43.933	6.947	6.992	7.036	7.199	7.341	7.828
H_2	0.00	31.256	6.902	6.960	6.997	7.070	7.209	7.733
O_2	0.00	49.050	7.010	7.220	7.437	8.068	8.350	8.721
H_2O	-57.77	45.154	8.000	8.231	8.446	9.223	9.875	11.258
$H\dot{O}_2$	3.00	54.809	8.349	8.886	9.465	10.772	11.380	12.484
H_2O_2	32.53	55.724	10.416	11.446	12.346	14.294	15.213	16.851
N_2	0.00	45.900	6.820	7.110	7.520	7.770	8.280	8.620
Ar	0.00	37.000	4.900	4.900	4.900	4.900	4.900	4.900
He	0.00	30.120	4.970	4.970	4.970	4.970	4.970	4.970

Table A-2 Thermodynamic Database.

units: $\Delta H_f^{298.15\,K} \equiv kcal/mol$, S^{300K} and $C_p(T) \equiv cal/mol\,K$

Species	Geometry	ε/kg	Σ	$\overline{\mu}$	α	Z^*_{rot}
Ar	0	136.5	3.33	0	0	0
H	0	145.0	2.05	0	0	0
H_2	1	38.0	2.92	0	0.79	280
H_2O	2	572.4	2.605	1.844	0	4
H_2O_2	2	107.4	3.458	0	0	3.8
HO_2	2	107.4	3.458	0	0	1
N_2	1	97.5	3.621	0	1.76	4
O	0	80.0	2.75	0	0	0
O_2	1	107.4	3.458	0	1.6	3.8
OH	1	80.0	2.75	0	0	0

Table A-3 Transport Database

Appendix B

ANSYS® FLUENT™ SOLVER SETUP

Direction Vector	X = 1		
	Y = 0		
Viscous Resistance (Inverse Absolute Permeability)	Direction - 1 [1/m]	4.53E+07	Determined by Flow Test
	Direction - 2 [1/m]	4.53E+10	Order of magnitude greater than direction 1
Inertial Resistance	Direction - 1 [1/m^2]	37.52	Determined by Flow Test
	Direction - 2 [1/m^2]	37520	Order of magnitude greater than direction 1
Fluid Porosity	0.72	Determined from arrestor element design	
Heat Transfer Setting	Thermal Model	Equilibrium	
	Solid Material	Steel	
Relative Viscosity	Constant	1	

Table B-1 Porous zone setting

		Models / Material		Solution Method	
Time	Transient	Energy Equation enabled		Formulation	Explicit
Type	Density Based	Inviscid Model		Flux Type	AUSM
Velocity Formation	Absolute	Species Transport		Spatial Discretization	
Operating Condition	0 atm	Mixture Material	Imported CHEMIKIN Mechanism	Gradient	Least Square Cell Based
	x=0 y=0		hydrogen-2004	Flow	Second Order Upwind
		Density	Ideal Gas		
		Reaction	Volumetric	Transient Formulation	Explicit
		Chemistry Solver	Stiff Chemistry Solver	Controls	Specific Time Step
		Turbulence-Chemistry Interaction	Finite-Rate/No TCI	Time Step	1e-09 s
		Integration Parameter	ISAT	Initialization	Standard

Table B-2 Inviscid Model Fluent™ Setting

Solver		Models / Material		Solution Method	
Time	Transient	Energy Equation enabled		Formulation	Explicit
Type	Density Based	Viscous Turbulent Model		Flux Type	AUSM
Velocity Formation	Absolute	Species Transport		Spatial Discretization	
Operating Condition	0 atm	Mixture Material	Imported CHEMIKIN Mechanism	Gradient	Least Square Cell Based
	x = 0 y = 0		hydrogen-2004	Flow	Second Order Upwind
		Density	Ideal Gas		
		Reaction	Volumetric	Transient Formulation	Explicit
		Chemistry Solver	Stiff Chemistry Solver	Controls	Specific Time Step
		Turbulence-Chemistry Interaction	Finite-Rate/No TCI	Time Step	1e-09 s ~1e-10 s
		Integration Parameter	ISAT	Initialization	Standard

Table B-3 Turbulent model Fluent™ solver setup

Model	k-ω (2 equation)
k-ω model	Shear Stress Transport (SST)
option	Production limiter
Model Constants (default value)	α^*_∞=1, α_∞=0.52, β_∞=0.09, a_1=0.31, β_1 (inner)=0.075, β_1 (outer)=0.0828, TKE_Pr (inner)=1.176, TKE_Pr (outer) =1, SDR Pr(inner)=2, SDR Pr(outer)=1.168, Energy Pr=0.85, Tur Schmidt=0.7, Production Limiter Clip Factor=10
User Defined Functions	None
Scale-Resolving Simulation Option	Not selected

Table B-4 Turbulent model k-ω parameters and setting

REFERENCES

[1].   Grossel, S.S., *Deflagration and Detonation Flame Arresters*, Wiley, 2002.

[2].   Glassman, I., Yetter, R. A. and Glumac, N. G., *Combustion*, 5th ed., Academic, 2014

[3].   Cant, R.S. and Mastorakos, E., *An Introduction to Turbulent Reacting Flows*, Imperial College, 2008

[4].   Liepmann H.W. and Roshko, A. *Elements of Gasdynamics*, Dover, 2001

[5].   Pope, S. B., *Turbulent Flows*, Cambridge, 2000

[6].   Ben-Dor, G., *Shock Wave Reflection Phenomena*, 2nd ed. 2007

[7].   Poinsot, T. and Veynante, D. *Theoretical and Numerical Combustion*, 3rd ed. 2012

[8].   John H.S. Lee, *The Detonation Phenomenon*, Cambridge, 2008

[9].   Fickett, W. and Davis, W. C. *Detonation Theory and Experiment*, Dover, 2000

[10].   ANSYS® 18.1, "ANSYS Fluent Theory Guide", 2017

[11].   ISO 16852-2016, "Flame Arresters – Performance requirement, Test Methods and Limits for Use". 2nd Edition, 2016

[12].   Melina G. Sidiropoulou, Konstadinos N. Moutsopoulos and Vassilios A. Tsihrintzis, "Determination of Forchheimer equation coefficients a and b", HP 21, 534–554, 2007

[13].   Dastan Takhanov, "Forchheimer Model for Non-Darcy Flow in Porous Media and Fractures", Thesis, Sept. 2011

[14].   H.C. Chan, W.C. Huang, J.M. Leu, C.J. Lai, "Macroscopic modeling of turbulent flow over a porous medium", International Journal of Heat and Fluid Flow 28 1157-1166, 2007

[15].   S. M. Kim, S.M. Ghiaasiaan, "Numerical Modeling of Laminar Pulsating Flow in Porous Media", Journal of Fluids Engineering, ASME, Vol. 131, 2009

[16]. Eric Skjetne, Jean-Louis Auriault, "High-Velocity Laminar and Turbulent Flow in Porous Media, Transport in Porous Media", DOI: 10.1023/A:1006582211517, 1999

[17]. James T. Peace and Frank K. Lu, "Numerical Study of Pulse Detonation Engine Nozzle and Exhaust Flow Phenomena", AIAA/SAE/ASEE Joint Propulsion Conference, 2017

[18]. Xiaodoing Cai, Jianhan Liang, Zhiyong Lin, Ralf Deiterding, "Detonation Attenuation and Re-initiation in Expanding Channels", AIAA, 2017

[19]. Jian Li, Jianguo Ning, Charles B. Kiyanda, Hoi Dick Ng, "Numerical simulation of cellular detonation diffraction in a stable gaseous mixture", Propulsion and Power Research 5(3):177-183, 2016

[20]. Hua-Shu Dou, Her Mann Tsai, Boo Cheong Khoo, Jianxian Qiu, "Simulation of detonation wave propagation in rectangular ducts using a three-dimensional WENO scheme", Combustion and Flame 154 644-659, 2008

[21]. Génin, Franklin & Fryxell, B. & Menon, Suresh. "Simulation of Detonation Propagation in Turbulent Gas-Solid Reactive Mixtures", 2005

[22]. ShaoChen Sun, Yuan Shu, Yu Feng, DaChao Sun, HaiTao Long and MingShu Bi. "Numerical simulation of detonation wave propagation and quenching process in in-line crimped-ribbon flame arrester". Cogent Engineering Volume5, 2018

[23]. O'Connaire, M., H. J. Curran, J. M. Simmie, W. J. Pitz, and C. K. Westbrook, "A Comprehensive Modeling Study of Hydrogen Oxidation," Int. J. Chem. Kinet., 2004

[24]. J.E. Shepherd, "Chemical Kinetics of Hydrogen-Air-Diluent Detonation, Progress in Astronautics and Aeronautics", Vol. 106, pp 263-293, 1986

[25]. Juan Li, Zhenwei Zhao, Andrei Kazakov, and Frederick L. Dryer, "An updated Comprehensive Kinetic Model of Hydrogen Combustion", International Journal of Chemical Kinetics, Vol. 36, page 566-575, 2004

[26]. Tae-Hyeong Yi, "Numerical Study of Chemically Reacting Viscous Flow Relevant to Pulsed Detonation Engines", UTA, Dissertation, 2005

[27]. Thomas, Geraint & Oakley, Gwyn, "Pipeline explosions I: An evaluation of MESG as a relative measure of potential explosion severity and the genesis of a mimic gas concept for explosion hazard testing", 5th Int. Seminar on Fire and Explosion Hazards, 2019

[28]. D.J. Part, A.R. Green and Y.C. Chen, "Analysis of Local Flame Propagation in Gas Explosions with Multiple Obstacles", 15th Australasian Fluid Mechanics conference The University of Sydney, 2004

[29]. Geraint Thomas, Gwyn Oakley, Richard Bambrey, "An experimental study of flame acceleration and deflagration to detonation transition in representative process piping", Process Safety and Environmental Protection, Volume 88, Issue 2, Pages 75-90, ,2010

[30]. J.T. Peace, F.K. Lu, "Detonation-to-Shock wave transmission at a contact discontinuity", Shock Waves, 2018

[31]. G. Yu. Bivol, S. V. Golovastov, V. V. Golub, "Detonation suppression in hydrogen–air mixtures using porous coatings on the walls", Shock Waves, Volume 28, Issue 5, pp.1011-1018, 2018

[32]. G.O. Thomas. "Some observation on explosion development in process pipelines and implication for the selection and testing of explosion protection devices". Process Safety and Environmental Protection, Volume 86, Issue 3, pages 153-162, 153-162, 2008

[33]. F.K. Lu, J.M. Meyers, and D. R. Wilson, "Experimental study of a pulse detonation rocket

with Shchelkin spiral", ResearchGate, 2015

[34]. T.H. New, P.K. Panicker, K.F. Chui, H.M. Tsai and F.K. Lu, "Experimental Study on Deflagration-to-Detonation Transition Enhancement Methods in a PDE", ARC, 2012

[35]. D.D. Joshi, "Unsteady Thrust Measurement Techniques for Pulse Detonation Engines", UTA Doctoral Dissertation, 2014

[36]. Lawrence Livermore National Laboratory, "Chemical Kinetics Mechanism Archive" https://combustion.llnl.gov/archived-mechanisms/hydrogen

[37]. S. Gordon and B. J. McBride, "Computer program for calculation of complex chemical equilibrium compositions and application I. Analysis", Tech. Rep. NASA RP-1311, 1976. [Online]. Available: https://cearun.grc.nasa.gov/

[38]. Arm-Tex, "Fluid Handling Equipment Distributor", https://www.arm-tex.com/flame-arrestors.html

[39]. Gwyn Oakley, "Experimental Testing of 3D Printed Flame Arrestor", Aber Shock and Detonation Research Limited, AS80301, 2018

BIOGRAPHICAL STATEMENT

Hoden Ali Farah was born in Nazareth (Adama) Ethiopia. She earned her B.S. degree in Mechanical Engineering from Addis Ababa University in Ethiopia in 1984. She joined the University of Texas at Arlington (UTA) in the fall of 1990 and graduated with a M.S. degree in Mechanical Engineering in 1991. Her Master's thesis was "Symbolic Computation Application to Typical Fluid Mechanics Problems Using Galerkin Method". She also conducted research and studied the stability of high-speed liquid jet with a high-speed coaxial gas jet. After working for automotive, oil & gas industries and raising a family, she rejoined UTA PhD program in fall of 2016. Her research area is focused on industrial applications, numerical study of detonation propagation, flame arrestor element modeling using porous medium, determination of porous medium parameters using experimental methods, and interaction of detonation with the flame arrestor element. She currently works at Emerson as a Senior Design Engineer for new product development.